Aeroelastic optimization of thin flapping structure

by

Grace Swee See Goon

B.A., Cambridge University (2010)
M.Eng, Cambridge University (2011)

Submitted to the Department of Aeronautical and Astronautical Engineering
in partial fulfillment of the requirements for the degree of

Master of Science in Aeronautical and Astronautical Engineering

at the

MASSACHUSETTS INSTITUTE OF TECHNOLOGY

June 2017

Signature redacted

Author ....
Department of Aeronautical and Astronautical Engineering
May 18, 2017

Signature redacted

Certified by..... .....
Pedro M. Reis
Associate Professor of Mechanical Engineering and Civil and Environmental Engineering
Thesis Supervisor

Signature redacted

Accepted by .....
Youssef M. Marzouk
Associate Professor of Aeronautics and Astronautics
Chair, Graduate Program Committee

Aeroelastic optimization of thin flapping structure

by

Grace Swee See Goon

Submitted to the Department of Aeronautical and Astronautical Engineering
on May 18, 2017, in partial fulfillment of the
requirements for the degree of
Master of Science in Aeronautical and Astronautical Engineering

Abstract

We study the flow generated when a handheld fan is waved. This fluid-structure interaction problem is investigated through precision experiments, using an oscillating semi-circular elastic plate as a reduced analog model. The aerodynamic performance of the fans is systematically characterized for a variety of geometric and material parameters, as well as the amplitude of the periodic driving. We demonstrate that the bending stiffness of the structure can be tuned to maximize the output of the generated airflow, while simultaneously minimizing the input power. A design guideline is established for this optimal conditions based on matching the driving and the natural frequencies of the plate. Closer to the handheld fans, we then consider a discrete analog model comprising an array of overlapping strips. Unlike homogeneous plates, these discrete designs deform passively into shapes with finite Gaussian curvature and further enhance the generated flow. Finally, we explored the effect of corrugation on the flapping plate and found that the fan employs the interesting mechanism of reversible buckling to simultaneously increase the velocity of the flow and reduce the load.

Thesis Supervisor: Pedro M. Reis
Title: Associate Professor of Mechanical Engineering and Civil and Environmental Engineering

Acknowledgments

Firstly, I would like to take this opportunity to thank my advisor, Professor Pedro Reis for his guidance throughout this work. I would also like to thank Joel Marthelot, with whom I collaborated with on this work. I am also grateful for the members of the EGS.Lab who are always willing to provide advice and assistance. Next, I want to thank everyone here at MIT (especially the GCF and SSS friends) who had encouraged me through this process. I am also grateful to my parents back at home for being supportive. Finally, to my husband, Sam Elder for his love and care. Soli Deo Gloria.

Contents

Chapter 1

Introduction

In nature, flapping plates structures are often exploited dynamically in the biolocomotion of flying insects, birds and fishes. The animals are not only required to generate lift equal to their weight but also sufficient lift for acceleration from rest [56]. Some flying animals such as bats and insects were found to be able to generate maximum lift of up to 5 times the body weight despite the small wing area and low flying speed [40, 64]. The ability of the wings to generate lift through flapping locomotion cannot be simply described using fixed wing aerodynamics, since large wing deformation occurs over the flapping cycle [56].

Insects have evolved over the past 400 million years and the designs of their wings were optimized for flapping flights [16]. There are several studies that focused on the structural designs of insect wings: the vein thickness distribution on a dragonfly wing [28], the functionality of corrugation in dragonfly wings [47] and the venation network of various insect wings [16]. In particular, Combes and Dainel measured the flexural stiffness of the wings of different insect species and showed that stiffnesses of the wings depends on the cube of the span while the chordwise flexural stiffness to depend on the square of the chord length [12]. This result pointed towards a universal scaling and anisotropy of the wing designs, even though there is a wide variation in the venation networks across species of the insect [12, 16]. Combes and Daniel [13] also identified the thicker and stiffer veins along the leading edge as a common feature among insects, which is the main contributor to the anisotropy of the wings. On top

of the overview of insect flexural stiffness, studies on specific features such as the effect of a vein joint on the flexibility and the aerodynamic force generated by the wings of a bumblebee [44] suggests that flapping wing structures can be optimized by exploiting unconventional structural designs.

While studies of insect flight was of academic curiousity in the past, there is now great interest in the studies of the aeroelastic behavior of flapping wings due to the advancement in autonomous control, miniaturization of electronic components and interest in small scale flying vehicles [56, 61]. Micro Aerial Vehicles (MAVs), or a class of Unmanned Aerial Vehicles (UAVs) that are smaller than 15 cm in wing span, have become increasingly popular in military and commercial operations due to their ability to avoid detection and agility. Weight and size constraints motivates the optimization of every aspect of the flapping wing drones, including kinematics and structural designs. At the scale of the MAVs, flapping is the main mechanisms for propulsion [64] and many research groups had turned to drawing inspiration from real insect wings. Examples of bio-inspired MAVs are the Nano hummingbird [31], insect scale Microrobotic Fly [74] and DelFly [36]. Flexibility of the structure was found to have significant impact on the optimal thrust production of the wings and the structures undergo large deformation during the flapping [61].

A more common biomimetic object is the hand fan. It is used dynamically to generate flow and used as a cooling device [54] and its design was inspired by a bat's wing [51]. In this thesis, we present a study of using the foldable hand fan as an analog model for flapping wings. We explored the effect of bending stiffness on the flow generation of planar homogeneous plates, followed by three different heterogeneous plates: commercial hand fans, discrete model fans and corrugated fans. Even though the specific geometry is different, the aim is to study the effect of discrete nature of the elements of the hand fan and the effect of corrugation.

1.1 Past Studies of Flapping Plates

The optimization of flexural properties in fluid-structure couplings is ubiquitous in the engineering context of vortex-induced vibrations [73], and in biolocomotion [60] (*e.g.*, in bacterial flagella [35], fish fins [67] or insect wings [61]). More recently, the instabilities in flags had also been studied [19, 43] and proposed as a mechanism for power generation [6]. While the influence of elasticity on the optimal locomotion of fish [20, 21, 68] and the resonance of insect wings [29, 42, 49, 52, 53, 57, 65] on the generation of thrust and lift have been widely explored as flat plates or foils, the effect of structural features on the performance of flapping wings remains elusive.

The maximum and optimal thrust production was found to occur near the resonant frequency of the structure in a number of flapping plate studies [17, 22, 42, 49, 52]. For self propelled models, the optimal thrust production had occured at resonant frequency of as low as 0.41 of the natural frequency [29] to a range of 0.65-0.85 of the natural frequency [53, 65]. For comparison, the measurement of natural frequency of the dragonfly wings the flapping frequency is only at a fraction of the structural frequency [9]. The occurence of improved performance of plates at lower frequencies is thought to be due to the deformed shape being favorable to thrust production [53]. It was also observed that the system also simultaneously self-selects the conditions to achieve a Strouhal number of 0.25-0.35 [76], which are also exhibited by real fishes [67, 63].

Many studies also showed that there is an intermediate flexibility at which the wings produce the optimal thrust [2, 4, 24, 25, 42, 46, 49, 50]. The study of the flexibility of the flapping structure can be largely classified into four categories: variation of flexibility through changing the thickness or material of the homogeneous flapping plate [65], in chordwise [2, 23, 42, 49, 50, 52], spanwise [4, 24, 32] and both chord and spanwise directions [25, 45, 46]. The chordwise case can be studied using two-dimensional [2, 42, 49] or quasi two-dimensional [17, 23] geometries. In a study, it was found that intermediate flexibility improved the thrust production by 1-2 times and doubles the efficiency [17]. The motion of the trailing edge of the airfoil was

also observed and foils with intermediate flexibility were found to produce favorable deflection that alters the effective angle of attack of the airfoil [4, 53]. Intermediate spanwise flexibility was found result in about a 50% increment in thrust and lower flexibility were found to cause the tip of the wing to move out of phase with the root, thus diminishing the thrust production [4, 24]. In a study that changes both the chord and spanwise direction, it was also found that increasing the flexibility of the leading edge structural member has a detrimental effect to the thrust production and increasing the flexibility of the wing relative to the leading edge improves thrust [46]. Most studies had relied on only changing the materials or thickness of thin homogeneous plates, while steering clear of more complicated structures. For studies that used composite wings [25], the studies again focused on the materials and little structural details were explored.

The flapping behavior is also studied using a modified versions of the Euler-Bernoulli beam theory and order of magnitude scaling of forces [17, 20, 29, 52, 65]. Thiria and Godoy-Diana characterized the flexibility of the wing by the ratio of inertia to elastic force [65]. Kang *et al.*. additionally scaled the added mass and aerodynamics term with non-dimensional numbers to derive the optimal thrust frequency [29]. While using order of magnitude scaling to study flapping motion is not new, most of the studies had focused on finding optimal frequency with few mention on effect of amplitude [49].

While there are considerable efforts in the aeroelastic study of flapping structures, there are still a few open questions. In terms of operating conditions, many literature focused on the flapping frequency and only a few studies investigated the effect of linear flapping amplitude [76, 49]. How the angular flapping amplitude affect the thrust generation was not addressed by past studies. Flapping structures in nature have complicated features; the effects and functionalities of (1) corrugation, (2) stiff discrete members held together by compliant materials, (3) distribution of venation network of the insect wings, (4) porosity, and (5) aspect ratio of the wings on thrust production were not studied in detail. In this thesis, we will address our question on flapping amplitude and the effects of the first two structural designs. Finally,

Schnipper *et al.* [58] studied the vortex structure generated by a two dimensional foil flapping in a stationary soap film but otherwise, the work reported in the current thesis the first time the hand fan is studied in the context of aeroelasticity.

1.2 The Hand Fan as an Analog Model to Study Flapping Structures

Flexible handheld fans have been in existence since ancient Egypt and Assyria [54]. In Egypt, fans were symbols of wealth and power and divine items used in religious ceremonies. Because of the esteemed status of the fans, they were made with exotic materials such as ostrich feathers and embellished with precious stones and metals [54]. The Japanese were credited for inventing the folding fan based on historical writings by Japanese and Chinese scholars [51].

A diagram depicting the different parts of a hand fans and terminology are shown in Fig.1-1. The foldable fans typically comprise an array of discrete radial *sticks* that narrow to become *ribs*, themselves attached to the *leaves*. The sticks are pinned together at the head by a *rivet* which is the point of rotation for the sticks. The top and bottom sticks are called *guards* [41]. The sticks and ribs are traditionally made of wood, and the leaves are connected by fabric, threads or paper [54]. Foldable fans with ribs that are connected by fabric leaves are known as the *pleated fans* while fans with ribs that are only connected at the tip with threads or ribbons are *brisé fan* [3].

Since the advent of the portable foldable fan, their use as an instrument to cool one down became increasingly popular. The to and fro axial motion about one's hand, displaces the air around the fan and generates vortices, thereby inducing flow. The foldable fans were introduced to Europe in the 16th century [3] and the craftsmanship of high-end artisanal fans has been passed down through generations; the geometry of the layout, together with materials, are careful selected to enhance the aerodynamic performance [38].

Based on historical writings, the design of the foldable hand fan was also inspired

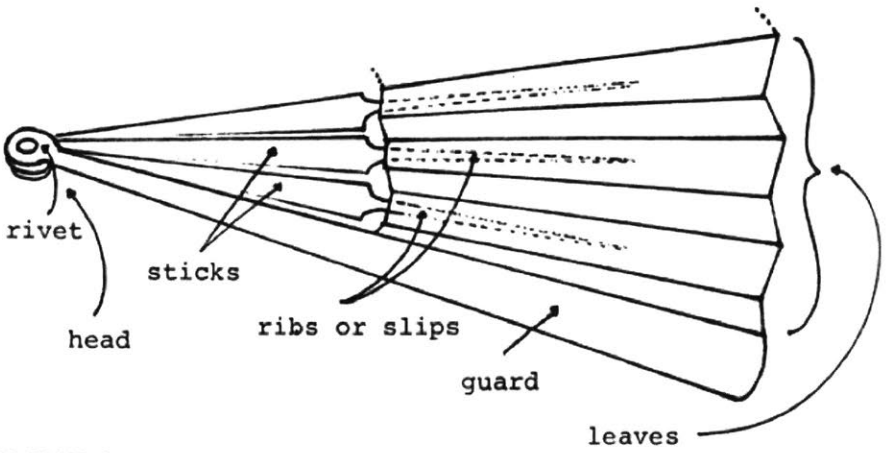

DIAGRAM A

THE ANATOMY OF A FOLDING FAN

Figure 1-1: The parts and terminology of a pleated hand fan. Figure adopted from [41]

by the wings of a bat [51]. In fact, bats are not the only animals that possess a stick-ribs-leaves structure. In marine biology, animals that use the fins for propulsion such as fishes [34] and seahorses [15] have radial arrays of bony fin rays that form the surface called the fins [34].

The wings of insects also have the stick-ribs-leaves structure. They consist of tubular veins spread out over the plane surface of the wings also known as the membrane. Even though the veins are made of similar materials as the wing membrane, the increased second moment of inertia of the tube causes an increased flexural stiffness [12]. For some species from the *Lepidoptera* (butterflies/moth) and *Diptera* (flies) order, the longitudinal veins form a radial pattern [14]. In the *Odonata* (dragonflies, laceflies) order, pleated structures were observed and the wings were observed to be able to carry very high loads and buckle reversibly [47]. Hence, the foldable hand fan is a good analog for these features in fish fins and insect wings.

1.3 Plate Bending and Vibration Theory

A plate is defined as a structural element where two of the dimensions are orders of magnitudes larger than the third dimension. The plane formed by the two larger dimension defines the face of the plate and the third dimension is the thickness [66, 70].

The stress and deformation of a flat plate subjected to known loads or vibration are well described using the Kirchoff-Love plate theory, which is an extension of the Euler-Bernoulli beam theory [66, 70].

Assuming a characteristic length scale of a for the planar dimension and thickness h, the way the plates carry load is highly dependent on the ratio of the thickness to the planar dimensions a/h. Plates with $a/h \sim 1-10$ [70] can be regarded as thick plates and the plate theory cannot be applied. For plates with $a/h \geq 10$, which is the case for all the results in this thesis, the plate theory can be used, and depending on the deflections relative to the thickness, the plate will either carry the load by bending or through membrane forces. Plate theory can only be applied to developable surfaces, or surfaces that have zero Gaussian curvature.

The governing equation for plates under pure bending is given by the Kirchoff-Love plate theory:

$$\frac{\partial^4 \xi}{\partial x^4} + 2\frac{\partial^4 \xi}{\partial x^2 \partial y^2} + \frac{\partial^4 \xi}{\partial x^4} = 0, \tag{1.1}$$

$$\nabla^2 \nabla^2 \xi = 0, \tag{1.2}$$

where ξ is the deflection and ∇^2 is the Laplace operator. Under a transverse load (perpendicular to the planar surface):

$$\nabla^2 \nabla^2 \xi = -\frac{q}{B} \tag{1.3}$$

where q is the load per unit area and B is the flexural stiffness per unit length. For the case where the bending motion is independent in one of the dimension (say y), the Kirchoff-Love theory can be simplified to a form similar to the Euler-Bernoulli equation

$$\frac{\partial^4 \xi}{\partial x^4} = -\frac{q}{B} \tag{1.4}$$

For plates under vibration, the governing equation is given by adding the D'Almebert forces to Eq. (1.3):

$$B\nabla^2 \nabla^2 \xi + \rho_p h \ddot{\xi} = P(x, y, t) \tag{1.5}$$

where ρ_p is the density of the plate and P is the excitation given by

$$P(x,y,t) = \sum_{m=1}^{\infty}\sum_{n=1}^{\infty} f_{mn}(t)\xi_{mn}(x,y) \tag{1.6}$$

$$w(x,y,t) = \sum_{m=1}^{\infty}\sum_{n=1}^{\infty} F_{mn}(t)W_{mn}(x,y) \tag{1.7}$$

where f_{mn} is the forcing term, F_{mn} is the response term, W_{mn} is the normalized mode shape, and m and n are the mode numbers. Assuming ξ is sinusoidal in time, $\ddot{\xi} = -\omega^2\xi$, where ω is the natural frequency . For free vibration we have:

$$B\nabla^2\nabla^2 W_{mn} - \rho_p h\omega_{mn}^2 W_{mn} = 0 \tag{1.8}$$

which is satisfied at every location on the plate. Hence, we have to integrate Eq. (1.8) over the entire plate [30]

$$\int_A\int_A B\nabla^2\nabla^2 W_{mn} - \rho_p h\omega_{mn}^2 W_{mn} dA = 0 \tag{1.9}$$

and we define the modal mass μ_{mn} and modal stiffness κ_{mn} (characteristic kinetic energy and bending energy at mode shape mn) respectively:

$$\begin{aligned} \mu_{mn} &= \rho h \int_A\int_A W_{mn}^2 dA \\ \kappa_{mn} &= \int_A\int_A B\nabla^2\nabla^2 W_{mn} dA \end{aligned} \tag{1.10}$$

where A is the area of the plate. The natural frequency can be found using

$$\omega = \sqrt{\frac{\kappa_{mn}}{\mu_{mn}}} \tag{1.11}$$

and we will now have to find expressions for W_{mn} by considering an estimate of the mode shape based on the boundary conditions.

We will now use Eq. (1.11) to derive the natural frequency of a rectangular plate

shown in Fig. 1-2 with one fixed boundary ($x = 0$) and free boundary conditions on the other three sides, ($x = a$, $y = 0$, $y = b$). The boundary conditions are thus

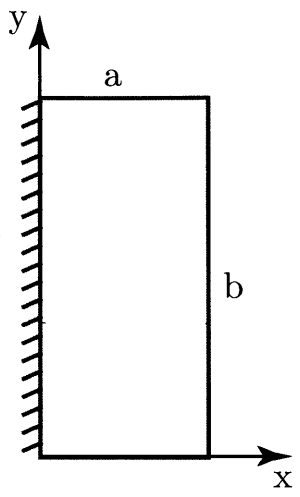

Figure 1-2: $x - y$ plane of a rectangular plate.

1.

$$W = 0, \quad \frac{\partial W}{\partial x} = 0 \quad \text{at} \quad x = 0 \tag{1.12}$$

2.

$$M_y = \frac{\partial^2 W}{\partial y^2} + \nu \frac{\partial^2 W}{\partial x^2} = 0, \quad V_y = -\frac{\partial}{\partial y}\left[\frac{\partial^2 W}{\partial y^2} + (2-\nu)\frac{\partial^2 W}{\partial x^2}\right] = 0 \quad \text{at} \quad y = 0, b \tag{1.13}$$

3.

$$M_x = \frac{\partial^2 W}{\partial x^2} + \nu \frac{\partial^2 W}{\partial y^2} = 0, \quad V_x = -\frac{\partial}{\partial x}\left[\frac{\partial^2 W}{\partial x^2} + (2-\nu)\frac{\partial^2 W}{\partial y^2}\right] = 0 \quad \text{at} \quad x = a \tag{1.14}$$

A way to estimate the natural frequency in Eq. (1.11) is to assume a mode shape that satisfies the boundary conditions. A solution for W is given by

$$W = 0, \quad \frac{\partial W}{\partial x} = 0 \quad \text{at} \quad x = 0$$
$$\frac{\partial^2 W}{\partial y^2} = 0, \quad \frac{\partial^2 W}{\partial x^2} = 0 \quad \text{at} \quad y = 0, b \quad \text{and} \quad x = a \tag{1.15}$$

Using a combination of sinusoidal and linear functions, we find that

$$W = \sin\left(\frac{n\pi y}{b}\right)\sin\left(\frac{m\pi x}{a}\right) - \left(\frac{m\pi x}{a}\right)\sin\left(\frac{n\pi y}{b}\right) \tag{1.16}$$

defines the mode shapes satisfies Eq. (1.15). Note that in order to satisfy the boundary conditions, $m = \mathbb{Z}^+$ and $n = \mathbb{N}$. Since the plate is unconstrained in the y direction, we can assume a pure bending scenario, the surface is developable (Gaussian curvature is zero) [5]. To have zero Gaussian curvature, we require $n = 0$:

$$W = \sin\left(\frac{m\pi x}{a}\right) - \left(\frac{m\pi x}{a}\right) \tag{1.17}$$

To get the mode shape for the first mode, we substitute $m = 1$ into Eq. (1.17):

$$\begin{aligned} \mu &= \frac{1}{6}\left(2\pi^2 - 9\right)ab\rho h \\ \kappa &= \frac{2ab}{\pi}B\left(\frac{\pi}{a}\right)^4 \end{aligned} \tag{1.18}$$

The natural frequency can then be estimated by substituting Eq. (1.18) into Eq. (1.11):

$$\omega = 0.356\left(\frac{\pi}{a}\right)^2\sqrt{\frac{B}{\rho h}} = 3.51\sqrt{\frac{B}{\rho h a^4}} \tag{1.19}$$

For a plate of similar deflection distribution but with different geometry, the natural frequency can be expressed as

$$\omega = k\sqrt{\frac{B}{\rho h a^4}} \tag{1.20}$$

where a is a characteristic length scale of the plate and k is a dimensionless prefactor that depends on the geometry of the plate. We will use this expression in Chapter 3 to obtain the prefactor for a semi-circular plate. The experimentally obtained prefactor will then be used to estimate the natural frequency of plates beyond the limits of our instruments.

1.3.1 Orthotropic Plates

The heterogeneous plates in our study have regular linear or radial structural patterns (detailed descriptions of the heterogeneous plates can be found in Section 2.3). Even though there may be local variation or discontinuities in flexural properties, we can idealize the global behavior of the plates to be similar to an orthotropic plate. In solid mechanics, a material or structure is known as orthotropic when its properties have symmetry along three mutually orthogonal axis. The strain is related to the stress in an orthotropic material by [7]

$$\begin{bmatrix} \epsilon_{xx} \\ \epsilon_{yy} \\ \epsilon_{zz} \\ \gamma_{yz} \\ \gamma_{xz} \\ \gamma_{xy} \end{bmatrix} = \begin{bmatrix} \frac{1}{E_x} & -\frac{\nu_{xy}}{E_y} & -\frac{\nu_{zx}}{E_z} & 0 & 0 & 0 \\ -\frac{\nu_{xy}}{E_x} & \frac{1}{E_y} & -\frac{\nu_{zy}}{E_z} & 0 & 0 & 0 \\ -\frac{\nu_{xz}}{E_x} & -\frac{\nu_{yz}}{E_y} & \frac{1}{E_z} & 0 & 0 & 0 \\ 0 & 0 & 0 & \frac{1}{G_{yz}} & 0 & 0 \\ 0 & 0 & 0 & 0 & \frac{1}{G_{xz}} & 0 \\ 0 & 0 & 0 & 0 & 0 & \frac{1}{G_{xy}} \end{bmatrix} \begin{bmatrix} \sigma_{xx} \\ \sigma_{yy} \\ \sigma_{zz} \\ \sigma_{yz} \\ \sigma_{xz} \\ \sigma_{xy} \end{bmatrix}$$

For a plate, we consider the plane stress condition which makes the assumption that the plate does not carry stress in the direction of the thickness: $\sigma_{zz} = \sigma_{yz} = \sigma_{xz} = 0$. Thus the stresses in a plates made with orthotropic material are [37]:

$$\begin{bmatrix} \sigma_{xx} \\ \sigma_{yy} \\ \sigma_{xy} \end{bmatrix} = \frac{1}{1-\nu_x\nu_y} \begin{bmatrix} E_x & E_\nu & 0 \\ E_\nu & E_y & 0 \\ 0 & 0 & (1-\nu_x\nu_y)G_{xy} \end{bmatrix} \begin{bmatrix} \epsilon_{xx} \\ \epsilon_{yy} \\ \gamma_{xy} \end{bmatrix} \tag{1.21}$$

where $E_\nu = \nu_y E_x = \nu_x E_y$, ν_x and ν_y are the Poisson ratio and E_x and E_y are the Young's Modulus about the x or y direction.

$$\begin{bmatrix} \sigma_{xz} \\ \sigma_{yz} \end{bmatrix} = \begin{bmatrix} G_{xz} & 0 \\ 0 & G_{yz} \end{bmatrix} \begin{bmatrix} \gamma_{xz} \\ \gamma_{yz} \end{bmatrix} \tag{1.22}$$

Note that even though the stresses σ_{xz} and σ_{yz} are assumed to be negligible in plate bending, vertical shear forces are required for the equilibrium of the plates [70].

$$\begin{bmatrix} M_x \\ M_y \\ M_{xy} \end{bmatrix} = \int_{-h/2}^{h/2} \begin{bmatrix} \sigma_{xx} \\ \sigma_{yy} \\ \sigma_{xy} \end{bmatrix} z\mathrm{d}z \tag{1.23}$$

$$\begin{bmatrix} Q_x \\ Q_y \end{bmatrix} = \int_{-h/2}^{h/2} \begin{bmatrix} \sigma_{xz} \\ \sigma_{yz} \end{bmatrix} z\mathrm{d}z \tag{1.24}$$

where M_x, M_y and M_xy are the bending moments and Q_x and Q_y are the shear force.

For our application, we want to look at structurally orthotropic plates made with isotropic materials, such as corrugated plates or plates with stiffeners. To calculate the forces and moments, we can substitute Eq. (1.21) into Eq. (1.23) and (1.24), using $E_x = E_y = E$ and $\nu_x = \nu_y = \nu$, and also using the strain curvature assumptions, we obtain:

$$\begin{bmatrix} M_x \\ M_y \\ M_{xy} \end{bmatrix} = \begin{bmatrix} -B_x \left(\frac{\partial^2 w}{\partial x^2} + \nu \frac{\partial^2 w}{\partial y^2} \right) \\ -B_y \left(\frac{\partial^2 w}{\partial y^2} + \nu \frac{\partial^2 w}{\partial x^2} \right) \\ B_{xy} \left(1 - \nu\right) \frac{\partial^2 w}{\partial x \partial y} \end{bmatrix} \tag{1.25}$$

where B_x, B_y and B_{xy} are the effective flexural stiffnesses relating moments to curvature.

For some cases such as plates with stiffeners, we can obtain the flexural stiffnesses through direct evaluation of the the integrals in Eq. (1.23) and (1.24). For corrugated plates, the flexural stiffness are dependent on the effective curvature and Castigliano's second theorem was used to derive the effective flexural stiffnesses proposed by Briassoulis [8]. The equations for the effective flexural stiffnesses derived from the two different methods for corrugated plates are presented in Chapter 4.

1.3.2 Anisotropy of the Hand Fan and the Effect on Natural Frequency

The stiffer sticks/ribs of the hand fans are arranged in a radial fashion and the ribs are connected to adjacent ribs by compliant leaves. This radial arrangement resulted in different flexural stiffness in the radial and tangential direction and the hand fan is polar orthotropic. If we assume that the tangential flexural stiffness is negligible compared to the radial flexural stiffness, we can consider each stick/rib of the hand fans to behave like a beam and derive its characteristic natural frequency based on the flexural stiffness and the mass of the fans. For a cantilever beam the natural frequency is given by [30]

$$\begin{aligned} \omega_j &= \frac{\beta_j}{L^2}\sqrt{\frac{EI}{\rho A_b}} \\ \beta_1 &= 0.597\pi \\ \beta_j &= \left(j - \frac{1}{2}\right)\pi \end{aligned} \tag{1.26}$$

where j is the mode number of the vibration and area A_b refers to the cross sectional area of the beam. For our hand fans, we can only experimentally measure their mass and we express the average mass per unit length, $m = \rho A = \frac{M}{R}$ where M is the mass of the fans and R is the radius of the fan.

For the hand fans, we will test our assumption that the hand fans are behaving like beams in Chapter 4 by using the following expression for the natural frequency of the hand fan:

$$\omega_f = \frac{k_f}{L^2}\sqrt{\frac{EI}{\rho A_b}} \tag{1.27}$$

where k_f is a dimensionless prefactor. If the hand fans do vibrate like beams, we will find k_f to be a constant.

1.4 Outline of Thesis

In the current introduction, we have provided a literature review and highlighted some of the relevant theory that will be used throughout this thesis. Chapter 2 describes the experimental apparatus used to conduct our studies, the process of choosing the hand fans and the fabrication of the model fans. Our study is divided into two main categories; flat homogeneous and heterogeneous plates. Our results for the homogeneous plates and theory to understand the scaling of flapping amplitude are reported in Chapter 3. In Chapter 4, we present the experimental results for the commercial hand fans, discrete model fans and corrugated fans. We will also contrast them with the corresponding values for the homogeneous plates. Finally, a summary of the outcomes of the thesis and areas of future work are provided in Chapter 5.

Chapter 2

Experimental Apparatus

In this chapter, we describe the setup and calibration for the experiments and method for the fabrication of the specimens. We designed and constructed an experiment set up that imposes the flapping motion of the fan, measure the flow generated by the fan and the torque required. The method for obtaining the instantaneous deflection of the fans during the flapping motion will also be presented. The chapter will also address the instruments and methods used to measure the natural frequency of the hand fan and plates. We then discuss the process of selecting the Spanish style of hand fans for this study and describe the structural elements of and materials used on the hand fans we acquired. Based on the design of the hand fans, we present the methods for making model fans that mimic two structural features of the hand fans. Semi-circular flat plate fan of various thicknesses were used as a baseline comparison and discrete model fans were designed to study the ribs-leaves feature of the hand fan. We also introduce corrugation to the thinner plates to study its effect. Finally, for our study we first evaluated the flexural stiffness of the hand fan by performing a precision load deflection test and the results for selected fans are also presented.

2.1 Flow Generation Experiment

In order to study the effect of structure on flapping fan behavior we designed an experimental set up that imitates the fan flapping motion (Section 2.1.1) and measure the flow output (Section 2.1.2). In Fig. 2-1a, we present a photograph of the experimental apparatus used to measure the flow output and input torque of handheld fans or, their simplified analogue models. A motor is aligned horizontally with the shaft connected to the input shaft of the 1:5 step down gearbox. The output shaft of the 1:5 right-angle speed reducer is aligned vertically and the motion is transmitted

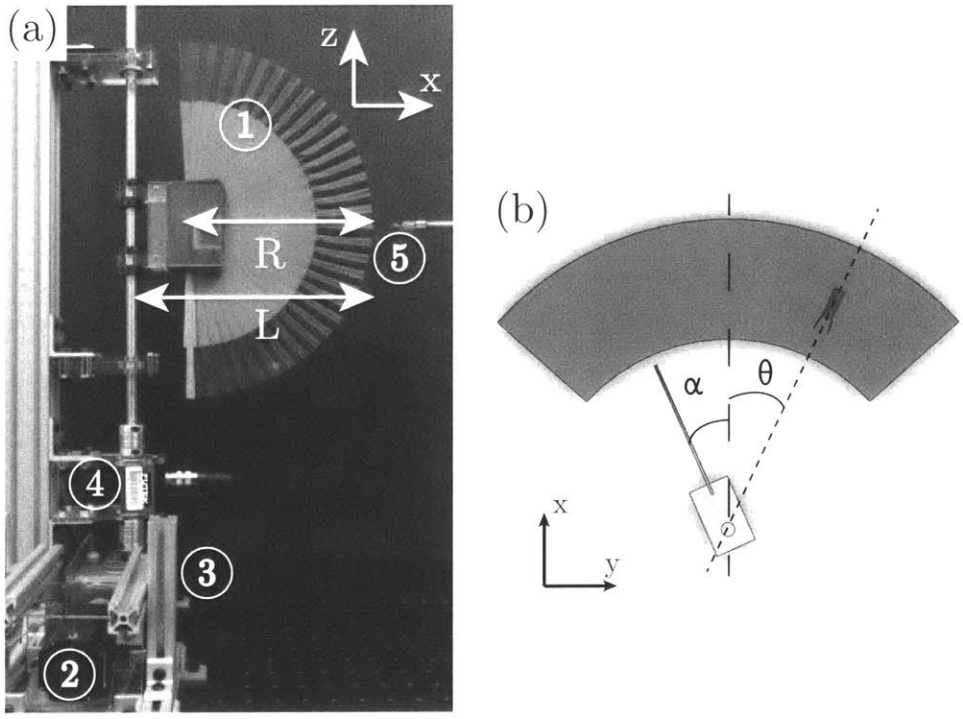

Figure 2-1: (a) A fan (1) is driven by a stepper motor (2), connected to 1:5 step down gearbox (3) followed by a torque sensor and encoder (4). The generated velocity is measured with an hot-wire anemometer (5). (b) A top down schematic indicating the flapping amplitude α and the angle between the hot-wire anemometer and the center line of the flapping motion. The red strip is on the x-y plate and on the same heigh as the symmetry line of the fan and indicates the range of positions the hot-wire anemometer.

through to a rotary torque sensor and encoder to a 6.35 mm diameter D-profile stainless steel shaft. The D-profile prevents the connector clamps inserted from slipping and D-profile shaft collars were used to secure the connector clamps along the axis of rotation. There is a stainless steel shaft coupling between each piece of equipment. The couplings match the diameter of the connector shaft of each piece of equipment to ensure that all the connections are aligned properly and prevent relative slip.

The control and operation of the flapping motion set up is described in Section 2.1.1. For flow measurement, we used a TSI 1210 hot wire anemometer. Before using the hot wire anemometer, calibration was carried out for flows between 0.3-11 m/s. The calibration methods and set up are described in Section 2.1.2. In the experiment, the hot wire anemometer was placed such that it is always pointing towards the axis of rotation and in plane indicated in Fig. 2-1b. Finally, to determine the surface deflection of the fans or models during flapping, strobe-trigger method was used to capture still photograph explained in Section 2.1.4.

2.1.1 Control of the Flapping Motion

The rotary stepper motor (NEMA23) was controlled by a Copley Controls Stepnet stepper amplifier through an ethernet cable via a Kvaser CAN communication adaptor. This allows us to program the motion using National Instrument LabView. We are able to control the stepper motor accurately to 0.5° and using a 1:5 right-angle speed reducer (Boston Gear) between the motor and the shaft, we improved the accuracy of the control to 0.1° and hence smoother flapping motion.

Using the manufacturer-provided motor control functions for the Copley amplifier for LabView, we programmed the motor to drive the motion for a series of amplitude at a fixed frequency. We imposed its angular position: $\Theta(t) = \alpha \sin(\omega t)$, where α is the angular amplitude (Fig. 2-1b), and t is time. The driving frequency was fixed at $\omega = 2\,\mathrm{Hz}$ to match comfortable operation conditions of handheld fans and the angular amplitude was varied over the range $8 \leq \alpha\,[^\circ] \leq 56$.

2.1.2 Measurement of Flow Generated by the Fans or Models

Due to the transient nature of the flow generated by a flapping structure, we require a measurement instrument that has high acquisition rate. While pitot tubes are more accurate for steady flow, it can take up to a couple of seconds to stabilize. Assuming the comfortable flapping frequency for a person flapping a fan is ~2 Hz and every complete oscillation passes through the middle of the flapping motion twice, generating a ~4 Hz signal and thus the minimum sampling rate required is ~8 Hz. The hot-wire anemometer we used (TSI 1210) can handle transient responses up to 500 Hz, which is sufficient for our experiment.

Before using the hot wire anemometer, we have to calibrate the probe. For low speed, U_g we calibrated the probe by mounting it on a high precision linear positioner (Parker Daedal model 404150XRMP-D2-H1L1) attached to a stepper motor and the motion of the stepper motor was controlled using LabView. As the hot wire anemometer moves together with the linear stage, the relative velocity of the air will be the speed of the movement. The linear stage was made to move at a speed of $U_g = 0.3-0.7$ m/s and the output voltage from the hot-wire anemometer was recorded using Logger Pro (Vernier Pro Software). For calibration at higher speed, the setup

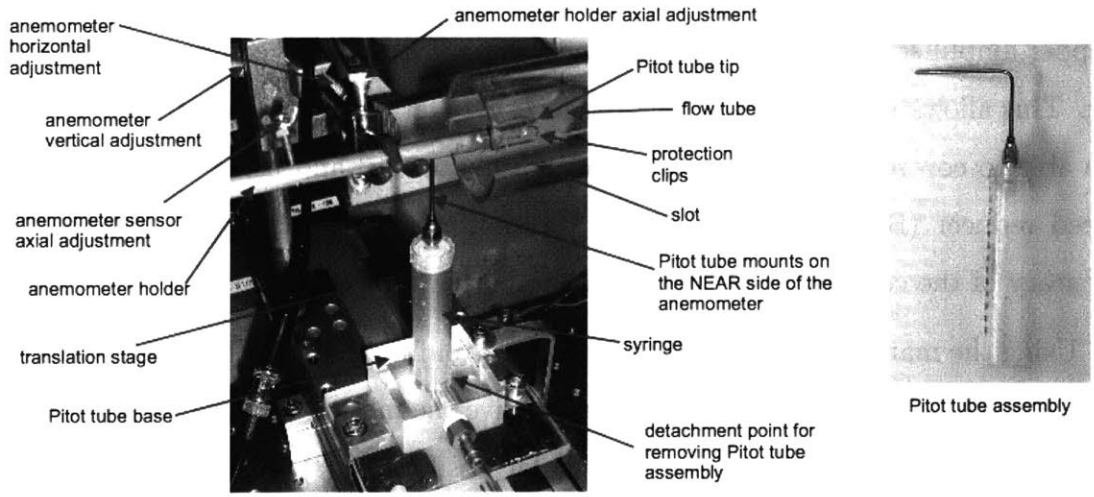

Figure 2-2: Photograph of the experimental setup for higher air flow U_g hot wire anemometer calibration and the pitot tube assembly. Figure adopted from [26].

in the 2.671 Instrumentation and Measurement lab shown in Fig. 2-2 was used. The flow is produced by releasing compressed air from a tank through a 100 mm inner diameter cylindrical tube. A pitot tube (Omega Engineering PX138-0.3D5V) and the hot wire anemometer were placed at the opening of the tube. They were positioned in the middle of the cylindrical tube opening to avoid significant boundary layer effect. The output pressure $P_g \approx \{300, 450, 600\}$ kPa will typically produce a flow of $U_g = 4 - 12$ m/s in the cylindrical tube. At each pressure setting, the pitot tube was first used to accurately determine the steady gas flow speed U_g in the cylinder. Then the output voltages of the hot wire anemometer probe for velocities of $U_g = 5 - 11$ m/s were obtained for our experiments. The constants from the calibration can then be found by fitting V_{ane}, the voltage measured by the anemometer, and U_g, the speed of the air, to the equation provided by the manufacturer $V_{ane}^2 = C_1 + C_2\sqrt{U_g}$, as shown in Fig. 2-3.

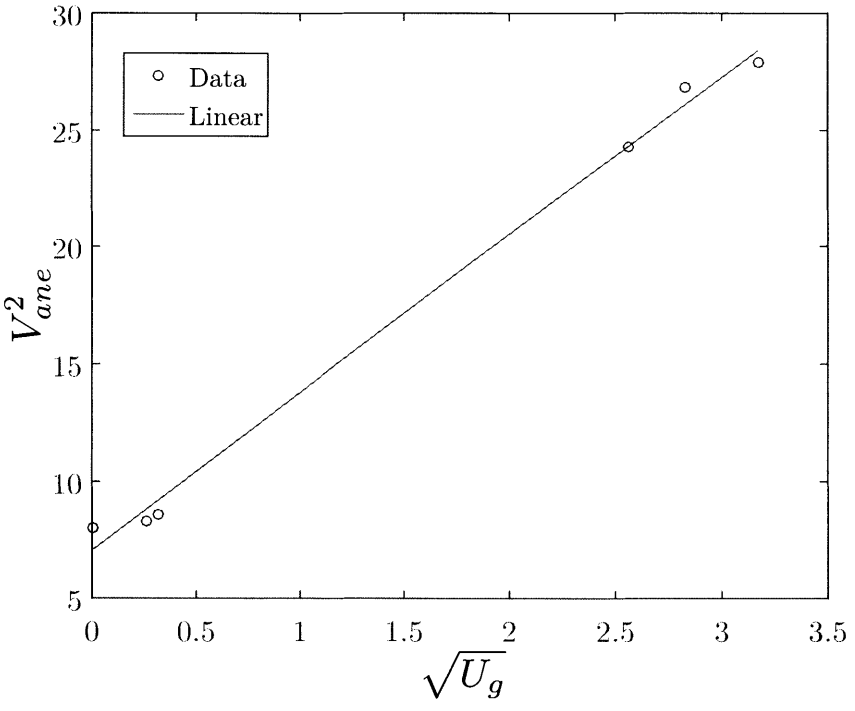

Figure 2-3: Plot of V_{ane}^2 against $\sqrt{U_g}$ use to derive the constants for the calibration of the hot wire anemometer. The fit of the data is $V_{ane}^2 = C_1\sqrt{U_g} + C_2$, where $C_1 = 6.73 \pm 0.6$ and $C_2 = 7.06 \pm 1.3$.

The calibrated hot-wire anemometer can now be used in the flow measurement experiment. The instantaneous velocity of the generated flow, $u(t)$, was measured by setting the single point hot-wire anemometer perpendicular to the axis of rotation, at a distance d from the fan tip and an angle θ from the mid point of the flapping tip motion, along the x-axis. Measurement of the velocity was carried out in the x-y plane on the same height as the symmetry line of the fan indicated by in Fig. 2-1, by having the center of the flapping motion be offset by an angle of θ, which allowed us to obtain the corresponding data without having to change the position of the hot-wire anemometer after every single data point. Based on the time average velocity field of velocity the final measurement location of $d = 0.1R$ and $\theta = 0°$ was selected. The specific results are presented in Section 3.3. For collection of data, the output of the hot-wire anemometer is collected via the National Instrument Data Acquisition device (USB-6002) and processed using LabView. In Fig 2-4, we present a 2 s sample of the instantaneous velocity, $u(t)$, measured by the hot-wire anemometer using LabView. Note that the flapping frequency is set at 2 Hz, but there are four peaks every second. This is because there are two symmetrical passes

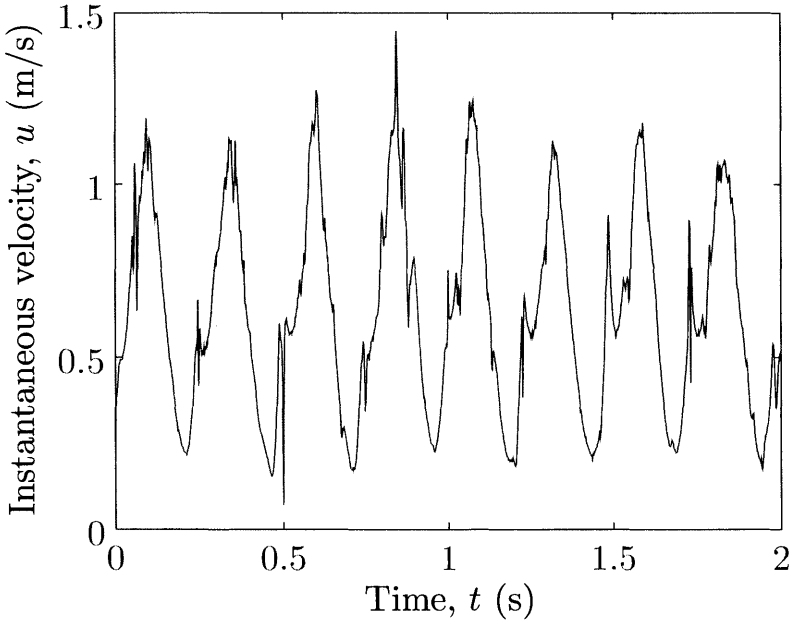

Figure 2-4: A 2 s sample of velocity measured by the hot-wire anemometer. For this signal, $h = 254\,\mu$m, $R = 200$ mm, $\theta = 0°$, $d = 20$ mm and $\omega = 12.6$ rad/s (2 Hz).

of the fan in every complete oscillation when $\theta = 0°$ and the hot-wire anemometer does not distinguish the direction of the flow. The peaks are of approximately the same height, indicating that the plate is flapping symmetrically.

2.1.3 Torque Measurement

We also want to know the torque required to impose the flapping motion, so that we can evaluate the input power. The instantaneous rotational input power can be computed using $P_i = \tau\dot{\Theta}$ where τ is the torque and $\dot{\Theta}$ is the instantaneous rotational velocity. Hence, we added a rotatory torque sensor and encoder (Futek TRS 605) to our set up (Fig. 2-1a) to measure the torque. The TRS605 measures torque up to 10 N/m with an uncertainty of $\delta\tau = \pm 0.02$ N/m and can measure the position of the fan up to 0.5°. The typical magnitude of torque is in the range of $|\tau| \approx 0.5 - 2$ N/m. Due to taring procedures where we subtract the torque measurement without the fans from the overall torque measurement, the uncertainty is $2\delta\tau/|\tau| \approx 2 - 8\%$. Both sets of data were recorded simultaneously and we can then extract the phase data of the torque output. Again the output signal is collected using the USB-6002 and processed using the same LabView program for the data collection of the flow generation. This allows us to record both the torque τ and angular position Θ together with the corresponding output flow, $u(t)$ simultaneously. Finally, we can then extract the phase averaged flow velocity at each measurement location for a given fan position to obtain the phase averaged velocity field. The results and data analysis are presented in Section 3.2.

2.1.4 Strobe Still Photography

Since we are interested in the effect of the geometry of the fans, we want to obtain the instantaneous deflection of the fans during flapping. The idea behind the technique is by controlling the amount of light in the environment, such that the camera only captures the instance when the lights are on. For that to work, the camera has to placed on long exposure mode in a dark room. The light strobe goes off at the the

specific time and the camera will capture a still image at the specific instance.

In order to use the technique on our experiment, we need to make some minor changes to the set up. A generic infrared beam-break sensor (it is a simple device constructed with infrared transmitter and receiver), shown in Fig. 2-5, is mounted next to the rotating shaft and a beam inserted into the rotating shaft such that every time the fan crosses the center line, the beam passes between the beam-break sensor, creating a gap in the signal collected by the receiver side of the beam-break sensor. The sensor sends binary signals every 50 ms to a trigger kit (Cognisys Stop Shot) which we programmed to send a trigger to a photography strobe light every time a gap is observed. The strobe light then produce a flash of light. We also programmed the trigger kit to send at most one pulse every second. Due to the frequency of the signal, the time delay of the trigger is less than 50 ms which is significantly lower than the frequency of the flapping motion of 2 Hz.

To collect our data, the specimen was first prepared by adding a regular array of points on the surface of the fan. We found that grids arranged in a rectangular grid Fig. 2-6a or radial array Fig. 2-6b resulted in similar findings on the flat semi-circular plate and thus opted to perform the test using a radial grid because of the geometry of the hand fans. A Nikon D600 camera is set up facing the face of the fan perpendicularly. The camera was set on the 0.5 s exposure mode and captured a still image at the instantaneous moment when the strobe light flashed. A photograph

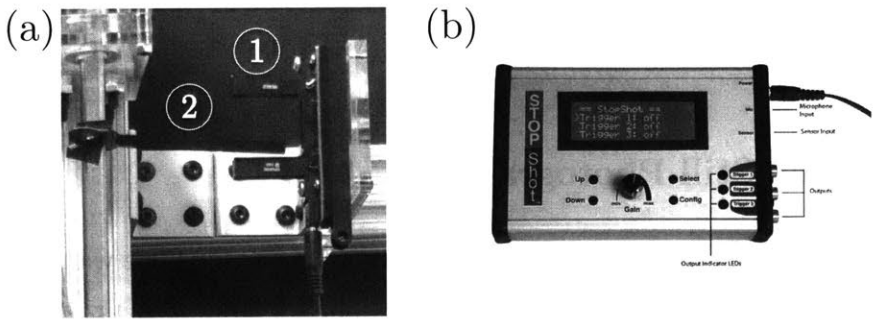

Figure 2-5: (a) Photograph of the mounted (1) infrared beam-break sensor and the (2) beam attached to the rotating shaft. (b) the Cognisys stop shot trigger kit.

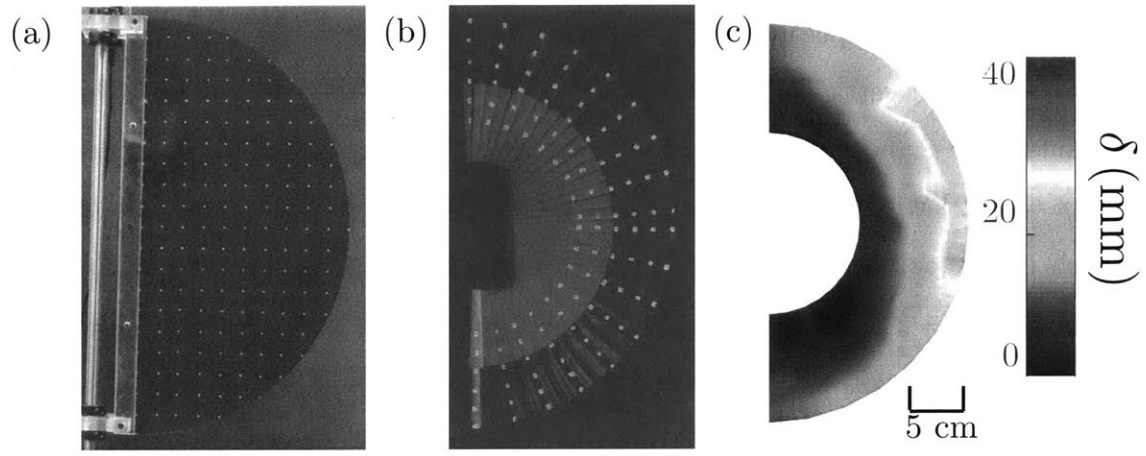

Figure 2-6: (a) Example of a grid of points on a semi-circular plate of $R = 200$ mm and $h = 254\,\mu$m (b) Grid of points on Fan 1. (c) Example of the resultant deformation field.

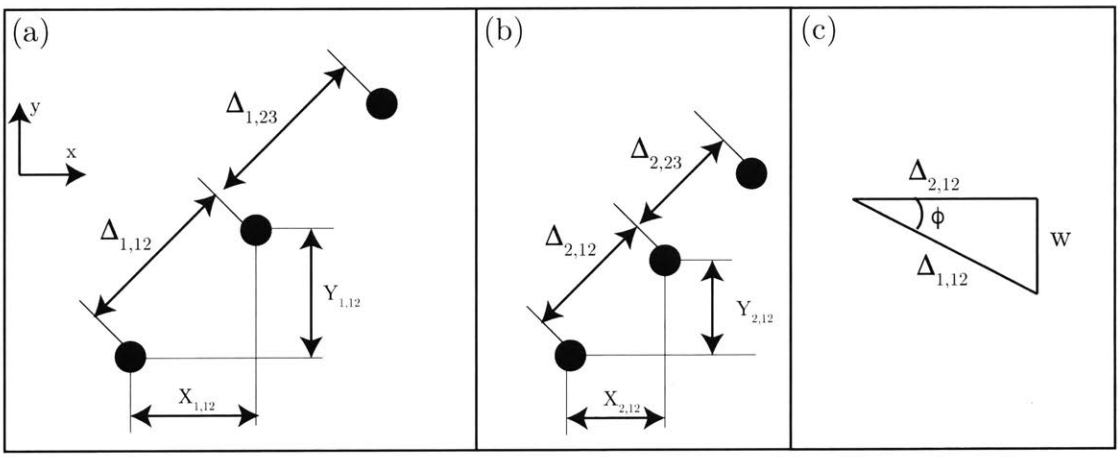

Figure 2-7: Schematic showing the points on a (a) undeformed and (b) deformed surface. (c) Schematic showing the deflection of the relationship between deformed and undeformed planar length.

at the same angle is also obtained when the fan is not flapping and this will give us the undeformed configuration. Fig.2-7a and b are schematics of the undeformed and deformed grid array respectively. Considering the x-axis and y-axis to be aligned with the horizontal and vertical sides of the photo, we can find the coordinates of each of the points. The x and y distance between successive points are defined $X_{p,qr}$ and Y_{p_qr} where $p = \{1, 2\}$ with 1 =undeformed and 2 =deformed and q and r are the identifier for each of the points in the array. The distance between two successive points is $\Delta_{p,qr} = \sqrt{X_{p,qr}^2 + Y_{p,qr}^2}$. Fig.2-7c shows a schematic of the relationship between the undeformed and deformed distances. The slope angle is $\phi = \cos^{-1}(\Delta_{1,qr}/\Delta_{2,qr})$. Deflection is then simply $w = \sin\phi$. All the distances were computed based on pixel length and we will have to convert pixels into real distance. Note that we obtained $\Delta_{p,qr}$ in pixels which is equivalent to real distance $\Delta^*_{p,qr} = 20$ mm.

2.2 Measurement of Natural Frequency Using a Laser Vibrometer

Section 1.1 considered previous works that showed the first resonant frequency has considerable effect on the aerodynamic performance of flapping structure. We also need to compare the results and characterize the respective mechanical properties for the handheld fans and the homogeneous plates using the same metric. Thus we choose their natural frequency, ω_n as the common mechanical property. This data will also help us better understand the effect of the change of structural features on the resonant frequency. The set up to measure the natural frequency of the fans and plate is shown in Fig 2-8.

The fan (or plate) is periodically excited from a frequency of $f = 2-20$ Hz with an electromagnetic shaker (Modal Shop 2075E). In order to find the natural frequency we need to be able to measure the response of the fan tip under vibration. The fan clamps (the respective clamps will be presented in Section 2.3) were connected directly at the base to the shaft of the shaker. An accelerometer (PCB Piezotronics

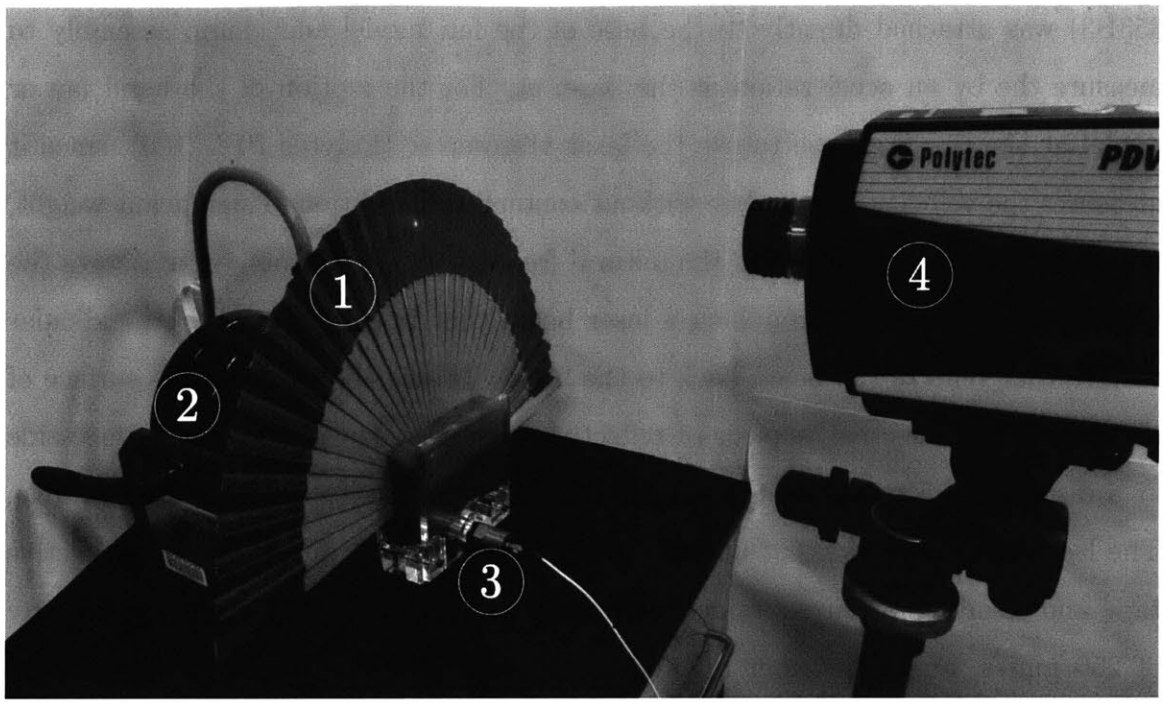

Figure 2-8: A fan (1) is driven by a electromagnetic shaker (2). The base acceleration is measured by an accerlerometer (3) and the velocity of the fan tip is measured with an laser vibrometer (4).

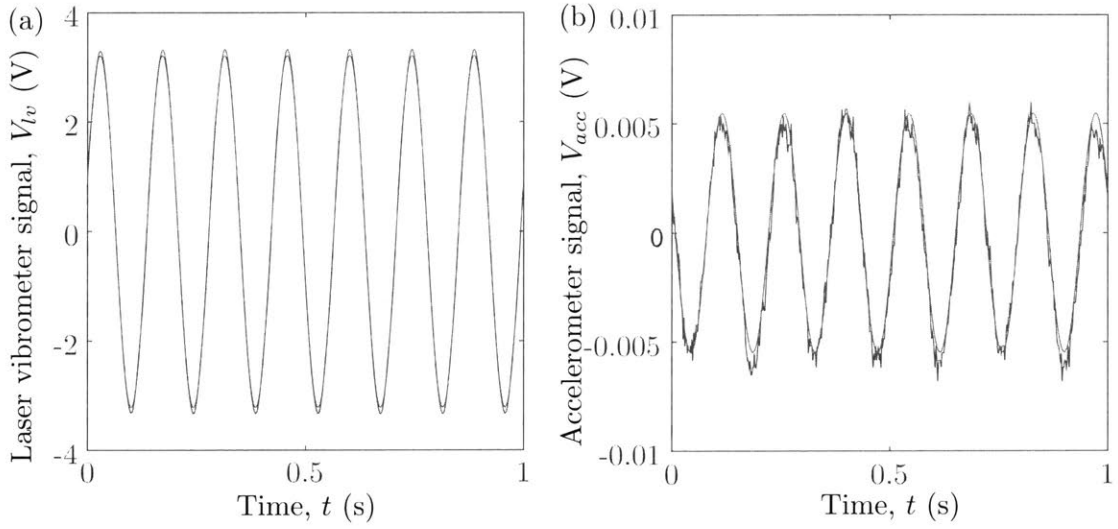

Figure 2-9: Example of signal (blue line) from (a) laser vibrometer and (b) accelerometer. The signal is fitted to a sinusoidal function (red line) using least root mean square. The specimen is a semi-circular flat plate $R = 200$mm, $h = 762\mu$m, vibrating at f=7Hz.

353B3) was attached directly to the base of the fan/model and clamp assembly to measure the by an acceleration at the base, a_b. For the motion of the hand fan or model at the tip, we chose to use the laser vibrometer (Polytec PDV 100), since it measures the velocity of a surface without contact and addition of significant weight, thus it would not interfere with the natural frequency. The vibrometer measures the velocity of a surface by producing a laser beam that is directed to a perpendicular surface that reflects the beam back to the laser vibrometer. To make the surface of the fan/model reflective, a piece of reflective tape was attached on to the face side at a distance of 5 mm from the tip and along the symmetry line of the semi-circle. The laser vibrometer was set up such that the laser points directly at the reflective tape and clear signals are obtained. The laser vibrometer is also limited to velocity of 250 mm/s, and the shaker amplitude was kept low. The laser vibrometer can work for frequencies up up 22 Hz accurately and we rejected results from models with natural frequencies higher than 22 Hz. Again the signals from the laser vibrometer and the accelerometer are digitized using the USB-6002 DAQ and recorded using a customized LabView program.

Fig. 2-9 shows an example of the signals obtain from the laser vibrometer and accelerometer. The signals from the DAQ and recorded in Labview are in voltages (V). The manufacturer provided conversion of the signal from the laser vibrometer to velocity is 1V= 125 mm/s while the manufacturer calibrated conversion of the signal from the accelerometer to acceleration is 0.0989V= 1g. The voltage signal from the laser vibrometer is V_{tip} while the voltage signal from the accelerometer is V_b. The two sets of data are synchronous in time and the data was fitted to a sinusoidal function using Matlab. We then derived phase and amplitude by fitting the signal to a sinusoidal function such that $V_{tip} = V_{tmax}\sin(2\pi t + \phi_1)$, $V_b = V_{bmax}\sin(2\pi t + \phi_2)$ and the phase difference is given by $\phi = \phi_1 - \phi_2$, which will be corrected to fall within $0 \leq \phi \leq 2\pi$. V_{tmax} and V_{bmax} are converted to u_{tmax}, the amplitude of the velocity of the fan tip, and a_{bmax}, the amplitude of the acceleration of the base of the fan, respectively. The maximum acceleration of the fan tip is then $a_{tmax} = 2\pi f u_{tmax}$. With the amplitude data we calculated the amplification factor at each frequency, which

is simply given as $A = a_{tmax}/a_{bmax}$. In Section 3.1 and Section 4.1.2 presents the measured natural frequency of the flat plates and, hand fans and models respectively

2.3 Experimental Specimens

We first conducted a search for various types of commercially available hand fans and observe the features of their designs, which we found to vary widely. In Section 2.3.1, we will rationalize our choice of using Spanish style hand fans for the study. Since we do not have control over the material properties and sizes of the hand fans, we want to fabricate model fans which we have control over those parameters. We fabricated three different types of model fans to understand the effect of structural features. In Section 2.3.2, we describe the fabrication procedure for the semi-circular flat plates, and its clamps, that will be used as simplified model systems for the hand fan. The mechanical feature we are exploring here is the effect of the thickness and hence the flexural stiffness of the fans. To study the ribs and leaves features found in foldable hand fan, we designed and fabricated a model fan made out of discrete flat sector-shaped plates described in Section 2.3.3. Finally, due to the foldable nature of the hand fans we can describe the folds as corrugation and we will describe the method we used to impose the geometry on the semi-circular plates in Section 2.3.4.

2.3.1 Materials and Structures of Spanish Hand Fans

As an initial screening process for the type of hand fans to be tested, we acquired a variety of commercial hand fans of different designs, almost all of them were of the foldable Chinese/Japanese and Spanish style. Most of the fans we collected are constructed out of stiff structural members, known as the ribs, usually made of wood or plastic, connected at the fan tip with compliant thin materials, known as leaves, usually made with cloth, paper or thin plastic sheets. Besides the the materials used to construct the fans, angle of the fully opened fans is also of importance; the Chinese/Japanese style of foldable hand fan when fully opened up forms a quadrant smaller than a semi-circle (*e.g.* Fig. 2-10a,c), which turns out to be another param-

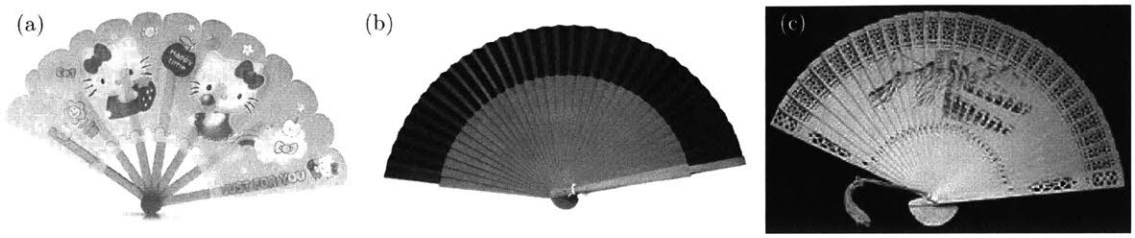

Figure 2-10: (a) A Chinese style plastic ribs and leaves hand fan with only seven ribs (b) A Spanish style wood ribs and cloth leaves hand fan with overlapping ribs (c) A Chinese style wood ribs hand fan without leaves with intricate through cuts on the ribs.

eter for consideration. The Spanish style fans on the other hand (*e.g.* Fig. 2-10b), though has the same ribs and leaves construction, open to a full semi-circular shape, eliminating the angle as a parameter. We will refer to the semi-circular surface side of the fully open hand fan as the *face side.*

The spacing between successive ribs and the size of the fold of the leaves is another factor to consider. If the number of ribs is small, the ribs are sparse circumferentially and thus the projected area of the fan changes significantly and difficult to estimate (*e.g.* Fig. 2-10a). Spanish style of fan also tends to have higher number of sticks such that each stick overlaps with adjacent ones, leaving the projected area of the fan to be exactly the same as a semi-circle (*e.g.* Fig 2-10b). Another common feature in some of the fans have intricate cuttings on the ribs both altering the projected area of the fan and the bending stiffness of the ribs (*e.g.* Fig. 2-10c) adding a problem of the effect of porosity, which is beyond the scope of this thesis.

The study began to focus on the Spanish style of fans and that brought the attention to a famous fan shop, Casa de Diego, in Madrid, Spain, that sells high quality and hand made Spanish style fans. From the conversation with the owner of the shop, we know that their collection of unembellished Spanish style hand fans is fabricated consistently and the source of materials for were also well documented. Even though the fans in the collection has very similar geometries, there are variations in terms of the size of the fans, choice of wood for the ribs and the thread counts for the leaves. The fan makers claimed that based on their experience, the "best" fans

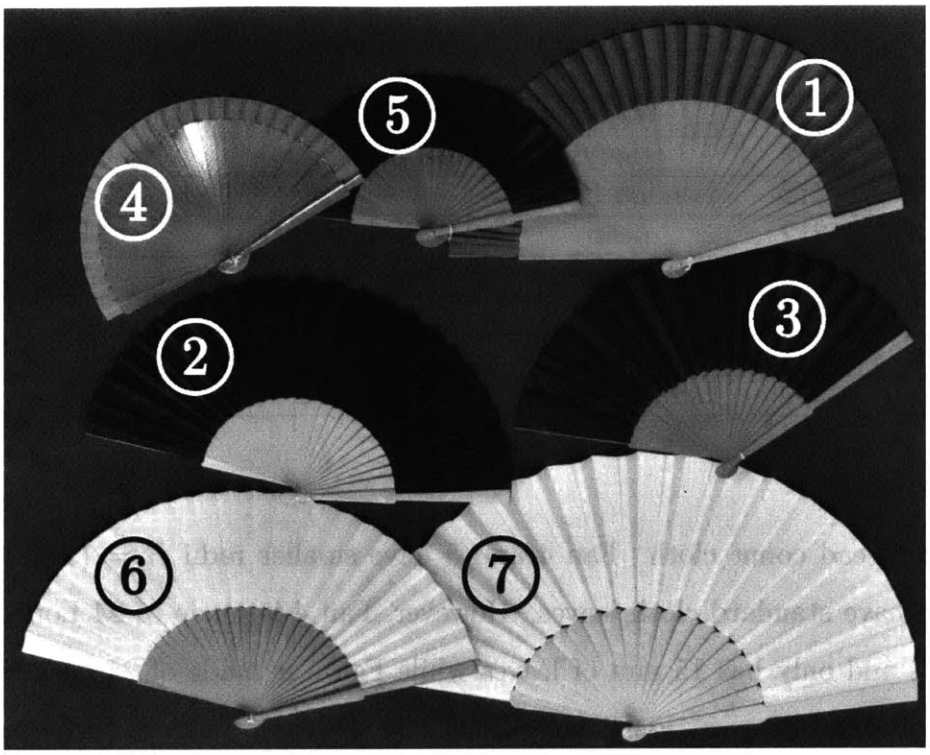

Figure 2-11: Pictures of the seven fans obtained from Casa de Diego (face side).

of this series tend to be made with wood from fruit trees, such as orange or pear, as they are strong yet flexible and London plane tree wood is also often used. We found that the typical Young's modulus of wood from pear tree is indeed the lowest at 7.8 GPa, followed by London plane tree at 8.9 GPa and then orange tree at 11.6 GPa [55]. High thread count cloth are also preferred as the threads are more closely weaved, thus reducing the effect of porosity, and was thought to be able to generate flow more efficiently.

Based on this information, we obtained a collection of seven fans shown in Fig 2-11 with their properties summarized in Table 2.3.1. Fans 1, 2 and 3 are of the same size with radii $R = 212$ mm. Fan 1 has 34 orange wood ribs and standard cloth leaves that only covers the outer 40 mm of the fan. The leaves section is half the length of the leaves of Fan 2 and 3. Fan 2 and 3 have the same geometry, but are made of different materials. The 24 ribs of Fan 2 are made out of wood from London Plane tree and the leaves out of standard thread count cloth. Fan 3 is made with pear wood

Table 2.1: Properties of commercial hand fans

Fan	R (mm)	Wood	Cloth thread count	Number of ribs
1	212	orange	standard	34
2	212	London Plane	standard	24
3	212	pear	high	24
4	144	London Plane	standard	24
5	137	pear	standard	24
6	244	pear	high	30
7	300	London Plane	standard	20

and high thread count cloth. Fan 4 and 5 have smaller radii $R = \{144, 137\}$ mm and both have standard cloth leaves. However, Fan 4 is made of 24 London Plane wood ribs and only has 15 mm of leaves while Fan 5 is made of 24 pear wood ribs and has 60 mm of leaves. Fan 6 has radius $R = 244$ mm, made with 30 pear wood ribs and high thread count cloth. Fan 7 has radius $R = 300$ mm and has 20 London Plane wood ribs and standard cloth. It seems that other than the materials used, the ratio of the length of leaves to the overall length of the hand fans may be another important feature. In our flow generation experiments, we focus on the first three hand fans, which are of the same size but have slight differences in their structure and materials.

The geometry of the hand fan is rather complex, especially at the base of the fan. In order to test the fan we constructed a simple clamp that can hold the fan open, while not applying breaking them with excessive force. Rigid clamps fabricated through using 3-D printing require a high resolution 3-D CAD of the fan since they need to match the surfaces of the fan perfectly. Given the high number of ribs in Spanish style fans, it is unrealistic. The clamp (Fig.2-12b) is made by attaching two acrylic plates to two connecting clamps (Fig. 2-12a) to the shaft. The distance between the two acrylic plates is 63.5 mm, which is thicker than the hand fans. A compliant material that can conform to the shape of the fan is then required to fill up the space between the fans and the plates, but yet has sufficient stiffness to impose a fixed boundary condition at the root. Polyurethane foam sheets with Young's

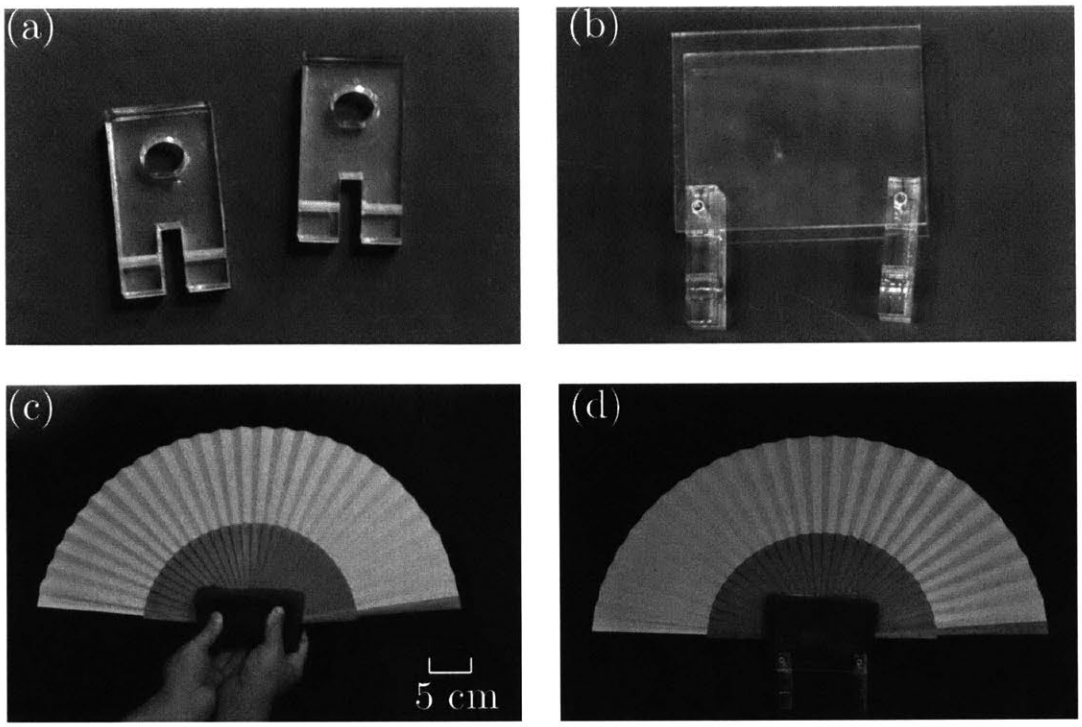

Figure 2-12: (a) Connector clamps to the rotating shaft (b) Acrylic plates attached to the connector clamps (c) Polyurethane foam wrapped around the hand fan (d) Foam and fan inserted between the acrylic plates.

Modulus of approximately 4000 Pa were used to wrap around the fully opened fan (Fig.2-12c) before being inserted them between the acrylic plates, as shown in Fig.2-12d. The foam becomes stiffer under compression and the fan remains in the same position even after high amplitude oscillations.

2.3.2 Fabrication of Flat Semi-circular Plates

As a baseline for flow generation, we want to test fans that have constant thickness over the entire surface. The semi-circular shape is picked since that is the projection of the face side of the hand fans. We fabricated semi-circular flat plate out of acrylic and polyethylene terephthalate (PETG) by laser cutting them out from a larger sheet of material using a LaserPro Spirit laser printer at the fabrication lab in Civil and Environmental Engineering department in MIT. Plates of two plates radii were fabri-

cated, $R = \{120, 200\}$ mm where the later was chosen because of the similar relative size to Fan 1-3. The former was chosen to correspond in size to the smaller Fan 4 and 5.

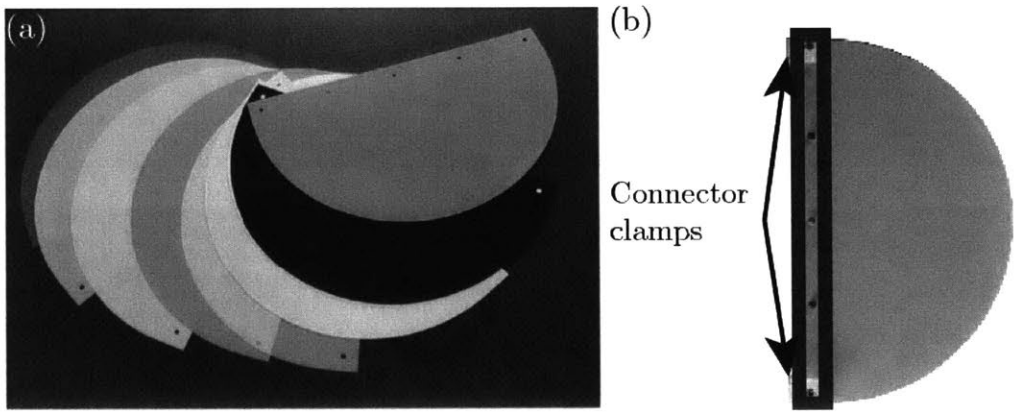

Figure 2-13: (a) Photo of the 120 mm semi-circular fans made from PETG of a range of thicknesses. (b) Photograph of the face side of a semi-circular plate fan of thickness $h = 762\,\mu$m and $R = 200$ mm with acrylic strips (blue box) and the connector clamps attached at the holes on the two ends.

The bending stiffness of the plates can then be changed systematically by using sheets of different thicknesses, since the flexural stiffness $B = Eh^3/12(1-\nu^2)$, where E is the Young's Modulus of the material and h is the thickness of the plate. The plates with $h = \{1588, 3175\}\,\mu$m were made out of acrylic (E=3.5 GPa, ρ_p=1180 kg/m^3) and the plates with $h \leq 1016\,\mu$m were made out of PETG (E=2.2 GPa, ρ_p=1270 kg/m^3). Plates of $R = 120$ mm (Fig. 2-13a) were made out of PETG plates of thicknesses $h = \{50, 76, 102, 127, 191, 254, 281, 508, 762, 1016\}\,\mu$m while plates of $R = 200$ mm were made with both PETG and acrylic plates of thicknesses $h = \{102, 127, 191, 254, 281, 508, 762, 1016, 1588, 3175\}\,\mu$m. An additional 2 cm was extruded at the base (flat) side of the semi-circular plates and five equidistance holes were cut in the extruded section, as indicated in Fig. 2-13b . We also laser cut two acrylic strips of thickness $h = 3175\,\mu$m, corresponding to the shape of the extruded section and they were fastened on each side of the plate with nut and bolt at the middle three holes. The two extreme holes were used to attach the fan to the connecting clamps.

2.3.3 Fabrication and Design of Discrete Model Fans

In hand fans, we can view the structure as stiff discrete beams (ribs) connected together at one singular point at the base. At the fan tip, the beams (ribs) were connected with adjacent beams (ribs) with a compliant materials. This construction means that there are two additional degree of freedom: the rotation of the beams (ribs) about the point of connection and twist of the individual beams about the axis running along the length of the beam.

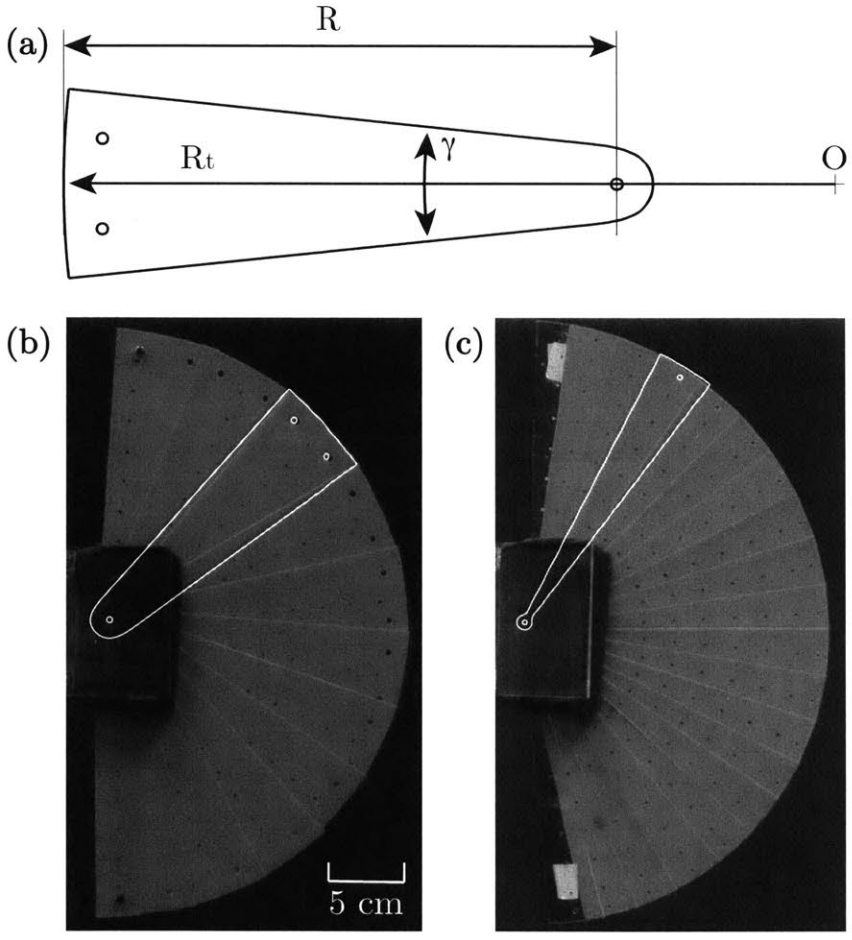

Figure 2-14: (a) Vector drawing of the sector and the parameters used to define the sectors. Photograph of the face side of (b) Model Fan 1 with $R = 200$ mm, $R_t = 300$ mm and $\gamma = 12°$ (c) Model Fan 2 with $R = 200$ mm, $R_t = 200$ mm and $\gamma = 10°$.

In order to find the effect of this additional degree of freedom, we explored that by imitating the construction of the hand fan through creating a model fan made

with discrete plates to represent the ribs and nitinol wires to represent the compliant material at the fan tip. Sector-shaped strips shown in Fig. 2-14a were cut out of PETG sheets of $h = 760\,\mu$m. The sectors are symmetrical in the radial direction and the shapes were defined with the following parameters: the radius of the outline defining the tip of the hand fan R_t, the distance from the intersection between the outline of the fan tip and the line of symmetry to the hole at the base R (also the size of the hand fan) and the angle between the outline on the sides, γ. The hole at the base of the sector was where the strips were fasted together with one single nut and screw and was centered on the line of symmetry. Near the tip, one or two (depending on the width of the sector at the tip) small holes were cut and nitinol wires ($500\,\mu$m diameter) was sewed through the holes at the fan tip side to simulate the leaves of the hand fan. Each strip can rotate minimally about the connecting hole but its motion was limited such that the overlap with adjacent plates fall in the range of 1-5°. Although the model fan is not fully foldable, it emulates the structure when the fan is constrained to the fully open configuration.

2.3.4 Fabrication and Design of Corrugated Fans

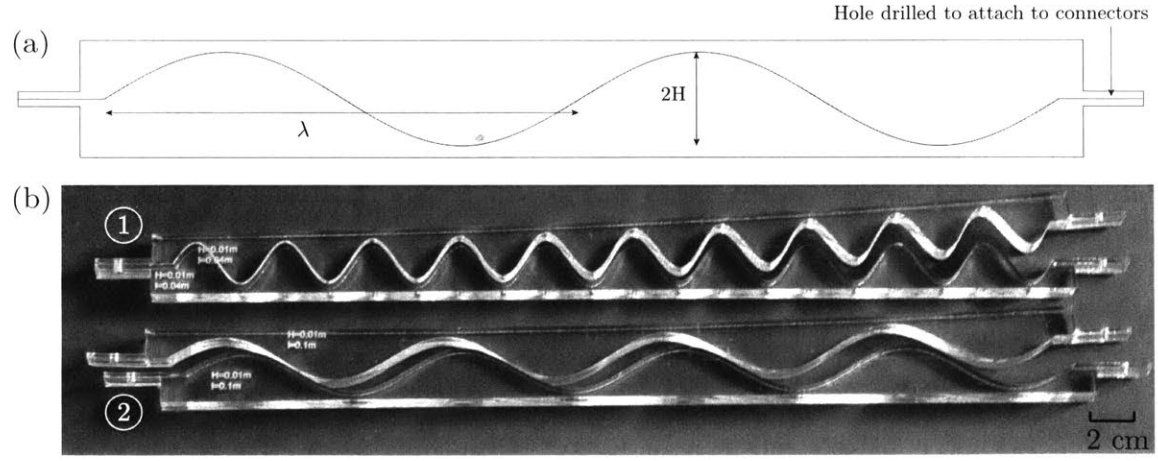

Figure 2-15: (a) Vector drawing of the corrugated clamp with the parameters shown (b) Photograph of two example corrugated fan clamps, (1) $H = 10$ mm and $\lambda = 40$ mm (2) $H = 10$ mm and $\lambda = 100$ mm.

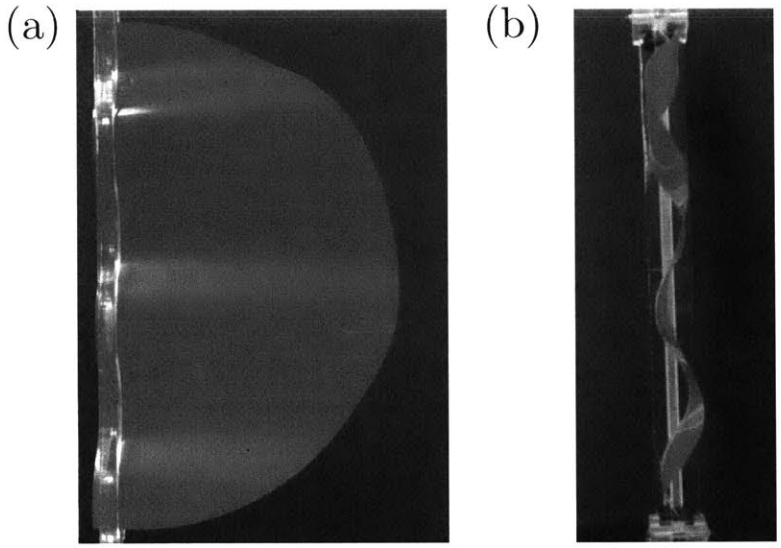

Figure 2-16: Photograph of the (a) face side and (b) thickness side of a corrugated fan with $R = 200$ mm, $h = 50\,\mu$m, $H = 20$ mm and $\lambda = 133$ mm

Corrugated plates were constructed by switching up the clamp of the flat semi-circular plate. The maximum thickness of plates used was $h = 191\,\mu$m, since making thicker plates conform to the shape of the clamp might result in irreversible deformation or failure. Clamps were laser cut using acrylic sheets of thickness 12.7 mm.

A sample vector drawing of the clamp is shown in Fig.2-15a and photographs of real clamps are shown in Fig.2-15b. Holes were drilled on the ends perpendicular to the thickness of the plate to fasten the clamp to the connector to the rotating shaft. The interface with the plate is defined by the shape of the corrugation, $z = H\sin(\frac{\pi y}{\lambda})$ where H and λ are the amplitude and wavelength of the corrugation respectively. Based on classic literature on corrugated plates, the second moment of inertia was calculated based on the geometry of the corrugation and was thought to depend strongly on the ratio $2H/\lambda$ [66]. More recent literature estimated the second moment of inertia based on average curvature of the surface and the second moment of inertial was found to be scaled by H^2t only [48, 37]. Fig. 2-16 shows the photograph of a semi-circular plate clamped to conform to the corrugated shape using the corrugated clamps fabricated.

2.4 Flexural Stiffness Measurement of Hand Fans

The bending stiffness of the fans cannot be easily calculated due to their complex structure and thus we measured it through experiments by performing a mechanical testing on the fans. The bending stiffnesses of Fans 1, 2 and 3 were estimated through a load-displacement mechanical test (Instron 5934, 10 N load cell). The displacement of the fan tip, δ, was increased incrementally up to 10 mm and the load, F required is measured (Fig. 2-17). Since we cannot place the contact point right at the tip, we set it at a point of 5 mm inwards from the tip; the radius of Fans 1, 2 and 3 are $R = 211$ mm, and the distance between the clamped end of the fan and the location of the applied load is $l = 206$ mm. An indenter with diameter of 3 mm was used. The bending stiffness values were estimated using classic theory for the linear deflection of a beam under point loading:

$$EI = \frac{Fl^3}{3\delta}, \tag{2.1}$$

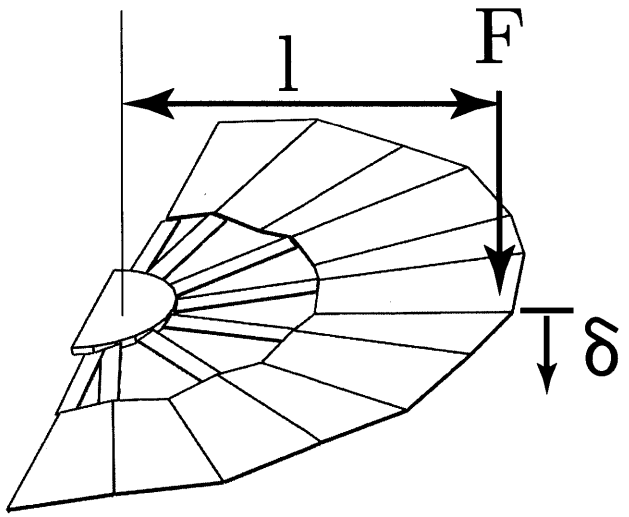

Figure 2-17: (a) Schematic of the point load experiment. The displacement of the fan tip, δ, is increased incrementally up to $10mm$ and the load, F required is measured

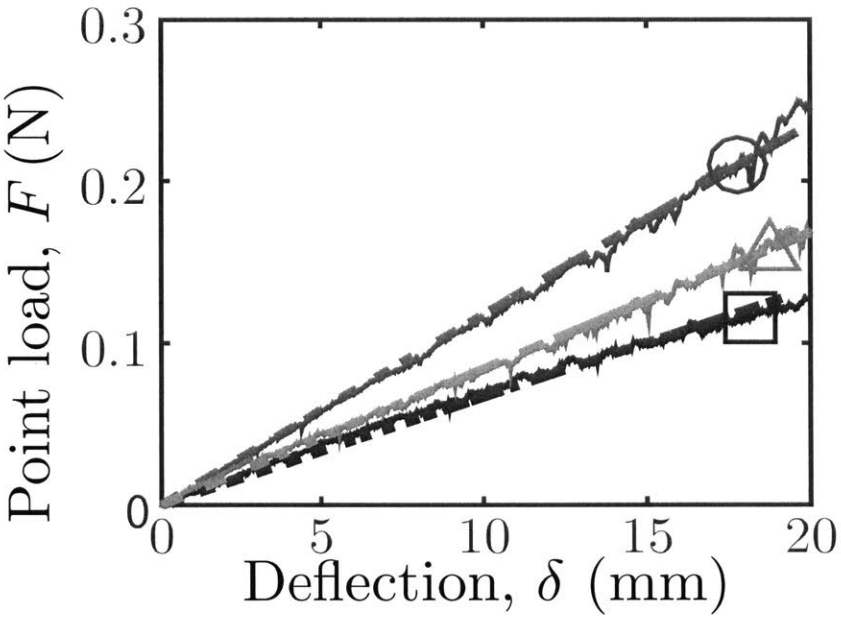

Figure 2-18: Point load for deflection of the tip of the hand fans up to 20 mm for Fan 1 (square), 2 (circle) and 3 (triangle)

where E is the Young modulus, I the area moment of inertia. The calculation of the moment of inertia, I for the hand fan is non-trivial due to several reasons. Firstly, the number of ribs is large, ranging from 20-30, each of them are like beams aligned to the radial direction and the effective stiffness has to be calculated in the direction of interest individually. Secondly, the ribs also interacts with each other due to partial overlap near the connecting points and forces are also transmitted through the stretching and deflection of the cloth leaves, which are not well characterized. Furthermore, there is a variation of thickness along each beam and while we can find that through measurement, it would be rather inefficient. While a creation of a model to derive the second moment of inertial of the fan is not unfeasible, it would be beyond the exploratory scope of the thesis, but could be of interest for detailed designs in the future. Since we also do not know the specific value of E due to the composite nature of the fan, we will perform the subsequent analysis of the fans based on EI.

Using the measurement setup described above, we found the force F required

to impose a deflection of δ at the point of contact. The graph of $F(\delta)$ versus δ is plotted in Fig. 2-18. We perform a linear fit of the data and obtain the slope which is F/l. The effective rigidity of Fans 1, 2 and 3 was measured to be $EI = \{2.24 \pm 0.02, 4.02 \pm 0.04, 2.76 \pm 0.03\} \times 10^{-2}\,\mathrm{Nm}^2$.

We note that although orange wood has the highest typical Young's modulus, the overall structure of Fan 1 (made from orange wood) is the most flexible. This is an indication that there is an overall structural effect, since Fan 1 has a larger "discrete" wood section (or smaller connected leaf section) than the other two fans. We will show later in Chapter 4 that the orange wood also generates the most flow among the hand fans, despite being the most flexible of the trio.

2.5 Outlook

We presented the experimental setup to measure the flow production and the natural frequencies of the hand fans and models, the selection of the hand fan and the method of fabrication and design of the semi-circular plate, discrete model and corrugated fans. The experiment specimens were tested using the procedure and setup described and we will aeroelastic behavior of the flat plates in Chapter 3. In Chapter 4, we will study the aeroelastic behavior of heterogeneous structures.

Chapter 3

Aeroelastic Behaviour of Flapping Flat Plates

In this chapter we present the flow and natural frequency measurement results for the semi-circular flat plates described in Section 2.3.2. We first evaluate the natural frequencies of the flat plate with the experimental set up described in Section 2.2 which allowed us to find the pre-factor that linked the geometrical parameters to the primary natural frequency and we evaluated the natural frequency of plates above the limitation of our apparatus. Velocity of the flow generated by plates were obtained using the hot-wire anemometer. Comparing the velocity fields of plates of different thicknesses and radii, we determined a location where we will place the hot-wire anemometer probe for the rest of the study. Tests were done by setting the same flapping frequency, but with increasing flapping amplitude. We normalized the generated velocity by the velocity of the fan tip and the natural frequency by the driving frequency and found an optimal when the normalized frequency is close to unity, which is consistent with past studies discussed in Section 1.1. Together with data from the torque sensor, we are able to evaluate a representative efficiency of the flapping motion. We then define plates as thick, thin and intermediate based on the normalized natural frequency and seek to understand the differences in variation of normalized velocity and efficiency with flapping amplitude by considering the order of magnitude of the moment terms.

3.1 Natural Frequency of the Flat Plates

From the literature review in Section 1.1, the resonant frequency is a critical parameter in the aerodynamic performance of a flapping plate. From the estimation of the vibration of a flat plate in Section 1.3, we recall that the characteristic frequency of a vibrating homogeneous plate is [70, 30]:

$$\Omega_p = k\sqrt{\frac{B}{\rho_p h R^4}}, \tag{3.1}$$

where $B = Eh^3/12(1-\nu^2)$ is the bending stiffness and k is a prefactor that depends on the geometry and boundary conditions. Also, we noted that analytical solution for the natural frequency of a rectangular plate was an assumption of the deflection mode shape that satisfies a fixed-free boundary condition. The actual solution depends on the geometry and thus would be easier to obtain an experimental solution for the flat plates. Some of the plates have natural frequencies that are much higher than the measurement range of our apparatus (up to 22 Hz or 138 rad/s), so we cannot measure the natural frequency for all the plates. Hence, we solve the problem by performing the vibration experiments using the apparatus presented in Section 2.2 for plates with natural frequencies lower than 22 Hz to obtain the pre-factor k.

Before conducting the tests on the plates, we want to ensure that the amplitude is sufficiently small such that we reduce the effect of damping from aerodynamic forces (dependent on velocity) and the effect of frequency shift from added mass (dependent on acceleration). To do that we conducted a series of vibration experiments on Fan 2 with increasing shaker amplitude and plotted the resultant amplification factor in Fig. 3-1a. The phase shift for all the experiments were also plotted in Fig. 3-1b. We see that for the range of amplitude considered, the amplification factor peak shifted minimally from the value of $\omega_s =\sim 85.5$ rad/s (13.6 Hz) at base amplitude of 0.125 mm to $\omega_s \sim 86.7$ rad/s (13.8 Hz) at base amplitude of 0.5 mm, while the phase shift reaches a value of π (where resonant occurs) narrowly between the band of $\omega_s = 83 - 88$ rad/s for base amplitude of lower than 1.5 mm. Hence, a value of

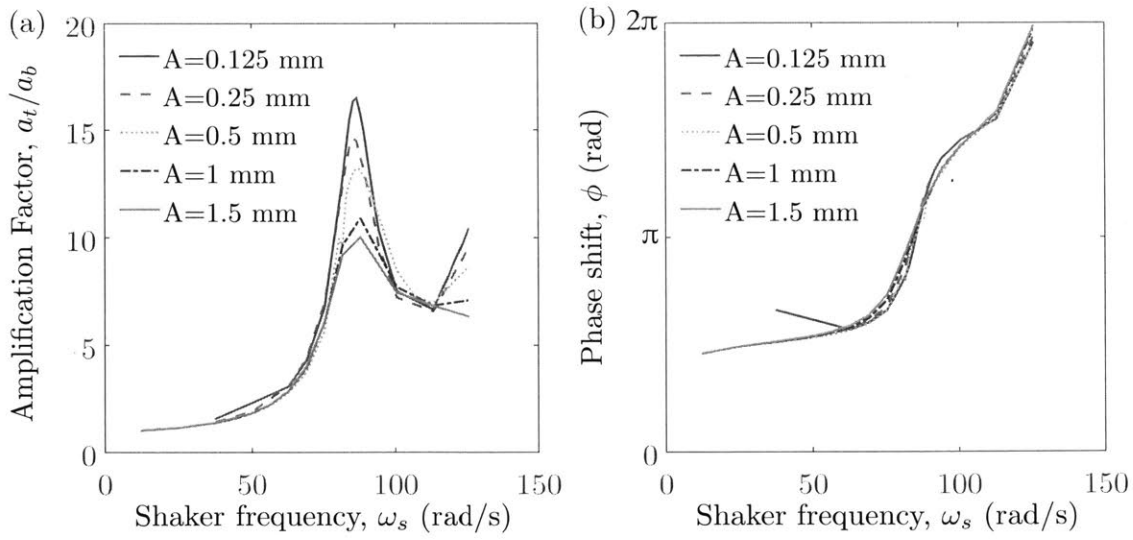

Figure 3-1: (a) Amplification factor, a_t/a_b and (b) phase shift over a range of shaker frequency for a range of different peak to peak amplitude at the base for Fan 2

$A = 0.5$ mm base amplitude was chosen for our experiments, since a pronounced peak was produced, while the frequency shift was small.

In Fig. 3-2a, we present three representative examples of the measured amplification factors as a function of shaker frequency ω for three representative plates of thicknesses $h = \{1016, 762, 254\}$ μm and $R = 200$ mm. We observed a sharp peak in amplification factor and the frequency at which the peaks occur are the natural frequencies. The natural frequencies of the plate of thicknesses $h = \{1016, 762, 254\}$ μm are $\omega_n = \{44.6, 32.0, 13.2\}$ rad/s . We obtained the natural frequencies for four other semi-circular plates using the corresponding plots and in Fig. 3-2b, we plotted the experimentally measured ω_n versus Ω_p, for our semi-circular plates (solid red circles). The data collapse onto a straight line, with a pre-factor $k = \omega_n/\Omega_p = 4.1 \pm 0.2$ (determined by fitting, for ω_n in rad/s), confirming our experimental method to determine ω_n for plates. There are also plates, thicker and smaller, that have natural frequencies much larger than 22 Hz (138 rad/s). Since we do not have the necessary instruments to measure those frequencies accurately, we will be using pre-factor $k = 4.1$ and Eq. (3.1) to estimate the natural frequencies for plates and fans with resonance higher than the range of the laser vibrometer (22 Hz). In Section 2.2, we

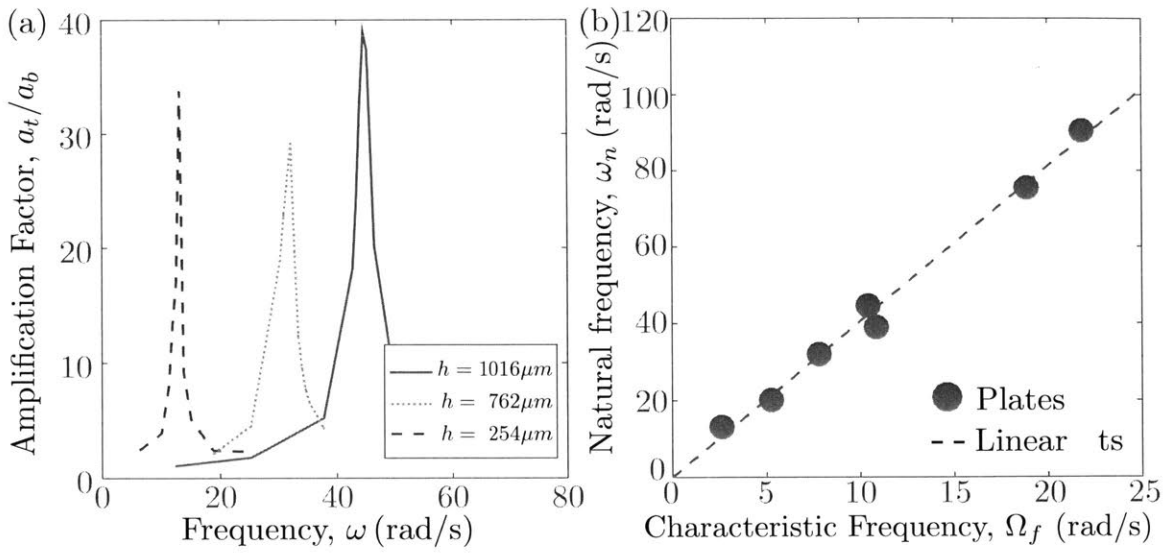

Figure 3-2: (a) Frequency response curve of three semi-circular plate with R=200mm and $h = \{1016, 762, 254\}\mu$m. (b) Natural frequency of semi-circular plates (red circles) versus the relevant characteristic frequency, Ω_f

estimated the pre-factor for a rectangular plate of similar dimensions to be $k_{rec} = 3.51$ by assuming a deflection mode shape of

$$W = \sin\left(\frac{n\pi y}{b}\right)\sin\left(\frac{m\pi x}{a}\right) - \left(\frac{m\pi x}{a}\right)\sin\left(\frac{n\pi y}{b}\right). \tag{3.2}$$

The value of the measured and the estimated pre-factors are close and the higher natural frequency for the measured value is higher because the semi-circular plate has smaller mass as compared to the rectangular plates, but both geometries have the same flexural stiffness B. Thus, it is reasonable to assume the plate deflection to be

$$\xi = w_0 L\alpha \sin(\omega t)\sin(\frac{n\pi}{R}x) - w_1 x, \tag{3.3}$$

where w_0 and w_1 are scaling parameters.

3.2 Phase Averaged Velocity and Vortex Generation

Before conducting the series of experiments to parametrically changing the thickness of the semi-circular plate, we need to understand the phenomenological behavior of how flow is produced. The phase average velocity is defined,

$$\tilde{u}\left(\frac{t}{T}\right) = \frac{1}{n}\sum_{1}^{n} u(t+nT), \tag{3.4}$$

where t is time, $T = 2\pi/\omega$ is the driving period and $n \geq 30$ is the number of oscillations. Experiments were conducted at over 125 locations on the x-y plane indicated in Fig. 2-1b, using the set up as described in Section 2.1. The hot wire anemometer was set perpendicular to the axis of rotation, at 5 distances from the fan tip $d = [10, 30, 50, 80, 120]$ mm and 25 angles $-48 \leq \theta(^\circ) \leq 48$ at 4° intervals from the mid point of the flapping tip motion. Using the encoder data from the torque sensor, the phase average velocity field at each of the point can be matched to the motion of the fan. Thus we can pick an instantaneous position of the fan and obtain the velocity for all 125 points to create a velocity field. The snapshots of the velocity over half of the oscillating period shown in Fig. 3-3. For each snapshot, the position of the fan tip is indicated by the solid black line. The colors correspond to a range of 0 to 0.3 m/s (see adjacent color-bar in Fig. 3-3).

As the fan moves from its position at $t/T = 0$, a high velocity region is produced near the fan tip as it sweeps across and at $t/T = 0.125$, we see higher velocity of ~ 0.2 m/s at $\theta = 0^\circ$ and $d \sim 10$ mm, but the core of the vortex is not visible on the velocity field as it is in the path of flapping plate. The velocity at $\theta = 0^\circ$ and $d \sim 10$ mm builds up to the maximum of ~ 0.3 m/s as the tip of the fan slows down to a stop at $t/T = 0.250$. This is known as the *stopping vortex* [61, 57]. As the fan moves away from the extreme position at $t/T = 0.250$ to $t/T = 0.375$, another vortex is formed on the right side of the map with the velocity at $\theta = 24^\circ$ and $d = 10$ mm is ~ 0.3 m/s. This is the *starting vortex* [61, 57].

As the fan moves towards $\theta = 0^\circ$ at between $t/T = 0.0375$ and $t/T = 0.500$, the

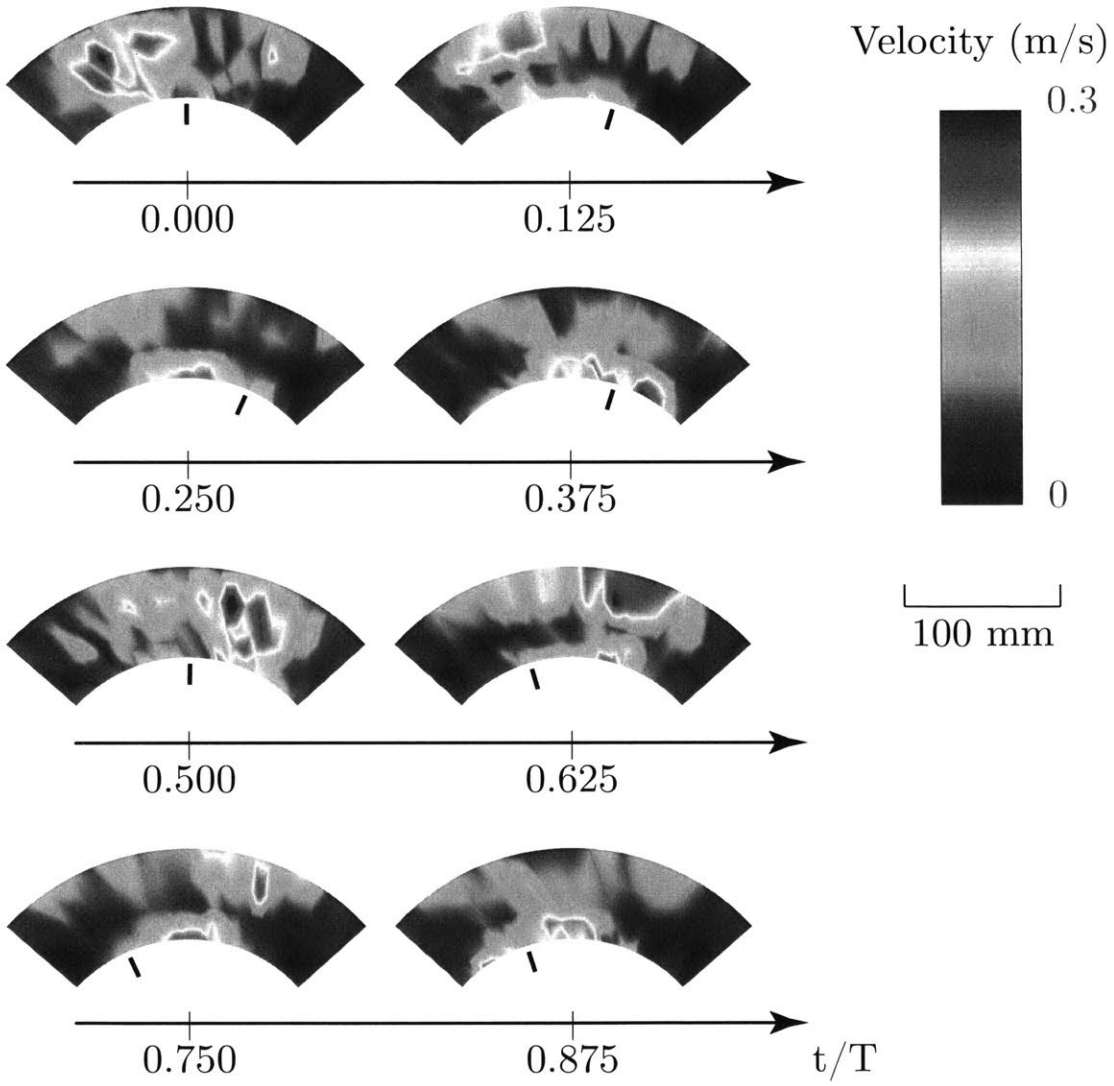

Figure 3-3: Phased averaged fields showing the instantaneous velocity $u(t)$ at different time indicated by t/T for a plate of radius $R = 120\,\text{mm}$, thickness $h = 127\,\mu\text{m}$ driven at a frequency $\omega = 12.6$ rad/s (2 Hz), and an angular amplitude $\alpha = 24°$. The position of the tip of the fan is indicated for each time-step by the solid black line.

starting and *stopping* vortex pair then moves away from the fan tip. The velocity of the vortex pair moving away from the fan tip is known as the induced velocity. We observe from the velocity field at $t/T = 0.5$ that the vortex pair centers around $\theta \sim 24°$, the same angle as the angular amplitude of $\alpha = 24°$, and $d \approx 80$ mm. The vortex then continues to move further and moves to $d \approx 100$ mm and $\theta \approx 24°$ at $t/T = 0.625$, moving a distance of $\delta d_v = d_v(t/T = 0.625) - d_v(t/T = 0.5) \approx 20$ mm over a time period of $\delta t/T = 0.125$ or $\delta t = 0.0625$ s. Thus the speed at which the vortex pair moves or induced velocity is given by $U_{induced} = \delta d_v/\delta t \approx 0.02/0.0625$ m/s $= 0.32$ m/s. The process repeats as the position of the fan is now at negative values of θ and similar behavior was observed for $t/T \geq 0.5$. After the last frame at $t/T = 0.875$, the process loops back to $t/T = 0$. Smaller intervals of d and θ would be required If we want a more accurate estimate of the induced velocity. While it is possible to characterize the flow generated by the flapping fan by finding induced velocity, we would be required to produce the phase average velocity field for every single test cases. It would not be a realistic approach for our purpose and we have to find the most representative location to place the probe.

3.3 Placement of Hot-Wire Anemometer Probe

To simplify the problem, we used the phase velocity data in Fig.3-3 to determine the best position for the placement the hot-wire anemometer probe. We averaged the velocity field for all t/T in the previous section for each of the 125 positions tested. This process was carried out for plates of thicknesses $h = [51, 127, 254, 762]\,\mu$m and radius $R = 120$ mm, driven at a frequency $\omega = 12.6$ rad/s (2 Hz), and an angular amplitude $\alpha = 24°$. The average velocity field for the plates are shown in Fig. 3-4. Similar velocity fields were also obtained for plates of radius $R = \{200\}$.

There are two locations on the averaged velocity fields where higher velocities were measured. The first location is for small angles around the center of the flapping motion and close to the trajectory of the fan tip, which is $-12° \leq \theta \leq 12°$ and $d \leq 30$ mm for the plates of $R = 120$ mm flapping at an amplitude of $\alpha = 24°$. We tested the

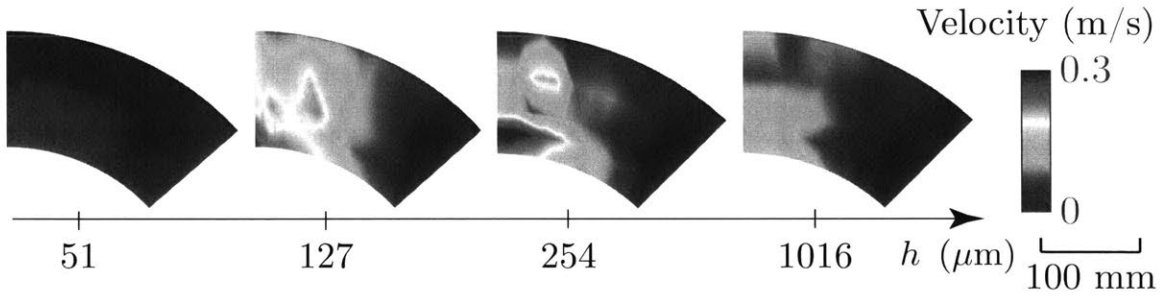

Figure 3-4: Time averaged velocity fields showing the average velocity U for plates of different thicknesses of plates $h = [51, 127, 254, 762]\,\mu$m, radius $R = 120\,$mm driven at a frequency $\omega = 12.6$ rad/s (2 Hz), and an angular amplitude $\alpha = 24°$.

larger plates and a range of flapping amplitude and find that this also happens in the region defined by $-\alpha/2 \leq \theta \leq \alpha/2$ and $d \sim 0.25$ R. This region is observed across all the cases we tested, even when the velocity is relatively low throughout the data (*e.g.* for the case $h = 51\,\mu$m, $R = 120$ mm, $\omega = 12.6$ rad/s (2 Hz) and $\alpha = 24°$ shown in Fig. 3-4). The second location occurs at distance of $d \sim 50 - 80$ mm and at $\theta \sim \alpha/2$ for plates of $R = 200$ mm and $h = \{127, 254\}\,\mu$m. For plates of $h = \{51, 1016\}$, this second region of higher velocity were not observed. The observation of whether the second region of high velocity occurs correlates with the value of velocity measured at $-12° \leq \theta \leq 12°$ and $d \leq 30$ mm. The second regions of higher velocity is not observed for many plates and its location is not well defined based on our available data. It is then reasonable to chose a point within the first region, which we defined $-\alpha/2 \leq \theta \leq \alpha/2$ and $d \sim 0.25$ R, for the placement of the hot-wire anemometer. As the flapping amplitude can be as small as $\alpha = 8°$ and velocity values are the highest at points closest to the fan tip, we picked the mid point of the flapping tip motion ($\theta = 0°$) and a distance $d = 0.1R$ as a representative location to measure the flow.

3.4 Flow Generation and Power Efficiency of Flapping Flat Plate

In this section, we present the analysis of the measured velocities, generated by the plates at the location selected in the previous section, on all the semi-circular plates

described in Fig. 2.3.2. We normalized the measured velocity with and the natural frequency with the flapping frequency and found that the optimal normalized velocity indeed occurs when the normalized natural frequency is unity. Together with the data from the torque sensor and encoder, we also defined the input and output power terms which gives us the efficiency of the plates. The variation of normalized velocity and efficiency with angular amplitude also depends on the normalized natural frequencies. We then turn a modified version of the Euler-Bernoulli equation and considered the order of magnitude of the contributing moments of the equations to help us rationalize the dependence on flapping amplitude.

3.4.1 Velocity of Generated Flow

From the time-series of the instantaneous velocity, $u(t)$, we define the average velocity of the generated flow:

$$U = \frac{1}{n}\sum_{1}^{n}\frac{1}{T}\int_{0}^{T} u(t)dt, \tag{3.5}$$

where the averaging is done over $n \geq 40$ cycles. We define a length scale based on the velocity of the tip of the fan (assuming rigid motion) or the driving velocity, $V = \omega\alpha L$, where L is the length from the tip to the axis of rotation. Note that the distance between the base of the semi-circular fan to the axis of rotation is 45 mm, so $L - R = 45$ mm. The range of Reynolds number, $Re = VL/\nu$, explored was 250-5000, $\nu = 1.57 \times 10^{-5}\,\mathrm{m^2 s^{-1}}$ is the kinematic viscosity of air. We first start with testing the semi-circular, homogeneous, and elastic plate described in Section 2.3.2. This simplification enables a more systematic control over the relevant parameters, while decoupling the intricate structural details of the fan. We focus on plates with two radii values, $R = \{120, 200\}$ mm and eleven different thicknesses in the range $50 \leq h\,[\mu\mathrm{m}] \leq 3175$. All plates were tested using the apparatus shown in Fig. 2-1a, with the location of the anemometer determined from Section 3.3.

In Fig. 3-5, we plot the average speed of the generated flow, U, versus driving velocity, V, for three representative plates ($h = \{102, 254, 762\}\,\mu$m). Both the thickest and the thinnest plates ($h = \{762, 102\}\mu$m respectively), exhibit linear behavior,

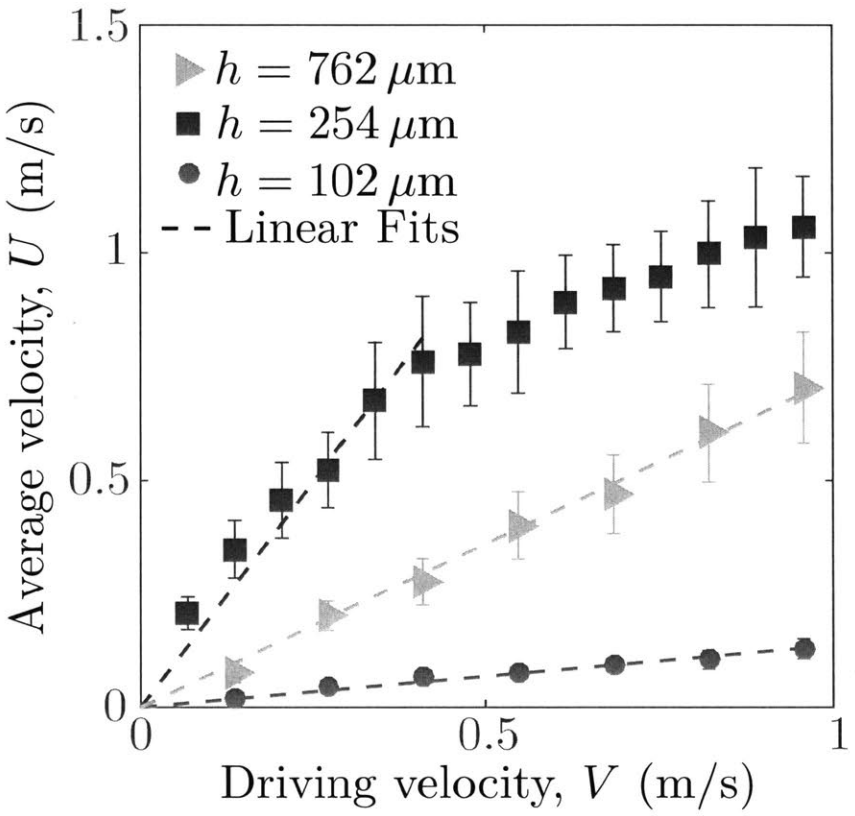

Figure 3-5: U versus V for semi-circular plates of $R = 200\,\text{mm}$ with three different thicknesses, h.

where $U \propto V$. On the other hand, for the intermediate-thickness plate ($h = 102\,\mu$m), the $U(V)$ dependence is nonlinear, even if a linear region can still be identified for $V < 0.4$ (corresponding to $\alpha < 24°$). More importantly, the average velocity of the flow generated by the intermediate thickness plate is significantly higher than the other two, further suggesting that there is an optimal bending stiffness to generate maximal flow output.

Next, we defined a normalized output velocity $\bar{u} = U/V$ and a normalized natural frequency $\bar{\omega} = \omega_n/\omega$ for plates. In Fig. 3-6, we plot the normalized output velocity $\bar{u}$ versus the normalized natural frequency $\bar{\omega}$ for plates of thicknesses $h = \{102, 127, 191, 254, 281, 508, 762, 1016, 1588, 3175\}\,\mu$m and radii $R = 200$ mm, driven at seven angular amplitudes where, $8° \leq \alpha \leq 56°$ at 8° intervals. From the graph, the maximum normalized velocity is found to occur when the driving frequency

matches the natural frequency of the plate: $\bar{\omega} \approx 1$. Away from this peak, the generated flow drops sharply to $\bar{u} \ll 1$ for $\bar{\omega} \leq 0.6$ and decreases towards the constant value of $\bar{u} \approx 0.70$ for $\bar{\omega} \geq 2$. Based on the behavior of the normalized velocity, we define *thin plates* for $\bar{\omega} \leq 0.6$, *thick plates* for $\bar{\omega} \geq 2$ and *intermediate plates* for $0.6 \leq \bar{\omega} \leq 2$.

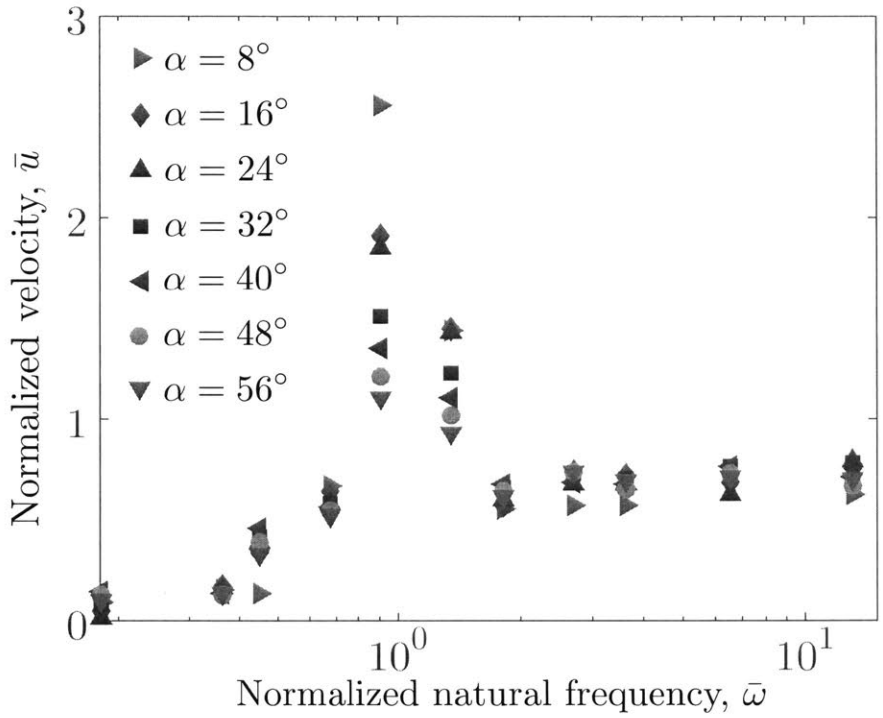

Figure 3-6: Dimensionless velocity of the generated flow, $\bar{u}$, versus normalized natural frequency, $\bar{\omega}$ for plates $R = 200\,\text{mm}$ at different amplitudes (see legend).

For both the thin and thick plates, the normalized output velocity $\bar{u}$ is independent of α and in this case, it means that $U \propto V \propto \alpha$. In the case of thick plates, the normalized velocity $\bar{u} \approx$constant, an indication that the plates have the same dynamics. In the limits of infinite thickness, the plates would be perfectly rigid. Thus we treat the plates in $\bar{\omega} \geq 2$ to be almost rigid or have small deflection. Thin plates however, have natural frequencies much smaller than the driving frequencies and while it is possible that higher modes, which can be estimated using an equation similar to Eq.(3.1) multiplied by m^2 where m is the mode number, could be excited, we did not observe another peak near $\bar{\omega} = 0.25$. Since the vortex generated is correlated to the effective

amplitude of the tip [42, 57], the smaller normalized velocity compared to the thick plate case indicates a reduction in the effective fan tip amplitude. Unlike the thick plates, the value of normalized velocity varies with normalized natural frequencies, we can conclude that the normalized shapes are different across the normalized natural frequencies. For the same normalized natural frequencies however, the deflections are independent of the flapping amplitudes. Interestingly, when $\bar{\omega} \approx 1$, $\bar{u}$ increases monotonically with decreasing α. The normalized velocity is as large as a factor of 4.5 at $\alpha = 8°$ to a factor of 1.4 at $\alpha = 56°$ when compared to rigid plates. This is an indication that the normalized deflection tip decreases with angular amplitude.

The above results demonstrate that flexibility is found to significantly enhance the aerodynamic performance of the plates during flapping, with maximal generated flow exhibited when the driving excitation occurs close to the natural frequency of the plate, which agrees with the findings from the other findings in literature. Counterintuitively, however, is that while the plates in the thin and the thick regimes are not affected by the flapping amplitude, plates in the intermediate regime are generating proportionally less flow with increasing amplitude. We will further discuss the effect of the flapping amplitude on deformation and consequently the flow generated in Section 3.5.1 by considering the order of magnitude of the forces acting on the plate.

3.4.2 Power Efficiency of Flat Plate

Our apparatus described in Section 2.1 also includes a rotatory torque sensor (Futek TRS 605) that, simultaneously to $u(t)$, acquires time-series of the torque, $\tau(t)$, applied at the driving axis, and its angular position, $\Theta(t) = \alpha \sin(\omega t)$. We find the phase average torque using

$$\tilde{\tau}\left(\frac{t}{T}\right) = \frac{1}{n}\sum_{1}^{n} \tau(t + nT), \tag{3.6}$$

and an example plot of the phase average torque vs. the normalized time t/T is presented in Fig. 3-7. The value of $t/T = 1$ represents a complete cycle. We then fit the data to a sinusoidal curve with equation $\tilde{\tau} = \tau_{max} \sin(\omega t)$.

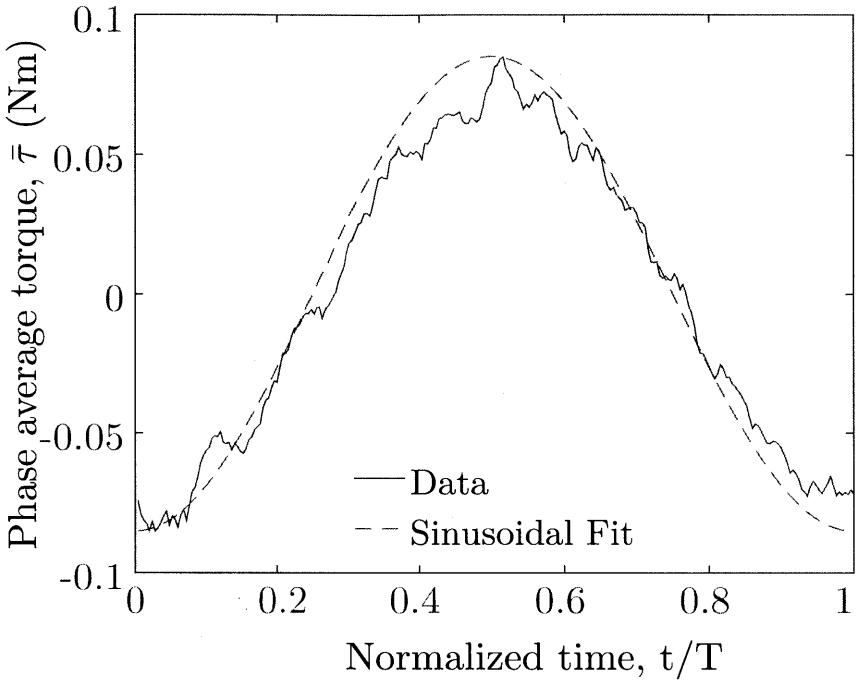

Figure 3-7: Phase average signal of torque measurement. For this signal, $h = 1016\,\mu$m, $R = 200$ mm.

With these data in hand, we define the flapping efficiency as the ratio of output and input powers,

$$\eta = \frac{P_{\mathrm{o}}}{P_{\mathrm{i}}}, \tag{3.7}$$

The input power is defined as

$$P_{\mathrm{i}} = \bar{\tau}\dot{\Theta}, \tag{3.8}$$

where $\bar{\tau}$ is the average magnitude of τ or $|\tau|$ over ≥ 40 cycles and

$$\dot{\Theta} = \mathrm{d}\Theta/\mathrm{d}t = \mathrm{d}/\mathrm{d}t\,\alpha\sin(\omega t) \sim \alpha\omega \tag{3.9}$$

is the angular velocity of the motion. The aerodynamic output power of the generated flow can be thought of a function of the volume, speed and density of air flowing through through a surface S, the area of the surface generated by the locus of the fan tip. A schematic of S is shown in Fig.3-8. The kinetic energy (KE) and power (P)

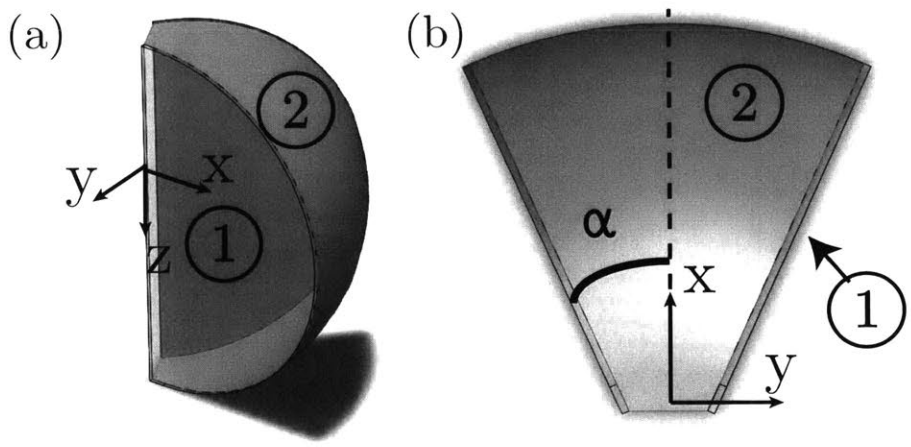

Figure 3-8: (a) An isometric view and (b) a top (x-y) view of a schematic illustrating the (1) maximum position of the fan and (2) location of surface area S.

of mass of air, m_{air} flowing at a velocity of U is given by

$$KE = 1/2 m_{air} U^2 \tag{3.10}$$

$$P_o = 1/2 \dot{m}_{air} U^2, \tag{3.11}$$

where $\dot{m}_{dot}$ is the mass flow rate. Since we are interested in the flow going through S, the mass flow rate crossing S with constant velocity U across the entire surface is

$$\dot{m}_{air} = \rho_f S U, \tag{3.12}$$

where ρ_f is the density of air. Thus we estimate the power output as

$$P_o \approx 1/2 \rho_f S U^3, \tag{3.13}$$

Note that the estimation of P_o is only valid at the level of scalings; a more detailed calculation would require measured data of U at many different locations close to the plane of S, before integrating the value over the entire surface. While it is theoretically possible to do so, it does not add value to our understanding of the efficiency of the flapping fan.

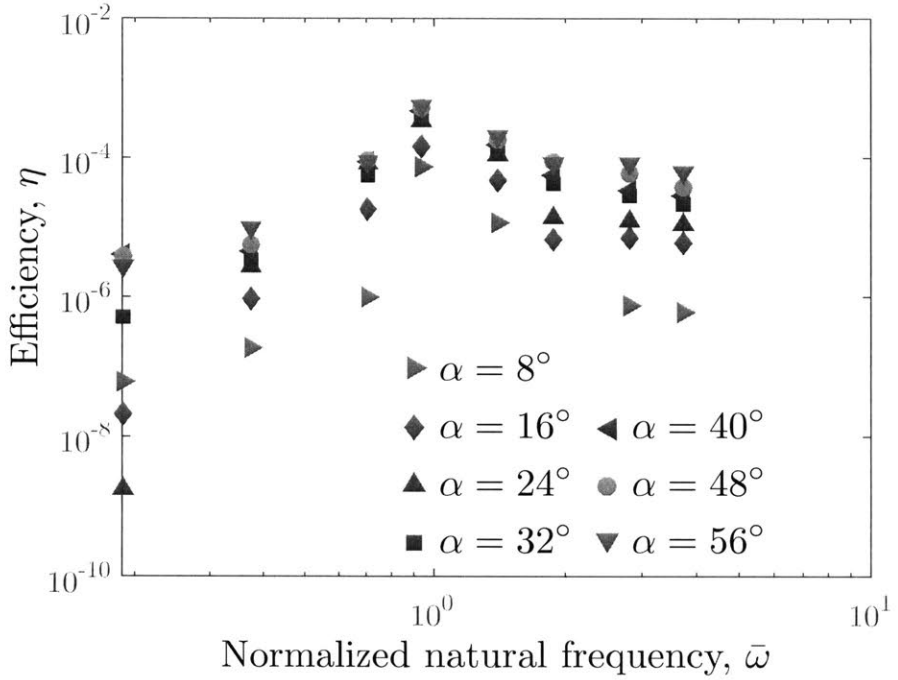

Figure 3-9: Efficiency η of semi-circular plates ($L = 200\,\text{mm}$) versus normalized natural frequency $\bar{\omega}$.

We plot in Fig.3-9 the efficiency η against the normalized natural frequency $\bar{\omega}$. Similar to the normalized velocity, we see that the overall maximum efficiency of $\sim 5.5 \times 10^{-4}$ occurs at $\bar{\omega} \approx 1$ and $\alpha = 56°$, which is in line with the position of the peak of the $\bar{u}(\bar{\omega})$ data shown in Fig. 3-6. However, the efficiency increases with flapping frequency, which is in reverse to the normalized velocity. The peak drops sharply by almost two order of magnitudes away from the plates. For the thick plates, the efficiency slow decreases with $\bar{\omega}$. Since the output power P_o is similar across the $\bar{\omega} \geq 2$, the decrease is due to the increase in input power P_i. Experiments were conducted using the same flapping frequency, hence the decrease in efficiency is due to the increase in torque. Meanwhile for the thin plates, the efficiency quickly drops in order of magnitude, as $\bar{\omega}$ decreases.

In Fig. 3-10 we present plot of the efficiency η against angular amplitude α for four plates with thicknesses in the range $h = \{102, 254, 381, 762\}\,\mu\text{m}$ and $R = 200$ mm. We observe that the efficiency η increases monotonically with α. For the thinnest

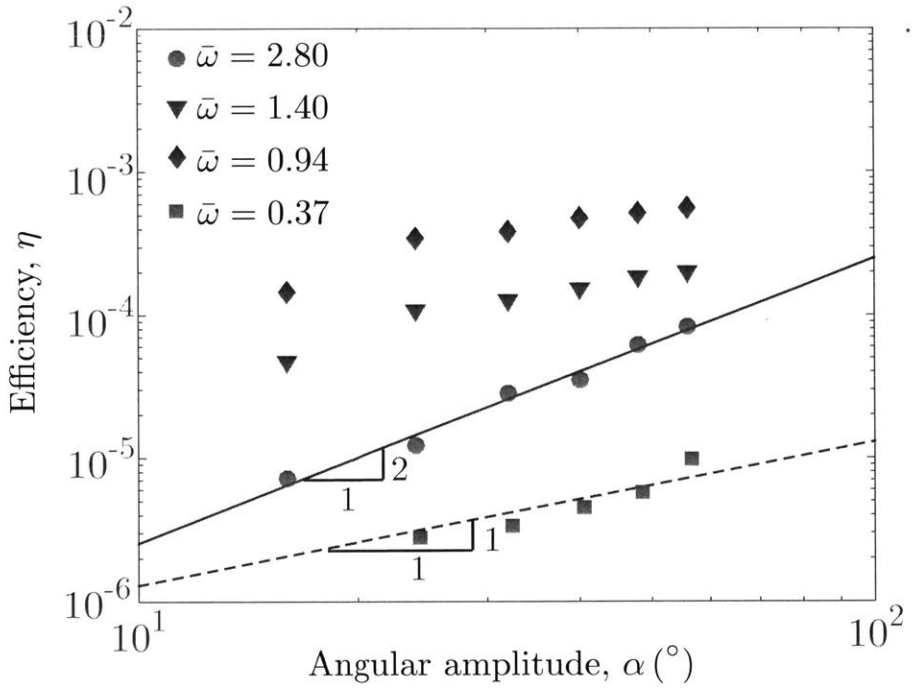

Figure 3-10: Efficiency η of semi-circular plates ($L = 200\,\text{mm}$) versus angular amplitude, α.

plate ($h = 102\mu\text{m}$, green squares), we find that $\eta \sim \alpha$. whereas for the thickest plate ($h = 762\mu\text{m}$, circles), the data is consistent with a power-law, $\eta \sim \alpha^2$. For the intermediate plate, we find $\eta \sim \alpha^q$ where $1 \leq q \leq 2$. We will rationalize the angular amplitude scaling in Section 3.5.1.

3.5 Euler-Bernoulli Equation

In this section, we will derive scaling expressions of the moment terms acting on the plates in terms of the geometry and properties of the plates and flapping conditions. We will consider the inertial, bending and aerodynamic moments. First, we assume a Euler-Bernoulli description [49, 29] for the deflection ξ,

$$(m_p + m_*)\ddot{\xi} + B\xi'''' + \frac{1}{2}\rho_f C_d \left|\dot{\xi}\right| \dot{\xi} = 0, \tag{3.14}$$

where $m_p = \rho_p h$ is the mass per unit area of the plate, $m_* \sim \rho_f \alpha R$ is the added mass of the fluid per unit area (estimated from the acceleration of the mass of air displaced by the moving plate [18]), $B = \frac{Eh^3}{12(1-\nu^2)}$ is the flexural rigidity per unit length of a plate, C_p is the aerodynamic force coefficient, $\dot{\xi} = \partial\xi/\partial t$ and $\xi' = \partial\xi/\partial x$ (x is the spacial coordinate).

Recall from Section 1.3 that the mode shape of a vibrating plate for a plate with fixed-free boundary condition is

$$\xi = w_0 L\alpha \sin(\omega t) \sin(\frac{n\pi}{R}x) - w_1 x, \tag{3.15}$$

where w_0 and w_1 are scaling parameters for the magnitude of maximum deflection, then differentiating Eq. (3.15) with respect to time, we have

$$\dot{\xi} = w_0 L\alpha\omega \cos(\omega t) \sin(\frac{n\pi}{R}x) \tag{3.16}$$

$$\ddot{\xi} = -w_0 L\alpha\omega^2 \sin(\omega t) \sin(\frac{n\pi}{R}x) \tag{3.17}$$

and integrating Eq. (3.15) with respect to x, we have

$$\xi'''' = w_0 L(\frac{n\pi}{R})^4 \alpha \sin(\omega t) \sin(\frac{n\pi}{R}x) \tag{3.18}$$

We can then substitute Eq. (3.16), (3.17) and (3.18) into the individual terms of Eq. (3.14). Integrating the individual terms in Eq. (3.14) with respect to the surface area of the fan and the distance from the rotation axes would give us the expression for each of the contributing moments. The first term is the inertial moment and there are two contributing terms, the inertial moment due to the plate and the added mass. The second term is the bending moment and the last term represents the moment due to aerodynamic forces. We will now discuss the individual moment terms in details.

Inertial Moment

The first term in Eq. (3.14) represents the d'Alembert forces due to the acceleration of the plate. The associated moments correspond to the sum of the inertial moments due to the mass of the plate and its added mass: $M^{\mathrm{i}} = M_p^{\mathrm{i}} + M_*^{\mathrm{i}}$. Inertial moment due to the mass of the plate, is given by integrating the product of the d'Alembert force at each infinitesimal segment and the moment arm.

The d'Alembert force per unit area F_p of the plate due to its mass is given by

$$dF_{\mathrm{p}} = \rho_p h \ddot{\xi}, \tag{3.19}$$

while moment arm of the force is given by

$$dM_{\mathrm{p}}^{\mathrm{i}} = \rho_p h x \ddot{\xi}. \tag{3.20}$$

Thus the resultant moment can be found by integrating Eq. (3.20) over the semi-circular area of the plate A

$$M_{\mathrm{p}}^{\mathrm{i}} = \int_A \rho_p h x \ddot{\xi}\, dA. \tag{3.21}$$

Using the scaling, considering only the amplitude of the modes, $\ddot{\xi} \sim w_0 L \alpha \omega^2$, based on Eq. (3.17) and dropping the sinusoidal terms, and using $\int_A x dA \sim R^2 L$ we have

$$M_{\mathrm{p}}^{\mathrm{i}} \sim \int_A w_0 \rho_p h x L \alpha \omega^2\, dA \sim w_0 \rho_p h R^2 L^2 \alpha \omega^2. \tag{3.22}$$

Next, the forces due to added mass is due to the acceleration of the mass of air displaced by the plate. The volume of displaced air is given by the volume of the segment swept by the plate, which is $\mathcal{V} \sim \alpha R^3$. Thus the force dF_* and moment arm dM_*^{i} of the contribution of an infinitesimal volume of air is

$$dF_* = \rho_f \ddot{\xi} d\mathcal{V}, \tag{3.23}$$

$$dM_*^{\mathrm{i}} = \rho_f x \ddot{\xi} d\mathcal{V}. \tag{3.24}$$

The inertial moment due to the added mass is then given by integrating Eq. (3.24) and using the scaling $\ddot{\xi} \sim w_0 L\alpha\omega^2$ and using $\int_A xdA \sim R^2 L$, we have

$$M_*^{\mathrm{i}} = \int_{\mathcal{V}} \rho_f x\ddot{\xi}\, d\mathcal{V} \sim \int_{\mathcal{V}} w_0\rho_f xL\alpha\omega\, d\mathcal{V} \sim w_0\rho_f R^3L^2\alpha^2\omega^2 \tag{3.25}$$

Bending Moment

The second term in Eq. (3.14) represents the bending moment. The per unit length forces due to bending is given by

$$dF^{\mathrm{b}} = B\xi''''. \tag{3.26}$$

The moment per unit length due to bending is given by

$$dM^{\mathrm{b}} = Bx\xi''''. \tag{3.27}$$

Using the scaling $\xi'''' \sim w_0\frac{L}{R^4}\alpha$, based on Eq. (3.18) and dropping the sinusoidal terms, the overall moment due to bending is found by integrating Eq. (3.27):

$$M^{\mathrm{b}} = \int_A Bx\xi''''dA \sim \int_A w_0 Bx\frac{L}{R^4}\alpha dA \sim w_0 B(L/R)^2\alpha \sim w_0 B\alpha \sim w_0 h^3\alpha. \tag{3.28}$$

Aerodynamic Force

Finally, the third term is due to aerodynamic loading. Taking the dynamic pressure as $\frac{1}{2}\rho_f U^2$, the aerodynamic force per unit area of the semi-circular plate is given by

$$dF^{\mathrm{a}} = \frac{1}{2}\rho_f C_p\dot{\xi}^2 dA, \tag{3.29}$$

and the moment arm of the aerodynamic force about the axis of rotation is

$$dM^{\mathrm{a}} = \frac{1}{2}\rho_f C_p\dot{\xi}^2 xdA, \tag{3.30}$$

Hence the total moment associated with the aerodynamic loading is found by in-

tegrating Eq.3.30 and using the scaling $\dot{\xi} \sim w_0 L\alpha\omega$, based on Eq. (3.16) and dropping the sinusoidal terms:

$$M^{\mathrm{a}} = \int_A \frac{1}{2}\rho_f \dot{\xi}^2 x \, dA \sim w_0^2 \rho_f R^2 L^3 \alpha^2 \omega^2 \tag{3.31}$$

where the aerodynamic force coefficient lies in the range $2.4 \leq C_p \leq 3.5$ for rotational motion [72, 1].

3.5.1 Order of Magnitude of the Moment Terms

The data presented above for the magnitude of the generated flow (Fig. 3-6) and the aerodynamic efficiency (Fig. 3-9), as functions of $\bar{\omega}$ and α, respectively, can now be interpreted by balancing the inertial, elastic and aerodynamic moments, in the limiting cases of (I) thin, (II) thick and (III) intermediate plates. For convenience, we will treat $R \sim L$ and the scaling for the four moments are summarized below:

$$M_{\mathrm{p}}^{\mathrm{i}} \sim w_0 \rho_p h L^4 \alpha\omega^2 \tag{3.32}$$

$$M_{*}^{\mathrm{i}} \sim w_0 \rho_f L^5 \alpha^2 \omega^2 \tag{3.33}$$

$$M^{\mathrm{b}} \sim w_0 E h^3 \alpha. \tag{3.34}$$

$$M^{\mathrm{a}} \sim w_0^2 \rho_f L^5 \alpha^2 \omega^2 \tag{3.35}$$

The resultant torque is then given by,

$$\tau = M_{\mathrm{p}}^{\mathrm{i}} + M_{*}^{\mathrm{i}} + M^{\mathrm{b}} + M^{\mathrm{a}} \tag{3.36}$$

Thin Plate Regime

In the case of our semi-circular fans, we defined it as the region when $\bar{\omega} \leq 0.6$. In this region, the thickness of the plate is much smaller relative to its other dimensions $\frac{L}{h} \gg 1$ or $L \gg h$. Thus, we will neglect terms that scales with h, i.e. elastic and inertia of plate moment terms $\{M^{\mathrm{b}}, M_p^{\mathrm{i}}\}$ and we will keep the terms that does not scale with

h, i.e. aerodynamics and added mass terms $\{M^{\mathrm{a}},\, M_*^{\mathrm{i}}\}$. Physically, this means that aerodynamic and added mass effects dominate, while the elasticity and inertia of the plate are negligible or $\{M^{\mathrm{a}},\, M_*^{\mathrm{i}}\} \gg \{M^{\mathrm{b}},\, M_p^{\mathrm{i}}\}$. Hence, Eq.3.14 becomes:

$$m_*\ddot{\xi} + \frac{1}{2}\rho_f C_d \left|\dot{\xi}\right| \dot{\xi} = 0, \tag{3.37}$$

and the two terms in Eq.3.37 scales similarly with $\{M^{\mathrm{a}},\, M_*^{\mathrm{i}}\}$:

$$w_0 \rho_f L^5 \alpha^2 \omega^2 \sim w_0^2 \rho_f L^5 \alpha^2 \omega^2 \tag{3.38}$$

Thus the amplitude of the mode shape of plate deflection w_0 does not depend explicitly on α. Consequently, $U \sim \alpha$ and $\bar{u}$ is independent of α, which is confirmed by the data in Fig. 3-6. To help understand the dependence of the efficiency on α, we consider the scaling for the resultant torque. From Eq.3.36, the resultant torque is now

$$\tau = M_*^{\mathrm{i}} + M^{\mathrm{a}} \tag{3.39}$$

$$\tau \sim \rho_f L^5 \alpha^2 \omega^2 \tag{3.40}$$

and hence the scaling for the input power is

$$P_{\mathrm{i}} \sim (M^{\mathrm{a}} + M_*^{\mathrm{i}})\alpha\omega \sim \rho_f L^5 \alpha^3 \omega^3 \tag{3.41}$$

The scaling for the input power, given that we know $U \sim \alpha$ for thin plates from Section 3.4.1 is

$$P_{\mathrm{o}} \sim SU^3 \sim \alpha U^3 \sim \alpha^4 \tag{3.42}$$

Thus the dependency of the aerodynamic efficiency on α is given by:

$$\eta = \frac{P_{\mathrm{o}}}{P_{\mathrm{i}}} \sim \frac{\alpha^4}{\alpha^3} = \alpha, \tag{3.43}$$

which is also found experimentally (Fig. 3-9, squares).

Thick Plate Regime

For thick plates, even though h is smaller than L, the value of h is large enough such that $\rho_p h \gg \rho_f L$ and $Eh^3 \gg \rho_f L^5$. Physically this means that aerodynamic and added mass effects can be neglected over inertia and elasticity: $\{M^{\mathrm{a}}, M_*^{\mathrm{i}}\} \ll \{M^{\mathrm{b}}, M_p^{\mathrm{i}}\}$. Now the resultant torque is

$$\tau = M_{\mathrm{p}}^{\mathrm{i}} + M^{\mathrm{b}} \tag{3.44}$$

$$\tau \sim \rho_p h L^4 \alpha \omega^2 + E h^3 \alpha \tag{3.45}$$

and hence the scaling for the input power is

$$P_{\mathrm{i}} \sim (M_{\mathrm{p}}^{\mathrm{i}} + M^{\mathrm{b}})\alpha\omega \sim \rho_p h L^4 \alpha^2 \omega^3 + E h^3 \alpha^2 \omega \tag{3.46}$$

The scaling for the input power, given that we know $U \sim \alpha$ for thick plates from Section 3.4.1 is

$$P_{\mathrm{o}} \sim SU^3 \sim \alpha U^3 \sim \alpha^4 \tag{3.47}$$

Thus the dependency of the aerodynamic efficiency on α is given by:

$$\eta = \frac{P_{\mathrm{o}}}{P_{\mathrm{i}}} \sim \frac{\alpha^4}{\alpha^2} = \alpha^2, \tag{3.48}$$

which is in good agreement with the data (Fig. 3-9, circles).

Intermediate Plate Regime

Finally, for intermediate thickness plates, all four moment terms are of the same order; the governing equation is nonlinear, making a detailed analysis more challenging. Qualitatively, the third term in Eq. (3.14) depends quadratically on the velocity of the plate and this damping term becomes increasingly more important as α is increased. Consequently, the deflection of the plate tip, and, hence, the average velocity of the generated flow, is expected to decrease with increasing α, which is also confirmed by the data in Fig. 3-6.

The interesting thing is to note how even though the plate is producing propor-

tionally less flow with increasing amplitude, the efficiency still increases with flapping amplitude. It is likely that the input and output powers are polynomials of α based on the scaling of each of the terms. The order of the input and output powers are $P_i \sim O(\alpha^{n_1})$ and $P_o \sim O(\alpha^{n_2})$, the exponents can be related in the inequality, $n_1 \leq n_2$. In the limits of thin and thick plates, the values of n_1 and n_2 are [3,4] and [2,4] respectively. From Fig. 3-6 we observed that $\bar{u} \sim \alpha^{n_3}$, where $n_3 \leq 0$ and so $U \sim V\alpha^{n_3} \sim \alpha^{1+n_3}$. Since U increases monotonically with V in Fig. 3-5, $0 < 1 + n_3 < 1$ and so $n_2 = 4 + 3n_3 \leq 4$ for intermediate plates. From Fig. 3-6a, we find that $U \sim \alpha^{0.5}$ fits well with the intermediate curve, which gives us $n_2 = 2.5$ and $\bar{u} \sim \alpha^{-0.5}$. Consequently, if we assume $w_0 \sim \bar{u} \sim \alpha^{-0.5}$, we find $M^{\mathrm{b}} \sim \alpha^{0.5}$, $M^{\mathrm{a}}, \sim \alpha$ and, M_*^{i} and $M_p^{\mathrm{i}} \sim \alpha^{1.5}$ which gives us $\eta \sim \alpha$. We observe from Fig. 3-9 that the slope of the curve for intermediate plate is around 1.

3.6 Outlook

In this chapter, the effect of thicknesses on the flow generation of semi-circular flat plate were discussed. First, we presented the measurement of the natural frequency of the semi-circular flat plate and fitted the parameter to classical plate vibration theory that relates natural frequency to geometry. Using the experimental set up presented in Chapter 2, we tested a variety of plates of different thicknesses and related their normalized velocity to normalized natural frequencies and demonstrated that the optimal conditions for flow generation and efficiency of a semi-circular homogeneous plate occur when driving near its natural frequency, which is consistent with previous studies of fixed flapping structures [2, 4, 24, 25, 42, 46, 49, 50]. We were also able to measure the input torque required for the flapping motion, which allowed us to define an efficiency term. By observing the order of magnitude of the contribution of different moment terms we were able to determine the scaling of efficiency terms with the flapping amplitude for both thick and thin plates. In the next chapter, we will focus on heterogeneous plates, namely the hand fan, the discrete model fans and corrugated fans to check whether a similar mechanism is present.

Chapter 4

Aeroelastic Behavior of Heterogeneous Plates

In this chapter, we turn our attention to the flow generated by flapping heterogeneous plates. The aim is to find out if the structural design of the plates increases the velocity of the flow and require less input power. The following cases are considered: the hand fans, the discrete model fans, and the corrugated fans. First, we present the results on the natural frequencies of the hand fans and compare them to the characteristic frequencies of a beam. The natural frequencies for both the hand fans and the discrete model fans were found to be in the range of the thick plates regime defined in Section 3.5.1. The normalized velocity for the hand fans and discrete model fans were then plotted against the normalized natural frequency. We found that one of the hand fans and the discrete model fans produced significantly higher velocity compared to the rigid plates. In the case of the corrugated plates, we first measured the flexural stiffness of the corrugated plates and compared them to theory and finite element simulations using commercial finite element package ABAQUS/CAE (SIMULIA, Providence, RI). We then present the normalized velocity generated by the corrugated plates as a function of the normalized natural frequency of the original semi-circular. It was found that reversible buckling is a mechanism for generating higher flow velocity and power efficiency.

4.1 Aeroelastic Behavior of the Hand Fans

In this section, we present the results for the natural frequency and flow measurements of the hand fans described in Section 2.3.1. First, we measured the natural frequency of the hand fan using the laser vibrometer setup described in Section 2.2. Since the structure of a handheld fan is more complicated than a semi-circular flat plate, we start by deriving the first and second mode shape of the fan in Section 4.1.1. To simplify the estimation of the natural frequencies, we fitted the vibration data by defining a characteristic frequency based on a beam. We then compared the normalized velocity and the power efficiency of the flow generated by the hand fan to that of the homogeneous flat plate in Section 4.1.3 and 4.1.4 respectively.

4.1.1 Mode Shape of Hand Fans

In Section 1.3, we derived analytical expressions for the mode shape of a flat plate that has one fixed and three free boundaries. We showed that mode shapes that depend only on the x direction satisfy the symmetric free-free boundary condition in the z direction. For the hand fan, we cannot simply assume that the mode shape varies only in the x direction as the *stick-ribs-leaves* structure of the hand fan is different from a flat plate.

Hence, we created an array of points marked with the reflective tapes on the right half of the face side of Fan 1 (Fig. 4-1a) and measured the acceleration a_n and phase shift ϕ using the process described in Section 2.2. We can then derive the maximum modal deflection $\zeta_{max,n} = a_n/\omega^2$, where a_n is the acceleration of the surface at the n^{th} location. Fig. 4-1b and Fig. 4-2 show the maximum modal deflection, $\zeta_{max,n}$ of the face side surface of Fan 1 at the first and second resonant frequency ($\omega_n \approx \{57.6, 94.2\}$ rad/s, shaker amplitude $A = 0.5$ mm), respectively. The axis follows the same convention as the experimental setup in Fig. 2-1.

We see that the first mode shape of the hand fan is almost constant in the z direction (similar to a planar plate). The second mode of the hand fan displayed a radial mode shape, with regions of alternating signs of phase. Note that the second

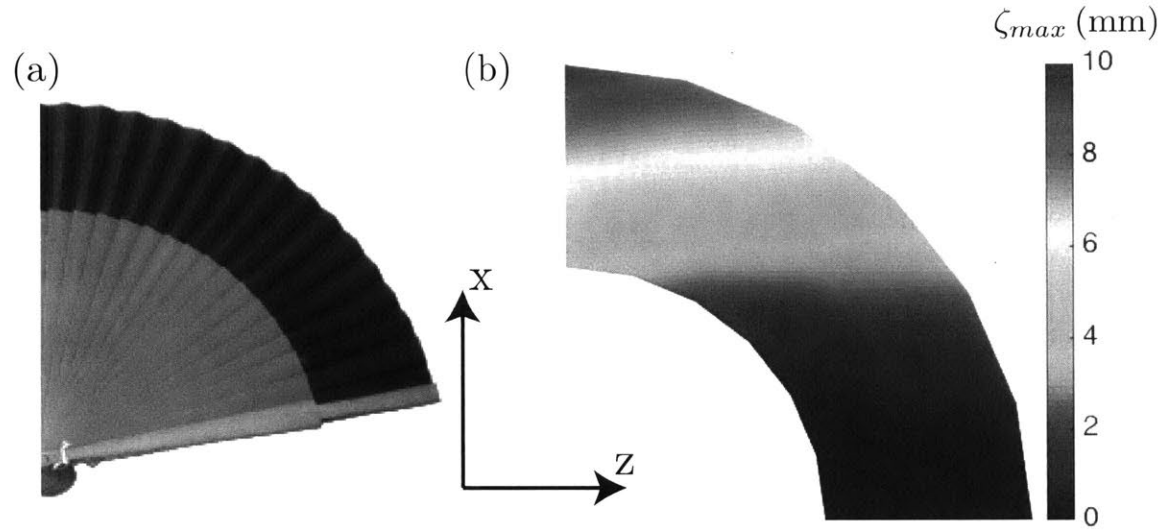

Figure 4-1: (a) A photograph of the side of Fan 1 where we measured the surface acceleration (photo not to scale) (b)Maximum deflection ζ_{max} for one half of Fan 1 at the first resonant frequency, $\omega_{n1} \approx 57.6$ rad/s (9.2 Hz) and shaker amplitude $A = 0.5$ mm (out of plane direction).

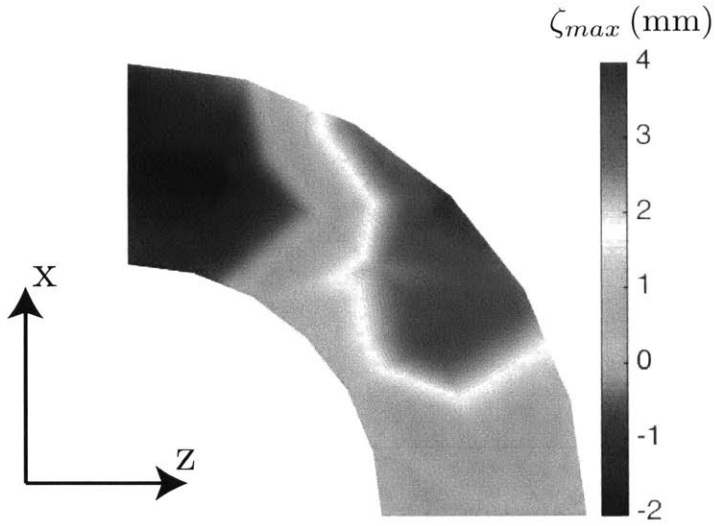

Figure 4-2: Maximum deflection ζ_{max} for one half of the Fan 1 at the second resonant frequency, $\omega_{n2} \approx 94.2$ rad/s (15 Hz) and shaker amplitude $A = 0.5$ mm.

mode shape of a flat plate will again be uniform in the z direction and only varies in the x direction. We conjecture that at higher natural frequencies, we would expect more of the alternating patterns to occur. The radial sticks would be vibrating relative to each other and the hand fans behave just like an array of beams. To test our hypothesis, we compared the measured frequency to the characteristic frequency of beams in Section 4.1.2.

4.1.2 Natural Frequency of Hand Fans

As we mentioned in Section 4.1.1, we conjectured that the sticks on the hand fan vibrate as if they were independent beams and, hence, we rewrite the characteristic frequency of the flat plate Eq. (3.1) to one that is similar to the characteristic

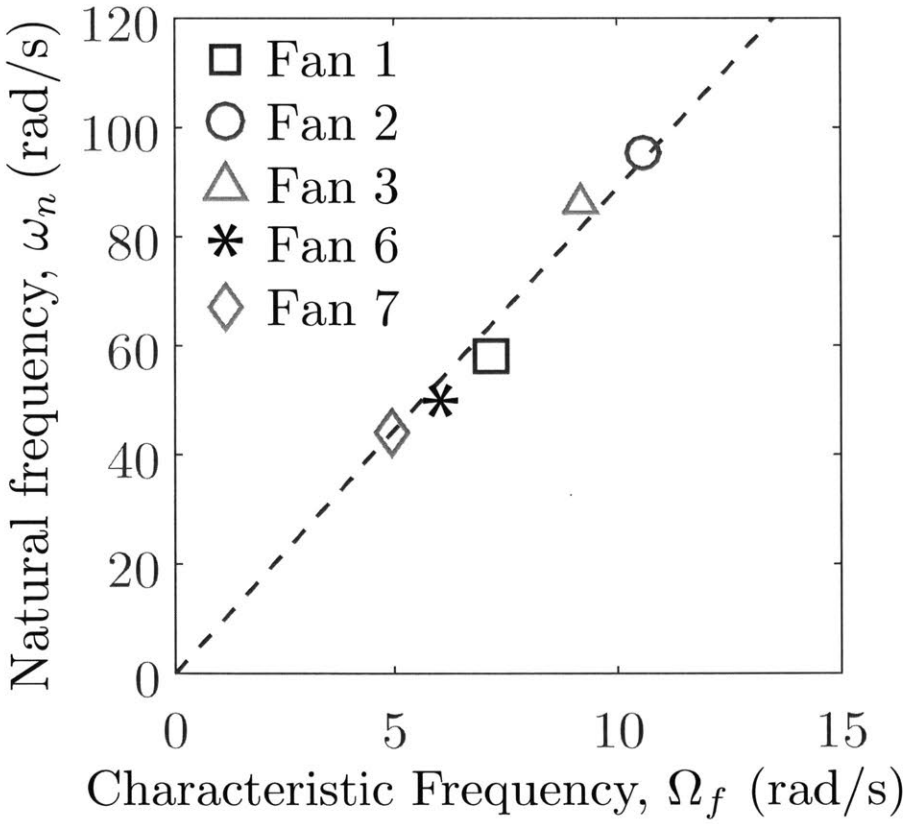

Figure 4-3: Measured natural frequency plotted against the characteristic frequency for Fans 1-3, 6 and 7. The dashed line is a linear fit.

frequency of a beam:

$$\Omega_f = k_f \sqrt{\frac{EI}{mL^4}}, \tag{4.1}$$

where $m = M/R$ is the mass per unit length of the fan, M is the total mass of the fan and EI is the effective flexural stiffness measured using the procedure outlined in Section. 2.4.

In Fig. 4-3, we plot $\omega_n(\Omega_f)$ for Fans 1-3, 6 and 7 (Details of the fans can be found in Section 2.3.1). The natural frequencies of Fans 4 and 5 are above the 22 Hz limitation of the laser vibrometer and were excluded in Fig. 4-3. Similarly to the semi-circular plates, we found that $\omega_n \propto \Omega_f$ with a prefactor $k_f = 8.9 \pm 0.7$. The linear relationship between ω_n and Ω_f indicates that the fans are vibrating like beams and can be seen as a set of discrete elastic strips arranged in a semi-circular fashion. Hereon, we use ω_n as a measure of the flexural properties of both the fans.

4.1.3 Flow Generated by the Hand Fan

We measured the flow generated by the hand fan using the same procedure for the flat plate (at the location $\theta = 0°$ and $d = 0.1R$ as described in Section 3.3). In Fig. 4-4, we plotted U versus the velocity of the tip of the fan $V = \omega\alpha L$ (based on a rigid plate). We found that all three fans have a linear dependence, $U \propto V$, similar to the rigid flat plate. Fan 2 and 3 produced comparable velocity ($U \sim \{0.75, 0.76\}V$) of the generated flow at each driving velocity, while Fan 1 generated consistently higher velocity. Note that Fan 1 is the most flexible ($EI = \{2.24 \pm 0.02, 4.02 \pm 0.04, 2.76 \pm 0.03\} \times 10^{-2}\,\mathrm{Nm}^2$ for Fan 1, 2 and 3) and has the lowest natural frequencies among the three fans ($\omega = \{57.6, 95.5\,88.0\}$ rad/s).

Having measured the natural frequency of the hand fans, we compared the flow they generate to that of the flat plates. Of particular interest is whether the hand fans improve the flow generated by plates with similar natural frequencies. The data were processed in the same manner as the flat plate. In Fig. 4-5, we contrast the $\bar{u}(\bar{\omega})$ data for Fans 1, 2 and 3 (open symbols) to the homogeneous plates (closed gray triangles). Given that the natural frequency of these fans is significantly larger than

the driving frequency, $\bar{\omega} = \{4.6,\ 7.6,\ 7.0\}$, one would expect them to exhibit rigid limit behavior or produce the same normalized velocity as the thick plates. The normalized velocities for Fan 2 and 3 $\bar{u} = \{0.75\pm0.05,\ 0.76\pm0.10\}$ are only $\approx 9\%$ higher than the normalized velocity of a rigid plate $\bar{u} = 0.70\pm0.04$. On the other hand, $\bar{u} = 0.97\pm0.20$ for Fan 1, which is $\approx 39\%$ higher than the expected velocity for a homogeneous plate with the same normalized natural frequencies. These results suggest that the discrete design may be an important feature that increases the velocity of the generated flow. In order to verify that hypothesis, we conducted the experiments on the discrete model fans with the methods described in Section 2.3.3 using the same methods as the hand fans. Besides the generated velocity, we also want to find out if the hand fans are more efficient than the flat plates as a flow generating tool and the results are presented in Section 4.1.4.

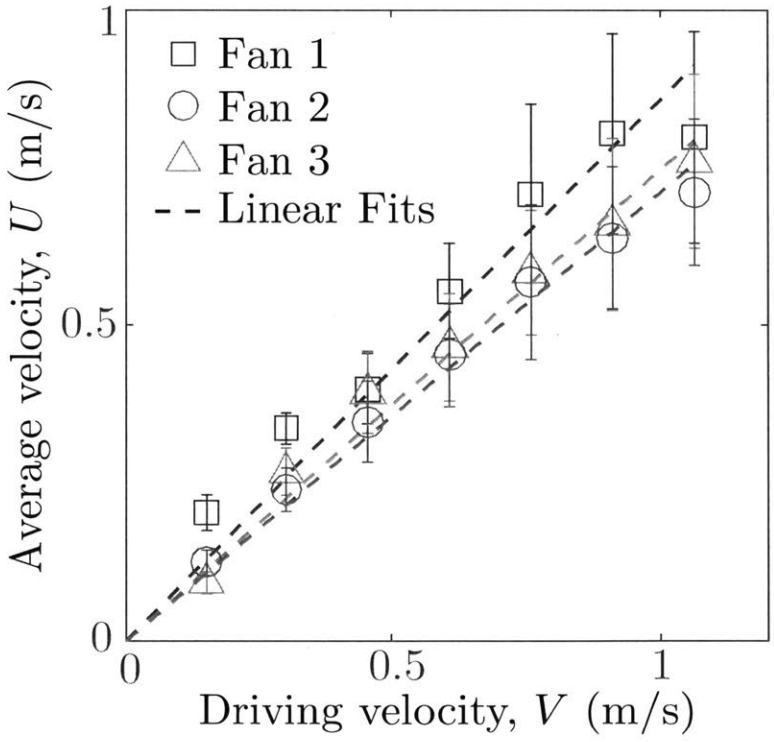

Figure 4-4: Velocity of generated flow U by the fan versus the velocity of the fan tip V for the three hand fans.

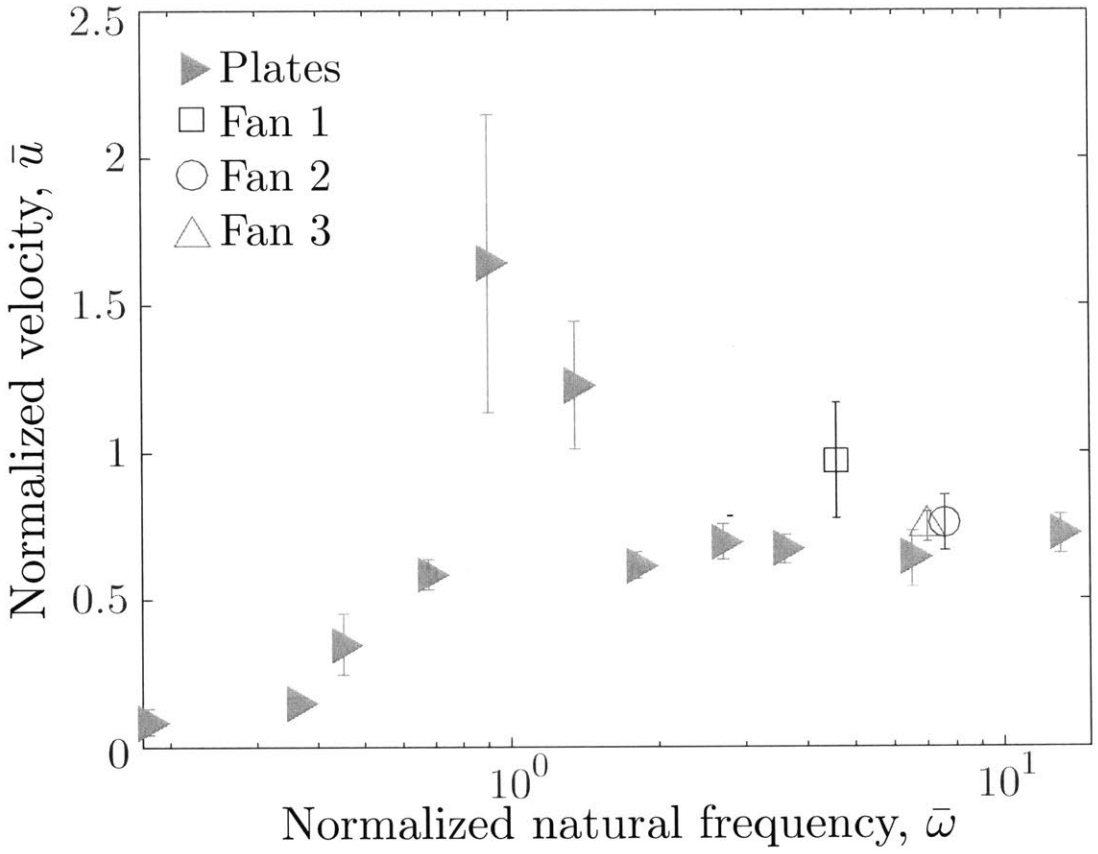

Figure 4-5: Average normalized velocity generated by the hand fans (open symbols) and the semi-circular plates (grey triangles) versus the corresponding normalized natural frequencies for $8° \leq \alpha \leq 56°$ at $8°$ intervals. The error bar represents the standard deviation of the flow generated for $8° \leq \alpha \leq 56°$.

4.1.4 Power Efficiency of the Flapping Hand Fan

Other than the flow generated by the hand fan, we also compared the power efficiency of the hand fans to that of the flat plates. We measured the torque required to flap the hand fan in a similar way to the procedure used on the flat plate described in Section 2.1.3. Details of the definition and derivation of the input and output power terms were presented in Section 3.4.2 and for convenience, we summarize the expressions for efficiency, input and output powers here. We defined the power efficiency as

$$\eta = \frac{P_o}{P_i}, \tag{4.2}$$

the input power

$$P_{\mathrm{i}} = \bar{\tau}\dot{\Theta}, \tag{4.3}$$

and the output power

$$P_{\mathrm{o}} \approx 1/2\rho_f S U^3. \tag{4.4}$$

In Fig. 4-6, we contrast the efficiency η data for Fans 1, 2 and 3 (open symbols) to the homogeneous plates (closed symbols). The efficiency of Fans 1, 2 and 3 are $\eta(\text{fans})/\eta(\text{plates}) = \{7.4, 4.5, 5.8\}$ times the efficiency of the flat plates. Fans 2 and 3 produced $\approx$ 13% higher velocity and consequently $\approx$ 30% more output power as compared to rigid plates of the same normalized natural frequencies (see Fig. 4-5). While the increased output power contributes to a corresponding increase

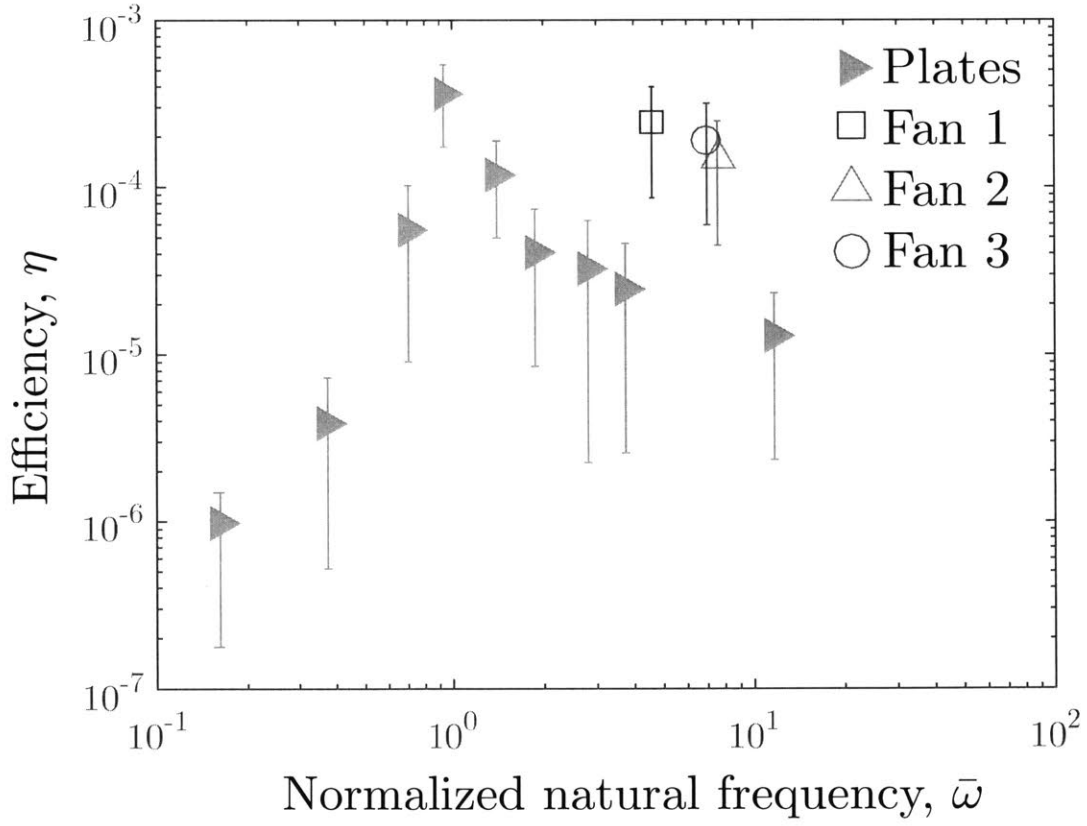

Figure 4-6: Average efficiency for the hand fans (open symbols) and the semi-circular plates (grey triangles) versus the corresponding normalized natural frequencies for $8° \leq \alpha \leq 56°$ at 8° intervals. The error bar represents the standard deviation of the efficiency for $8° \leq \alpha \leq 56°$.

in efficiency, the handheld fans also required much lower input power. Indeed, the input and output powers of Fans 1, 2 and 3, and the flat plates at $\alpha = 32°$ are $P_\text{i} = \{0.0050, 0.0027, 0.0030, 0.0017\}$ W and $P_\text{i} = \{19.73, 18.63, 16.69, \sim 75\}$ W, respectively. In Section 3.5.1 we noted that the dominant moments in the thick plate regime are inertial and bending. A plate of the same normalized natural frequency as the hand fans would have a thickness of $h \approx 900\,\mu$m and a mass of $M = \frac{1}{2}\pi R^2 h \rho_p \approx 0.078$ kg. This is approximately double the masses of Fan 2 and 3 ($M = \{0.0412, 0.0382\}$ kg). Given that the normalized natural frequency is the same, the inertial to bending moment ratio is also the same, meaning that the bending moment of the flat plate is also nearly double that of the fans. Considering the scaling of the moments in Eq. 3.32, we would expect the input power of the handheld fan to be $\approx 50\%$ of the semi-circular flat plate (assuming the distribution of the mass is the same as a semi-circular plate). However, the measured input power of the handheld fans are only $\approx 22 - 26\%$ of that of the flat plates, half of what we were expecting. We hypothesize that the discrete designs of the hand fan, in addition to increasing the output velocity, also contributes to higher power efficiency by reducing the input power requirement.

To investigate the effect of structures with discrete parts connected by compliant materials, we performed the same experiments and analysis on the discrete model fans described in Section 2.3.3 and the results are presented in Section 4.2. We will also revisit the handheld fan by considering its instantaneous deformation in Section 4.3

4.2 Aeroelastic Behavior of the Discrete Models

In this section, we test our hypothesis that the discrete design of the hand fan contributes to the increase in velocity of the flow. We performed the experiments on the discrete model fans described in Section 2.3.3, using the same procedure as both the flat semi-circular plates and the hand fans. In Section 4.2.1, we present the results of the measurement of the natural frequencies and the velocity of the flow and compare them with semi-circular plates of the same natural frequencies. In Section 4.2.2, we make the comparison of power efficiency of the discrete model fans and the semi-circular planar plates.

4.2.1 Natural Frequency and Flow Generated by the Discrete Models

We speculated that discrete structures increase the flow generation and tested the discrete model fans described in Section 2.3.3 using the same procedure for the hand fans and flat plates. The natural frequency of these model fans were similar to that of the homogeneous plate: $\bar{\omega}_n = 33.3\,\text{rad/s}$ and 34.5 rad/s for Model 1 and Model 2, respectively, versus 32.7 rad/s for the flat plate with $R = 200$ mm and $h = 762\,\mu$m (the same thickness of the material used to fabricate the sectors of Model 1 and 2). For simplicity, we shall henceforth call this semi-circular plate *Model Plate* in Section 4.2.1 and 4.2.2. It is surprising that having discrete sections did not significantly alter the natural frequency of the Model Plate (shifts of 1.8 and 5.5% in natural frequency for Model 1 and Model 2 respectively). More material was used for the model fans compared to the Model Plate due to the overlap of sectors, which cause an increase in the fan mass. The bending moment increased correspondingly as the inertial to bending moment ratios of Model 1 and 2 and Model Plate are similar.

In Fig. 4-7, we contrast the average velocity of flow generated by the model fans to that of the flat plates across the range of angular amplitudes $8° \leq \alpha \leq 56°$. We find that the averages of generated flow of $\bar{u} = 1.15 \pm 0.22$ and $\bar{u} = 0.96 \pm 0.13$ (Fig. 4-7, red triangle, green diamond) are significantly higher (53% and 26%,

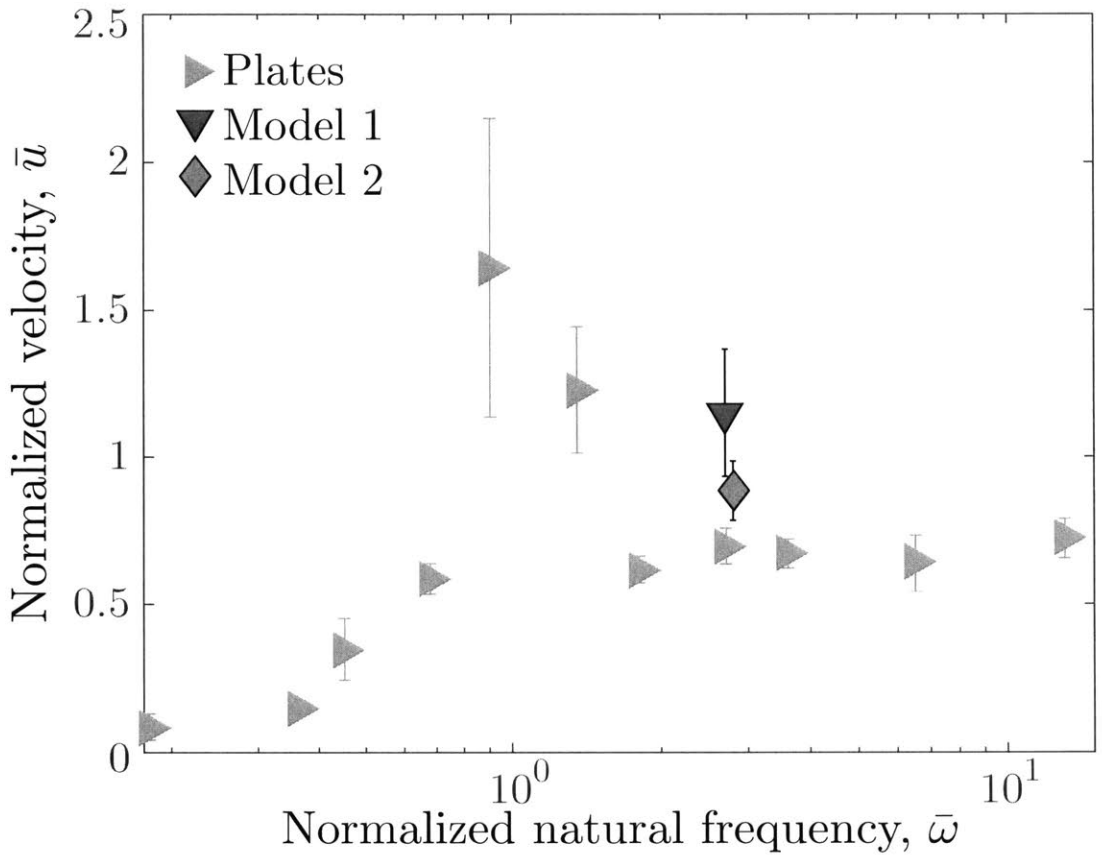

Figure 4-7: Average normalized velocity generated by Model 1 (red triangle), Model 2 (green diamond) and semi-circular plates (grey triangle) versus their corresponding normalized natural frequencies for $8° \leq \alpha \leq 56°$ at $8°$ intervals. The error bar represents the standard deviation of the flow generated for $8° \leq \alpha \leq 56°$.

respectively) than that of the Model Plate. To help us rationalize this improvement in flow generation, we shall measure the instantaneous plate deformation in Section 4.3. We also understood from Section 4.1.4 that even though the natural frequency of the Model 1, 2 and the Model Plate may be the same, the net moment will be affected by the mass and flexural stiffness of the structure and we will discuss the power efficiency of our discrete model fans next.

4.2.2 Power Efficiency of the Flapping Discrete Models

To complete our analysis, in Fig. 4-8, we contrast the efficiency of Model 1 and 2 to that of the Mode Plate. Model 1 and Model 2 have average efficiencies of $\eta = \{1.34, 0.81\} \times 10^{-4}$ which are 3.80 and 2.27 times the average efficiency of the Model Plate ($\eta = 0.36 \times 10^{-4}$). To understand the contributing factors for this increment, we compared both their input and output powers to that of the Model Plate at the median flapping amplitude, $\alpha = 32°$. The output power and input power of Model 1, Model 2 and Plate at $\alpha = 32°$ are $P_o = \{0.0055, 0.0026, 0.0017\}$ W and $P_i = \{51.7, 43.8, 54.6\}$ W respectively. Similar trends were also observed at other angular amplitudes. As expected, the higher input powers for the discrete plates are due to the higher normalized velocity relative to the Model Plate ($\bar{u} =$

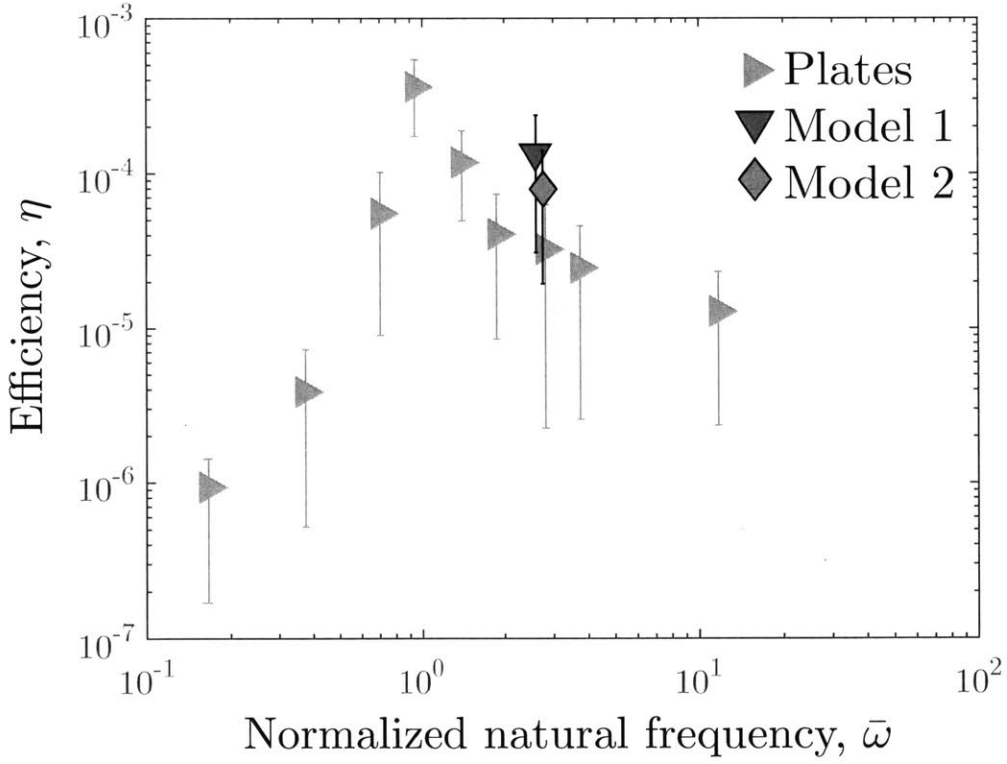

Figure 4-8: Average efficiency of Model 1 (red triangle), Model 2 (green diamond) and semi-circular plates (grey triangle) versus their corresponding normalized natural frequencies for $8° \leq \alpha \leq 56°$ at $8°$ intervals. The error bar represents the standard deviation of the efficiency for $8° \leq \alpha \leq 56°$.

{1.02, 0.80, 0.73} for Model 1, Model 2 and Model Plate at $\alpha = 32°$). The slight decrease in input power is a surprising result because the model fans are heavier (due to the overlapping nature of the discrete model plates) than the Model Plate. At the same values of the natural frequency, the inertial to bending moment ratios are the same and thus the model discrete fans have larger inertial and bending moment. Yet, the input power required to flap the discrete model fans is lower compared to that of Model Plate. We also observed from the handheld fans experiments that the input power is lower than expected (based on masses and flexural stiffness).

The direct effect of discrete sections on input moments is still unclear and we may have to rely on simulations to understand the contributions of the moments better. It is also interesting to note that Model 1 increased the flow generated drastically, while Model 2 increased the efficiency through requiring even less input power as compared to Model 1. Through optimization process, we should be able to design the shape of the sectors that can both produce higher velocity and reduce the input power.

4.3 Comparison of Instantaneous Deflection of Flat Plates, Hand Fans and Discrete Models

Finally, in order to understand why the discrete geometry helps the fan generate higher velocity flow, we quantified the deformation of the discrete model, the homogeneous plates, and a handheld fan. To obtain these data, we used the trigger strobe photography technique described in Section 2.1.4. The out-of-plane deflections, δ were also computed using the image processing technique described in Section 2.1.4. In order to derive the Gaussian curvature K, we used an open source Matlab function *Surface curvature* [11] which calculates the principal curvatures and the Gaussian curvature given the $x - y - z$ positions of points on the surface of the fans.

Fan 1 (Fig. 4-9b2) and the discrete model (Fig. 4-9c2) exhibited non-uniform deflection fields in the x and z directions, while the deflection of the semi-circular plates varied only along x. Moreover, the maximum tip deflection of both the fan

and the discrete model ($\delta_{\text{tip}} = \{31.8, 43.5\}$ mm) was $\approx 5-6$ times larger than that for the plate ($\delta_{\text{tip}} = 7.1$ mm). The Gaussian curvature of the homogeneous plate is uniformly zero (Fig. 4-9a3), a confirmation that the plate is only undergoing pure bending deformation and remains developable (isometric to a plane), as expected [5].

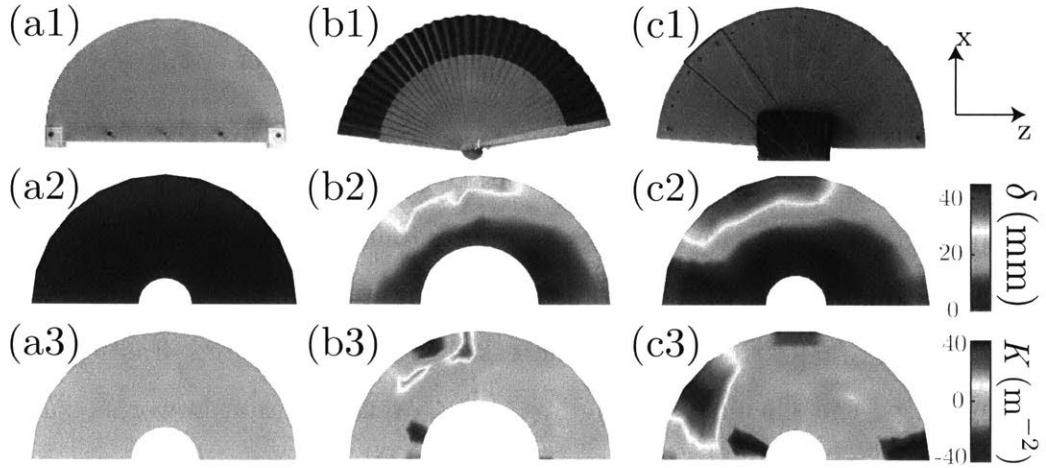

Figure 4-9: Deflection, δ and Gaussian curvature K field at $\omega = 2$ Hz and $\alpha = 48°$ of (a) semicircular plate ($L = 200$ mm, $h = 762\,\mu$m) (b) Fan 1 and (c) Discrete model made with 11 sector-shaped discrete strips (PETG, thickness 762 μm, radius 200 mm, and angular width 18°, with an overlap of $1-5°$ between adjacent strips).

By contrast, both the discrete model (Fig. 4-9c3) and the fan (Fig. 4-9b3) exhibit regions of positive and negative K, which means there are regions of significant of in-plane compression and expansion of the structure. Even if each individual strip only undergoes pure bending about the tangential direction, the additional degrees of freedom provided by their overlap allows this overall in-plane kinematics. The individual strips can form different angles about the radial direction relative to the adjacent strips, generating a "curvature" about the radial direction as illustrated in Fig. 4-10. Together with bending about the tangential direction, we have non-zero Gaussian curvature on the discrete surface. We speculate that this results in larger tip deflections and, correspondingly, increases the strength of vortices shed by the fan tip. Studying the aerodynamic effects of these shape transformations during the flapping motion would require either flow visualization or full-scale computational fluid dynamics (CFD) simulations which are outside of the scope of this thesis.

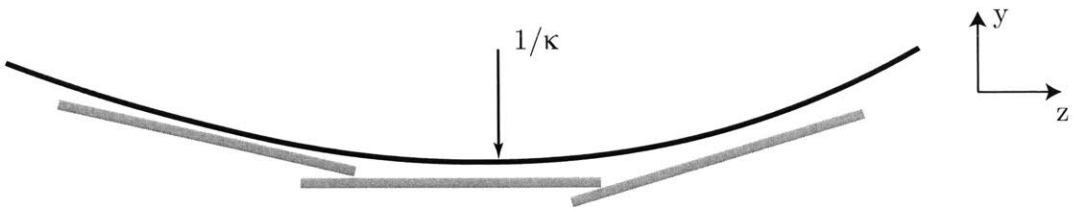

Figure 4-10: A simplified illustration to show how overlapping sectors generate a curvature with adjacent sectors. The amount of deformation is exaggerated and shown here is a generic orthogonal coordinate.

4.4 Outlook on Discrete Section Designs

Based on the results of the experiments on the commercial hand fans and how they compared to the semi-circular plates of similar natural frequencies, we conclude that the efficiency of flow generation was significantly improved by lowering both the mass and the bending stiffness. As the effect of the discrete nature of the hand fans is not well understood, we designed two fans with discrete sectors. In our experiments, Model 1 and 2 differs by the sector shape and even though they both improved the performance of the hand fan (both flow generation and efficiency), Model 1 generated much higher flow velocity than Model 2 while Model 2 required less input power for the flapping motion. Thus the shape of the sectors and the number of sectors used for the fans could be optimized to find the optimal discrete geometry. The optimization process is not a trivial process as we are not only concerned about the mass and flexural stiffness of the resultant structure but also the instantaneous deformation of the fan and the effect on the flow generation. On top of the optimization of the sector shape, the behavior of the discrete sector plates should also be studied for cases near the natural frequency.

In the next section, we explore another structural feature inspired by the pleated hand fan – the effect of the corrugation of the plates. For the discrete sections, we modified the structure of the thick plates and for the next section, we will be working on the thin plates.

4.5 Aeroelastic Behavior of Corrugated Plates

In this section, we imposed corrugation on plates with thickness $h \leq 191\,\mu$m with the method detailed in Section 2.3.4. Intuitively, we know that corrugation increases the flexural stiffness of the plates (only with respect to one of the axes), without changing the mass of the fan. We have first to characterize the bending stiffness of the corrugated plates in the direction of the corrugation. Finally, we will compare the velocity of the flow generated and the power efficiency of the corrugated plate to the corresponding values of the flat plates.

4.5.1 Mechanical Properties of Corrugated Plates

Firstly, we are interested in finding the bending stiffness of a plate at which the middle plane is defined with the shape $y = Hsin(\frac{2\pi z}{\lambda})$, where H is amplitude and λ is the wavelength. An illustration of the shape of corrugation is shown in Fig. 4-11.

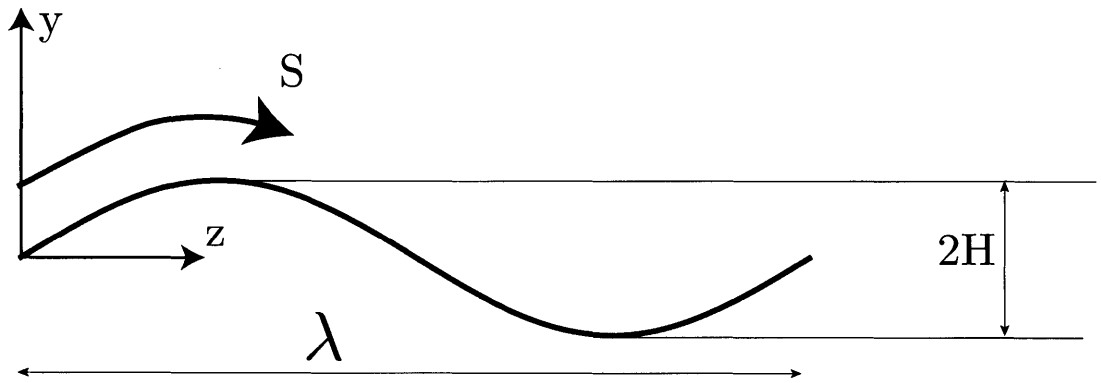

Figure 4-11: Illustration of the shape of corrugation.

Classical experiments conducted by Seydel [59, 66] approximated the length of the unwrapped plate, S and the bending moment I to be

$$\begin{aligned} S_{Sey} &= \lambda(1 + \frac{\pi^2 H^2}{\lambda^2}), \\ I_{Sey} &= \frac{H^2 h}{2}(1 - \frac{0.81}{1 + 2.5(\frac{H}{\lambda})^2}), \end{aligned} \tag{4.5}$$

where the subscript represents the method used to define the value. The values of the moment of inertia from the experiments were found to be much lower than the "exact" values calculated through integration [75]:

$$\begin{aligned} S_{int} &= 2\int_0^{\frac{\lambda}{2}} \sqrt{1+(\frac{dy}{dz})^2}\, dz, \\ I_{int} &= \frac{2}{\lambda}\int_0^{\frac{\lambda}{2}} z^2 h\sqrt{1+(\frac{dy}{dz})^2}\, dz. \end{aligned} \tag{4.6}$$

Evaluating Eqn. (4.6) using the software Mathematica (Wolfram) we have

$$\begin{aligned} S_{int} &= \frac{2\lambda}{\pi}\mathcal{F}_2\left[-\frac{1}{\mathcal{C}^2}\right], \\ I_{int} &= \frac{2H^2 h}{3\pi}\sqrt{1+\frac{1}{\mathcal{C}^2}}\left[(1-\mathcal{C}^2)\mathcal{F}_1\left[\frac{1}{1+\mathcal{C}^2}\right]+\mathcal{C}^2\mathcal{F}_2\left[\frac{1}{1+\mathcal{C}^2}\right]\right], \end{aligned} \tag{4.7}$$

where $\mathcal{C} = \frac{\lambda}{2\pi H}$, $\mathcal{F}_1[x]$ and $\mathcal{F}_2[x]$ are the complete elliptical integral of the first and second kind. The integrals cannot be expressed as analytical functions but for our application, we can use Matlab to evaluate specific values. We can first normalize the moment of inertia per unit length of the corrugated plates by the moment of inertia per unit length of the flat plate, which is given by $I_0 = \frac{h^3}{12}$. Thus we have the following relationships:

$$\begin{aligned} \frac{I_{int}}{I_0} &= \frac{8H^2}{h^2\pi}\sqrt{1+\frac{1}{\mathcal{C}^2}}\left[(1-\mathcal{C}^2)\mathcal{F}_1\left[\frac{1}{1+\mathcal{C}^2}\right]+\mathcal{C}^2\mathcal{F}_2\left[\frac{1}{1+\mathcal{C}^2}\right]\right] \\ &= \frac{2}{\pi^3\mathcal{C}^2}\frac{\lambda^2}{h^2}\sqrt{1+\frac{1}{\mathcal{C}^2}}\left[(1-\mathcal{C}^2)\mathcal{F}_1\left[\frac{1}{1+\mathcal{C}^2}\right]+\mathcal{C}^2\mathcal{F}_2\left[\frac{1}{1+\mathcal{C}^2}\right]\right] \end{aligned} \tag{4.8}$$

$$\frac{I_{Sey}}{I_0} = \frac{6H^2}{h^2}\left(1-\frac{0.81}{1+2.5(\frac{H}{\lambda})^2}\right) \tag{4.9}$$

Note that when we set $H = 0$ or $\lambda = \infty$, I_{Sey} and I_{int} vanish, which is inconsistent with our knowledge that the moment of inertia of the flat plate is given by $I_p = h^3/12(1-\nu^2)$. For corrugated plates, the effective curvature of the plates affects whether the loads are carried transversely (through bending moments) or axially

(through membrane forces) [48]. Castigliano's second theorem was used to derive the effective flexural stiffnesses proposed by Briassoulis [8] and the effective moment of inertia, I_B was given as:

$$I_B = \frac{Eh^3}{12(1-\nu^2)} + \frac{EH^2h}{2}. \tag{4.10}$$

Note that now when $H = 0$, I_B of Eqn. 4.10 was exactly that of the flat plate. Normalizing Eqn. 4.10 by $I_0 = \frac{h^3}{12}$, we have:

$$\frac{I_B}{I_0} = \frac{1}{(1-\nu^2)} + \frac{6H^2}{h^2} \tag{4.11}$$

In order to verify the expressions, we conducted finite element simulations using commercial finite element package ABAQUS/CAE (SIMULIA, Providence, RI) to find the moment of inertia of the corrugated plates I_{sim} for plates of thicknesses $254 \leq h \leq 7000\,\mu$m, in the ranges of $0.5 \leq H \leq 5$ mm and $0.1 \leq \lambda \leq 10$ mm. An example of the ABAQUS model is shown in Fig. 4-12. The plate was fixed on one of the corrugated ends and a line load was imposed on the other end. Symmetry conditions (about the x-axis) were placed on the other two sides, such that it was as though the simulation was conducted with infinite plates.

For plates of $h \leq 1000\,\mu$m, we used the four-node thin shell elements (element type S4R) with 5 integration points through the thickness. We conducted a mesh sensitivity study on large amplitude H and small wavelength λ cases and found that the size of the elements have to be no larger than $\approx \lambda/100$. The number of elements were usually of the order of ~ 4000.

For $h \geq 1000\,\mu$m, we used the eight-node solid elements (element type C3D8R) because there are significant stress gradient across the thickness of the plate (shell elements are good for plane stress conditions). From the mesh sensitivity study, we found that the mesh size has to be at most $h/8$ in the direction of the thickness and $\approx \lambda/100$ for the other dimensions.

In Fig. 4-13, we then plot $I_{sim}/I_0 - 1/(1-\nu^2)$ against H^2/h^2 in log-log graph shown (blue circles). Based on the theoretical value, we should have a line that has a slope of 1 and intercepts the point $[H^2/h^2, I_/I_0 - 1/(1-\nu^2)] = [1, 6]$. From the

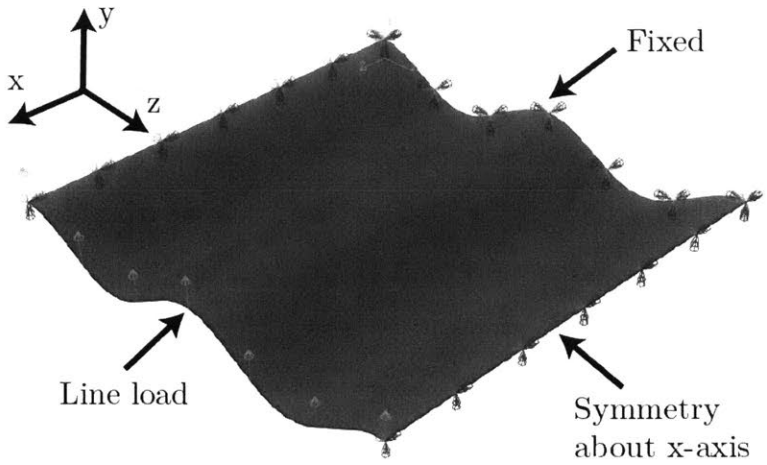

Figure 4-12: Image showing an example corrugated plate in ABAQUS. The boundary conditions are defined as shown.

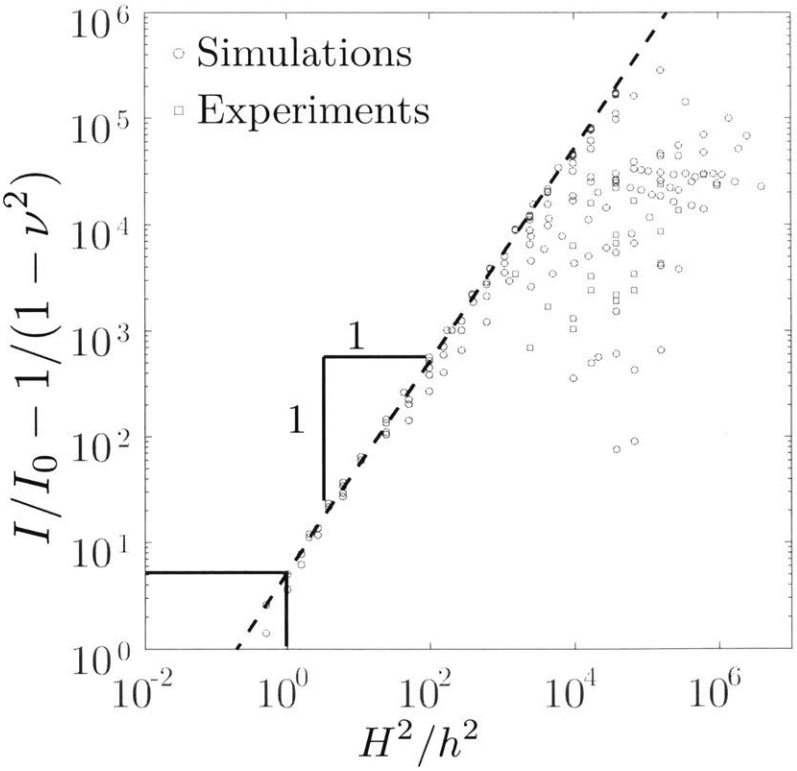

Figure 4-13: Plot of $I/I_0 - 1/(1-\nu^2)$ and H^2/h^2 for simulations, $I = I_{sim}$ (blue circle) and experiment $I = I_{exp}$ (red square). For points below $H^2/h^2 \leq 1000$, the line of best fit was found to have slope 1 and intercepted $H^2/h^2 = 1$ at 5.

results in Fig. 4-13, we see that for $H^2/h^2 \leq 1000$, the line of best fit has a slope of 1 but intercepts the point $[H^2/h^2, I_/I_0 - 1/(1-\nu^2)] = [1, 5]$. For $H^2/h^2 \geq 1000$, some of the simulations show that the moment of inertia falls below the expected linear relationship behavior and exhibited global buckling behavior were observed for plates of $H^2/h^2 \geq 1000$. The buckling behavior is not well characterized by H^2/h^2 since the value of $I_/I_0 - 1/(1-\nu^2)$ spans more than 3 orders of magnitude.

We then experimentally measured the flexural stiffnesses of a few corrugated plates and they are also plotted in Fig. 4-13 (red squares). In order to impose a line load to find the overall flexural stiffness, an additional plate that matches the shape of the corrugation was laser cut from acrylic and attached to the indenter as shown in Fig. 4-14. It was difficult to bend a thicker plate into the corrugated shape without causing irreversible damage, so the smallest feasible H^2/h^2 was in the order of ~ 600. Furthermore, we were also only able to define the shape at one end and as we move away from the clamp, there is a relaxation of the shape of corrugation as the amplitude of corrugation gets smaller, given that the stress-free configuration of the plate is its flat state. The evolution of the corrugation patterns from root to tip can be estimated through energy scaling arguments [69] but that would also be beyond the scope of this thesis.

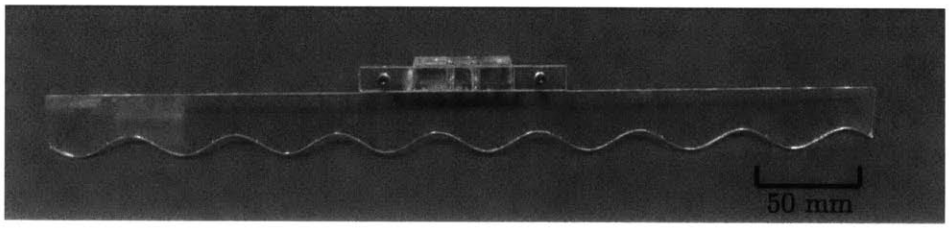

Figure 4-14: Photograph of an example of a linear indenter used to impose a line load on the corrugated fan.

We shall see in Section 4.5.2 how global buckling behavior affects the flow generation of a corrugated plate. Nevertheless, both the simulations and experiments show that at the physically feasible range of $H^2/h^2 \geq 600$ corrugation increases the flexural stiffness by at least ~ 100 times. This means that we expect the natural frequency of the corrugated structures to be at least ~ 10 times larger than the natural frequency

of the plates. Unfortunately, that would also make most of the corrugated structures out of range for the laser vibrometer experiments. Since we do not have specific information of the natural frequency of the corrugated plates, we will be normalizing and compare them with the parameters of the original un-corrugated plate.

4.5.2 Flow Generation of Flapping Corrugated Fans

In a process similar to the commercial handheld fan and the discrete model plates, we again compared the $\bar{u}(\bar{\omega})$ data for by two different corrugation designs (four thicknesses each, blue squares and red circles) with that of the original flat homogeneous plates (gray triangles). Corrugated Fan 1 has $H = 12.5$ mm and $\lambda =$

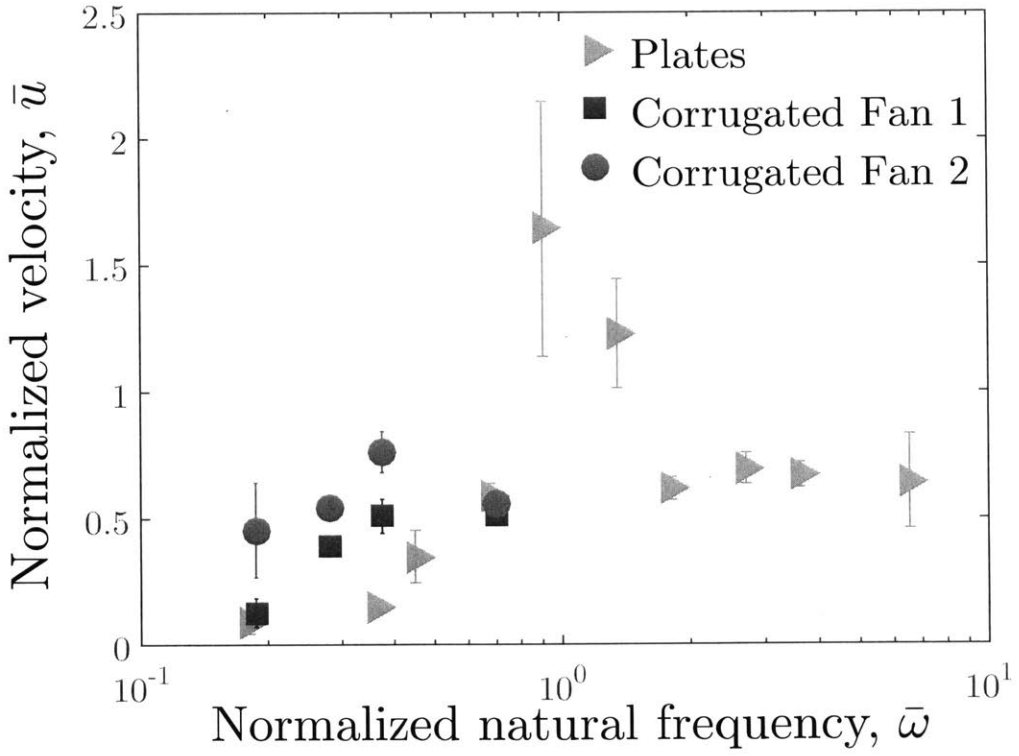

Figure 4-15: Average normalized velocity of flow generated $\bar{u}$ by corrugated design 1 (blue square) $\lambda = 133$ mm, $H = 12.5$ mm and $R = 200$ mm and corrugated design 2 (red circle) $\lambda = 200$ mm, $H = 12.5$ mm and $R = 200$ mm using plates of $h = \{51, 76, 102, 191\}\,\mu$m with original normalized natural frequency $\bar{\omega} = \{0.181, 0.271, 0.361, 0.677\}$ compared to the flat planar plates (grey triangles).

133 mm while Corrugated Fan 2 has $H = 12.5$ mm and $\lambda = 200$ mm. We imposed the corrugation to four homogeneous semi-circular plates of thicknesses $h = \{51, 76, 102, 191\}\,\mu$m and $R = 200$ mm using the clamps of the two corrugated designs (the method of fabrication of the fan clamp is outlined in Section 2.3.4). The normalized natural frequencies of the planar homogeneous semi-circular plates used were $\bar{\omega} = \{0.181, 0.271, 0.361, 0.677\}$ and the average $\bar{u}$ of the corrugated plates are plotted at the $\bar{\omega}$ of the corresponding semi-circular plates in Fig. 4-15.

From Fig. 4-15, we see that the average normalized velocities of flow for both corrugation designs are higher than that of the semi-circular plates of $\bar{\omega} = \{0.271, 0.361\}$. For instance, at $\bar{\omega} = 0.361$, the average velocity is $\bar{u} = \{0.510, 0.764, 0.146\}$ for Corrugated Fan 1, Corrugated Fan 2 and the corresponding semi-circular plates, respectively. For $\bar{\omega} = 0.677$, the average normalized velocities of both corrugated designs are comparable to that of the corresponding semi-circular plates at $\bar{u} \approx 0.515$. Note that at the rigid limit, the average $\bar{u} \approx 0.76$ for the homogeneous semi-circular flat plate and almost all of the corrugated plates performed worse.

Similar to the discrete model fan, the design of the corrugation shape is an important factor to the flow generation. In Fig. 4-16, we present the photographs of the static and undeformed corrugated plates (Fig. 4-16a1, a2, b1 and b2) and photographs of the deformed fan during the flapping motion (Fig. 4-16a3, a4, b3, and b4. The positions of the deformed fans are at the extremes) for Corrugated Fan 1 (Fig. 4-16a) and Corrugated Fan 2 (Fig. 4-16b). The properties of the corresponding semi-circular planar plate are $h = 51\,\mu$m, $R = 200$ mm and $\bar{\omega} = 0.181$. The parameters of the corrugation shapes are $\lambda = 133$ mm and $H = 12.5$ mm for Corrugated Fan 1 and $\lambda = 200$ mm and $H = 12.5$ mm for Corrugated Fan 2. Since both corrugation designs have the same H and h, they have the same theoretical moment of inertia based Eqn. 4.10. However, we see from Fig. 4-16 that Corrugated Fan 1 did not buckle under the load and flaps rigidly with minimal deformation while Corrugated Fan 2 buckles and creates a large tip deformation. This buckling behavior is reversible and Corrugated Fan 2 reverts back to the undeformed configuration once the flapping motion stops. Due to this large buckling behavior, the tip velocity of

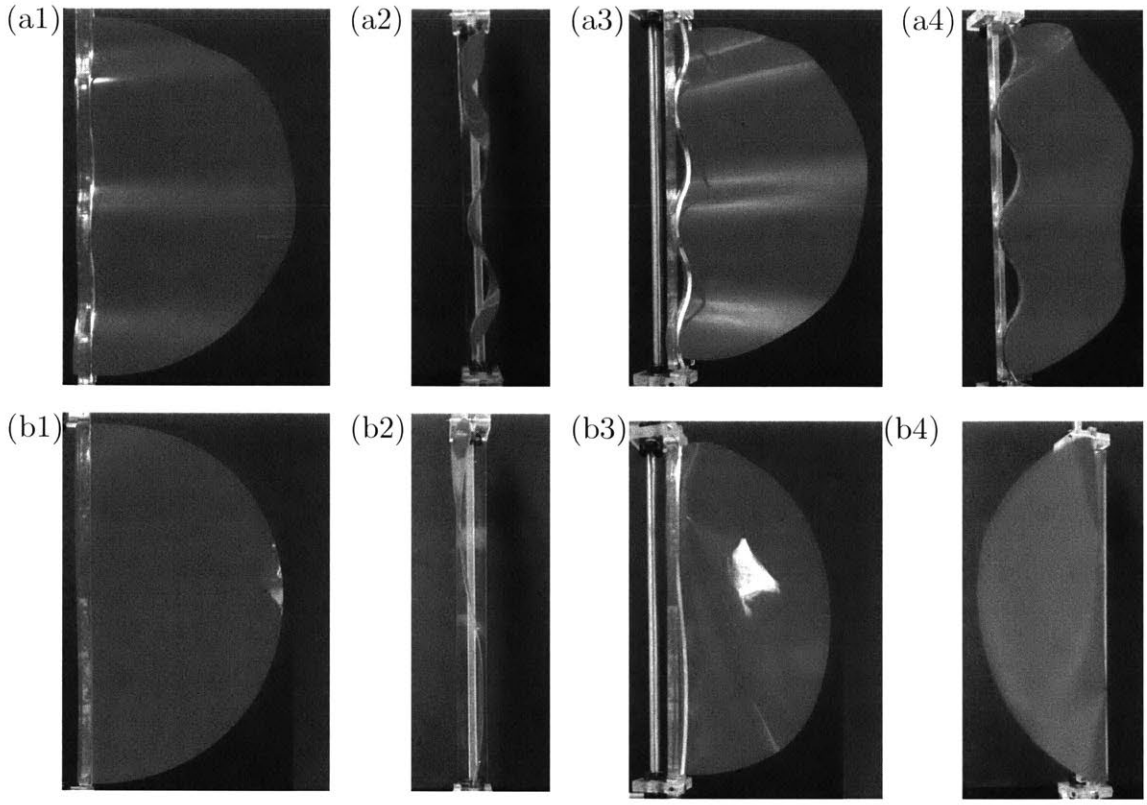

Figure 4-16: Photographs of the undeformed corrugated plate (1) from the face side and (2) from the negative x axis view, and deformed corrugated plate during flapping motion (3) from the face side and (2) from the negative x axis view for (a) Corrugated Fan 1 ($\lambda = 133$ mm, $H = 12.5$ mm) and (b) Corrugated Fan 2 ($\lambda = 200$ mm, $H = 12.5$ mm) with $h = 51\,\mu$m, $R = 200$ mm and $\alpha = 48°$

Corrugated Fan 2 was much larger than $V = \omega\alpha L$ and caused the fan to generate a higher normalized velocity than Corrugated Fan 1. For the conditions shown in Fig. 4-16 ($\bar{\omega} = 0.181$ and $\alpha = 48°$) the normalized velocities for Corrugated Fan 1, Corrugated Fan 2, and plate are $\bar{u} = \{0.143, 0.246, 0.102\}$. Even though Corrugated Fan 1 behaves as though it is rigid at $\alpha = 48°$, the $\bar{u} = 0.143$ is only a fraction of the rigid semi-circular flat plates $\bar{u} \approx 0.70$. We hypothesize that this is because the corrugated shape is not ideal for generating vortexes and to investigate that, CFD simulations of a rigid flapping corrugated plate is required.

Even though the velocity generated by the buckling of the corrugated plate is still smaller and at most comparable to that of rigid plates, the corrugated plates

are thinner ($h = 51\,\mu$m) and hence lighter than the rigid homogeneous semi-circular plates ($h \geq 508\,\mu$m). This means that the inertial moments is lower for the corrugated plates. To understand the overall effect of corrugation on the flapping motion, we consider the power efficiency of the flapping corrugated fan.

4.5.3 Power Efficiency of Flapping Corrugated Fans

To round up our study on corrugated plates, we contrast the average power efficiency η of the corrugated fans to that of the semi-circular plates in Fig. 4-17. The averaged normalized efficiency for both corrugation designs are higher than that for semi-circular plates of $\bar{\omega} = \{0.271, 0.361\}$. At $\bar{\omega} = 0.361$, the average η for Cor-

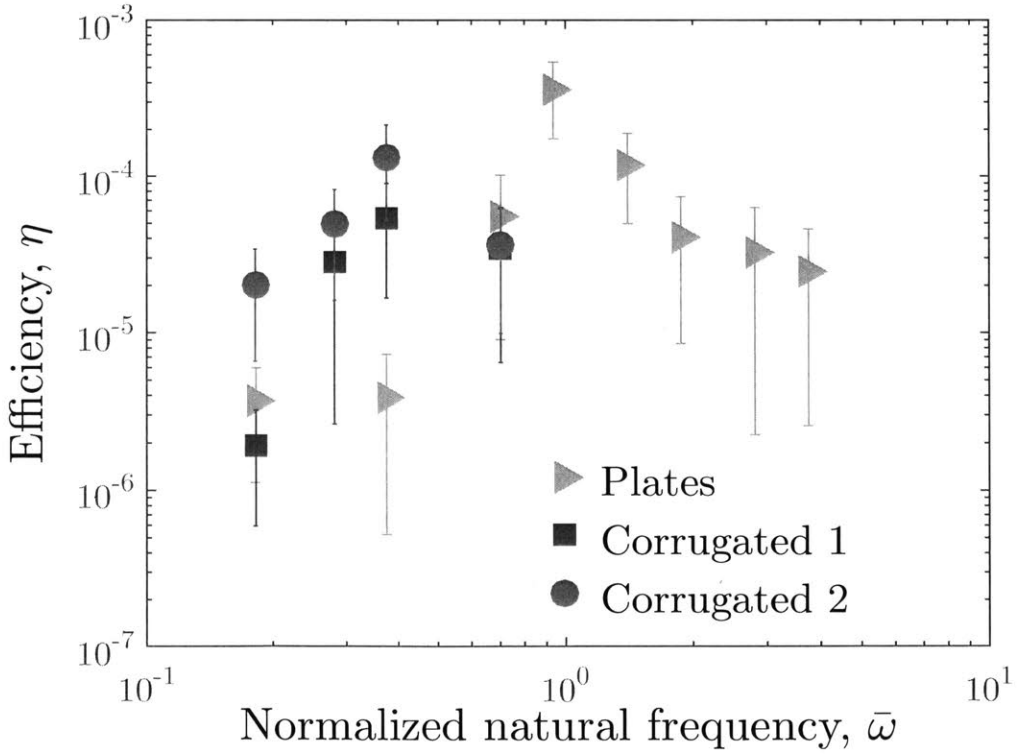

Figure 4-17: Power efficiency of corrugated design 1 (blue square) $\lambda = 133$ mm, $H = 12.5$ mm and $R = 200$ mm and corrugated design 2 (red circle) $\lambda = 200$ mm, $H = 12.5$ mm and $R = 200$ mm using plates of $h = \{51, 76, 102, 191\}\,\mu$m with original normalized natural frequency $\bar{\omega} = \{0.181, 0.271, 0.3613, 0.677\}$ compared to the flat planar plates (grey triangles).

rugated Fan 1, Corrugated Fan 2 and the corresponding semi-circular plates are $\eta = \{0.533, 1.331, 0.039\} \times 10^{-4}$. At $\bar{\omega} = 0.361$ and $\alpha = 32°$, the output power are $P_o = \{0.83, 4.67, 0.01\} \times 10^{-3}$ W for Corrugated Fan 1, Corrugated Fan 2 and the corresponding plate, respectively. We also consider how the input power changes with corrugation. At $\alpha = 48°$ and $\bar{\omega} = 0.361$, the input power $P_i = \{14.6, 13.61, 3.56\}$ W for Corrugated Fan 1, Corrugated Fan 2 and semi-circular plates. As we can see, the input power for the corrugated plates are $\approx 4 - 5$ times higher than the un-corrugated configuration. However, the improvement in output power far outweighs the increased required input power. Thus we observe the power efficiencies: η(Corrugated Fan 2) $>$ η(Corrugated Fan 1) $>$ η(plate).

Finally, we want to understand the effect of buckling on the power efficiency. We consider the case shown in Fig. 4-16 (normalized frequency $\bar{\omega} = 0.181$) where we observed that Corrugated Fan 2 buckled, while Corrugated Fan 1 did not. The input powers for Corrugated Fan 1, Corrugated Fan 2 and the plates at $\bar{\omega} = 0.181$ and $\alpha = 48°$ are $P_i = \{28.04, 19.55, 10.88\}$ W. It is interesting to note that the input power (and also torque) for Corrugated Fan 1 was $\approx 43\%$ higher than that of Corrugated Fan 2. On top of the larger fan tip deflection, which results in larger flow velocity ($\bar{u} = \{0.143, 0.246, 0.102\}$ at $\bar{\omega} = 0.181$ and $\alpha = 48°$ for Corrugated Fan 1, Corrugated Fan 2 and flat plate), this dynamic reversible buckling mechanism also alleviates the high torque that an undeformed corrugated plate would experience. The advantage of reverse buckling is hence two-fold: increasing velocity and the lowering input power requirement. However, not all corrugated designs are advantageous as we demonstrated above; corrugation without reversible buckling only increases the required input power without the benefit of increased flow. The resultant power efficiencies for Corrugated Fan 1, Corrugated Fan 2 and flat plate are $\eta = \{0.41, 3.00, 0.38\} \times 10^{-5}$ at $\bar{\omega} = 0.181$ and $\alpha = 32°$. The power efficiencies of all these plates are still significantly lower than a semi-circular plate near resonant frequency $\eta(\bar{\omega} = 0.98) = 5.19 \times 10^{-4}$.

4.6 Outlook of Corrugated Fan

From the experiments on the corrugated fans, we find that buckling of the corrugated fans allows them to achieve larger tip deflection and consequently higher values of velocity of the generated flow. We also observed that the shape of the corrugation has a significant impact on whether the fans will buckle under the flapping motion. Newman and Wootton [47] proposed that reversible buckling is a mechanism employed by dragonflies to withstand and alleviate the high load. Indeed, we observed from our experiments on the corrugated plates that the input torque for the corrugated plate that buckles reversibly is lower than the unbuckled case. To optimize corrugated plate design, it would be necessary to first study the mechanisms of dynamic buckling and develop a simplified model to determine if the plate will buckle. This is not a trivial problem as the loads are unsteady and also depends heavily on the flapping amplitudes and frequencies.

We note that dragonflies have wings with higher aspect ratio than a semi-circular shaped structure like the fans. Longer wings typically have to balance the larger bending moment at the wing root and the flexural stiffness of the wing. The corrugation designs provide the required rigidity without additional weight to the wings and were also proposed as an evolutionary optimization in insects such as dragonflies [47]. A study of using corrugation patterns on longer flapping structures could be conducted to further understand this trade-off. Coupled fluid-structure interaction simulations on the buckling deformation shape of the corrugated plates and the flow generation of the plates would have to be conducted in order to optimize the shape of the corrugated fans.

Chapter 5

Conclusion

In this concluding chapter, we first summarize (Section 5.1) the main findings of our experimental investigation on the aeroelastic behavior of four different flapping structures: planar homogeneous flat semi-circular plates, commercially available Spanish style pleated hand fans, discrete model fans and corrugated plates. Secondly, we discuss in Section 5.2 how our findings can be potentially applied to the understanding of the mechanisms of other flapping structures in nature, and the design of biomimetic flapping structures. Finally, in Section 5.3, we suggest some possible extensions of this thesis and direction for future research in the area of flapping structures.

5.1 Summary of Findings

In this thesis, we studied the aeroelastic behavior of four different flapping structures: planar homogeneous semi-circular plates (Section 5.1.1), commercially available Spanish style pleated handheld fans (Section 5.1.2), discrete model fans inspired by the hand fans (Section 5.1.3) and corrugated plates (Section 5.1.4). We used precision model experiments to understand the effects of structural designs on the ability of the fan to generate flow. The main findings for each of the categories are summarized below.

5.1.1 Homogeneous Semi-circular Plates

As a baseline for comparison with the other flapping structures, we quantified the normalized velocity $\bar{u}$ of the generated flow as a function of the normalized natural frequency $\bar{\omega}$ of the homogeneous semi-circular plates, for a range of thicknesses. We found that plates with $\bar{\omega} \sim 1$ produce the highest $\bar{u}$ and are also the most power efficient. Three thickness regime were defined: 1) *thin plates* for $\bar{\omega} \leq 0.6$; (2) *thick plates* for $\bar{\omega} \geq 2$; and (3) *intermediate plates* for $0.6 \leq \bar{\omega} \leq 2$. The behavior of these plates under flapping motion was understood by considering the contributing moments. Using the linearized Euler-Bernoulli equations, we expressed each of the moments in terms of geometrical and material parameters, and operating conditions. We found that for *thin plates*, the aerodynamic and the added mass moments dominate. In this case, the deflection is independent of the angular amplitude α and the efficiency scales as $\eta \sim \alpha$. For *thick plates*, the bending and the inertial moments dominate and, while deflection is also independent of angular amplitude, we have $\eta \sim \alpha^2$. For *intermediate plates*, it is more complicated than the previous two cases because all the ingredients (inertia, bending, aerodynamic and add mass) are of similar order of magnitude. In this third case, we find experimentally that $\bar{u} \sim \alpha^{-0.5}$ and $\eta \sim \alpha$.

5.1.2 Commercially Available Spanish Handheld Fans

We began by studying the mode shapes of the handheld fans at the first and second resonant frequencies and noted that the fans vibrated in a way similar to a series of beams arranged in a semi-circular array. We then found that the natural frequencies of the fans scale proportionally with the characteristic frequency of a beam. The three handheld fans (Fan 1, Fan 2 and Fan 3) were all found to have normalized natural frequencies that are in the thick plates regime. Fan 1, with a longer discrete section, was found to generate higher velocity flow than the rigid plates, while Fan 2 and Fan 3 generated comparable velocity with the rigid plates. All three fans were found to be more efficient than the rigid plates and we attributed this finding to their lower masses and flexural stiffnesses (which contributed to lower input power).

5.1.3 Discrete Model Fans

In order to explore the effect of discrete structures on the flow generation of the fans, we fabricated discrete model fans by attaching individual sectors shaped plates together. The natural frequencies of the discrete model fans were comparable to that of the homogeneous semi-circular plates with the same thickness. The discrete model fans produced 26-53% more flow than the corresponding semi-circular plates and also required slightly lower input torque to generate the flapping motion. Therefore, the discrete model fans have higher power efficiency compared to the semi-circular plates. We rationalized the increase in generated flow velocities by comparing the instantaneous deflection of the homogeneous plates, hand fans, and discrete model fans. We observed that the hand fan and the discrete model fans have significantly larger fan tip deflections compared to semi-circular plates of comparable natural frequencies. This is because the flat plates only deform through bending (resulting in uniformly zero Gaussian curvature) while the hand fans and discrete model fans experience in-plane expansions and compressions (resulting in regions of positive and negative Gaussian curvature).

5.1.4 Corrugated Plates

For the corrugated plates, we first compared the theoretical moment of inertia to FEM simulations and experimental results. Buckling behavior is observed for plates with high corrugation amplitude to thickness ratio ($H^2/h^2 \geq 1000$) and is not predicted by the theoretical models. This range of H^2/h^2 and is also the regime of interest for our study since we can only impose the corrugation shape on plates with thickness $h \leq 191\,\mu$m. We tested two different corrugation designs and observed improvements in flow generation and efficiency compared to the original un-corrugated plates. Between the two designs with the same corrugation amplitude, we observed the one which buckles during flapping has a larger fan tip deflection and consequently generated higher velocity flow. The buckled plate also required lower torque (and hence a lower input power) for the flapping motion.

5.2 Application to Biomimetic Flapping Structures

Beyond the specifics of handheld fans, we believe that uncovering the mechanisms for the enhancement of the flow generated by oscillating plate-like systems, which are both flexible and discrete, may open exciting opportunities in understanding the aeroelasticity of flapping structures such as insect and bird wings [71, 12, 45]. Moreover, these fundamentals could be invaluable in novel engineering designs of bio-inspired flapping drones [10, 39]. We hope that our findings will prompt zoologists, etymologists, and marine biologists to observe in detail the effect of modifying the stiff-ribs-compliant-connector structures in nature.

Our study identified the discrete nature of the ribs as a main structural design "ingredient" that allows the fan to achieve greater tip deflections. Hence, the fan is able to deform into a more favorable instantaneous shape, which in the case of our study, greatly improve the flow generation. We noticed that in self-propelling models, the frequencies at which optimal thrust production occurs is at a fraction of the natural frequencies [29, 53, 65]. We think that this discrete design could be paradigm shift in structural design which can be employed by biomimetic flapping wings structures with normalized natural frequencies $\bar{\omega} \geq 2$ to increase their thrust generation. We also identified plate corrugation as another structural design strategy to improve flow generation of plates with $\bar{\omega} \leq 0.6$. Our study confirmed that the corrugated plates employed the interesting mechanism of reversible buckling (proposed by Newman and Wootton [47] based on the observations on dragonflies) to generated higher velocity flow. In Chapter 3, we also scaled the moments and power efficiency with the flapping angular amplitude α. The findings have a direct implication on the controls and dynamics of flapping drones and robots.

5.3 Future Work

In this Section, we discuss some related works in literature and potential extensions for future research. Even if these are beyond the scope of the current study, we hope that our results will instigate future research activity in these directions.

5.3.1 Optimizing Discrete Section Models

Designs for flapping fans that contain discrete sections allows for finite Gaussian curvature to develop on the surface of the fan and improve the velocity of flow generation for $\bar{\omega} \geq 2$, with respect to flat homogeneous plate. A natural question to ask is whether the discrete design works for other $\bar{\omega}$ and if the optimal would occur at values other than $\bar{\omega} \approx 1$. In Sections 4.2.1 and 4.2.2, we also found that the shape of the discrete model fans is another important factor. Topology Optimization [62] could be applied to find the best sector shape for generating thrust. A further extension is to apply discrete sections to flapping structures that have are not semi-circular in shape, and in this case, the shape/size of the sectors in a plate may not uniform.

5.3.2 Visualization of Deformation and Optimization of Corrugated Plates

We noted that the amplitude and wavelength of the corrugations affect whether buckling occurs and has a significant effect on the generated flow. A natural potential research is to develop a simplified model to predict the conditions at which different corrugation shapes buckle dynamically. Since deflection shape is crucial for flow generation/thrust production, another direction for the study of the behavior of corrugated plate is related to the visualization of the resulting deflection. We can also apply corrugation to non-semi-circular structures. This is especially useful for structures with high aspect ratio since corrugation increases bending stiffness without additional weight.

5.3.3 Venation Network

The venation network of insect wings provides a structural support for the wing membrane to form the shape of the aerodynamic surface. Recent biological research has suggested that the overall flexural flexibility of insect wings scales to the cube of the span [12]. Moreover, the wings of *Manduca Sexta* have been shown to exhibit an exponential distribution of stiffness in the spanwise and chordwise direction [13]. A potential direction is to identify the geometrical and material design principles that contribute to this distribution of stiffness and develop a predictive understanding of the coupling between the structural properties of the wing due to the venation networks and the aerodynamic performance.

5.3.4 Porosity of the Flapping Structure

In nature, wing membranes can sometimes be porous but this has been typically overlooked in the literature. The handheld fans we tested have cloth leaves. The cloth material is a porous material in that there are spaces between the threads where air could move across. In this thesis and in existing designs of robotic flapping wings, we had used non-porous contiguous materials almost exclusively. Some robotic flapping wings had used cloth as a covering material [27, 33] but the trade-off is not well understood. The advantage of using a porous material is twofold: (i) it decreases the overall weight of the structures, and (ii) it allows the stiffness distribution across the wing to be readily tailored heterogeneously. The aerodynamics trade-off during flapping flight must then be understood so as to make use of porosity to optimize wing design. A possible direction for future work is to study the maximum degree of porosity that a wing membrane can contain, while still behaving aerodynamically as if it was contiguous.

Bibliography

[1] N. Agre, S. Childress, J. Zhang, and L. Ristroph. Linear drag law for high-reynolds-number flow past an oscillating body. *Physical Review Fluids*, 1(7):033202, 2016.

[2] S. Alben. Optimal flexibility of a flapping appendage in an inviscid fluid. *Journal of Fluid Mechanics*, 614:355–380, 2008.

[3] H. Alexander. *Fans.* London: BT Batsford, 1984.

[4] H. Aono, S. Chimakurthi, C. Cesnik, H. Liu, and W. Shyy. Computational modeling of spanwise flexibility effects on flapping wing aerodynamics. In *47th AIAA Aerospace Sciences Meeting including the new horizons forum and aerospace exposition*, page 1270, 2009.

[5] B. Audoly and Y. Pomeau. *Elasticity and Geometry: From Hair Curls to the Non-linear Response of Shells.* Oxford University Press, New York, New York, 2010.

[6] J. Bae, J. Lee, S. Kim, J. Ha, B-S. Lee, Y. Park, C. Choong, J-B. Kim, Z.L. Wang, H-Y. Kim, et al. Flutter-driven triboelectrification for harvesting wind energy. *Nature communications*, 5, 2014.

[7] A.P. Boresi and R.J. Schmidt. *Advanced mechanics of materials*, volume 6. Wiley New York, 1993.

[8] D. Briassoulis. Equivalent orthotropic properties of corrugated sheets. *Computers & Structures*, 23(2):129–138, 1986.

[9] J-S. Chen, J-Y. Chen, and Y-F. Chou. On the natural frequencies and mode shapes of dragonfly wings. *Journal of Sound and Vibration*, 313(3):643–654, 2008.

[10] Y. Chen, N. Gravish, A.L. Desbiens, R. Malka, and R.J. Wood. Experimental and computational studies of the aerodynamic performance of a flapping and passively rotating insect wing. *Journal of Fluid Mechanics*, 791:1–33, 2016.

[11] D. Claxton. Surface curvature, Matlab file exchange. https://www.mathworks.com/matlabcentral/fileexchange/11168-surface-curvature/content/surfature.m. Accessed: 2016-28-09.

[12] S.A. Combes and T.L. Daniel. Flexural stiffness in insect wings i. scaling and the influence of wing venation. *Journal of Experimental Biology*, 206(17):2979–2987, 2003.

[13] S.A. Combes and T.L. Daniel. Flexural stiffness in insect wings ii. spatial distribution and dynamic wing bending. *Journal of Experimental Biology*, 206(17):2989–2997, 2003.

[14] J.H. Comstock and J.G. Needham. The wings of insects. *The American Naturalist*, 33(395):845–860, 1899.

[15] T.R. Consi, P.A. Seifert, M.S. Triantafyllou, and E.R. Edelman. The dorsal fin engine of the seahorse (hippocampus sp.). *Journal of Morphology*, 248(1):80–97, 2001.

[16] J.F. De Celis and F.J. Diaz-Benjumea. Developmental basis for vein pattern variations in insect wings. *International Journal of Developmental Biology*, 47(7-8):653–663, 2003.

[17] P.A. Dewey, B.M. Boschitsch, K.W. Moored, H.A. Stone, and A.J. Smits. Scaling laws for the thrust production of flexible pitching panels. *Journal of Fluid Mechanics*, 732:29–46, 2013.

[18] M. Drela. *Flight Vehicle Aerodynamics.* The MIT Press, Cambridge, Massachusetts, 2014.

[19] C. Eloy, N. Kofman, and L. Schouveiler. The origin of hysteresis in the flag instability. *Journal of Fluid Mechanics*, 691:583–593, 2012.

[20] M. Gazzola, M. Argentina, and L. Mahadevan. Scaling macroscopic aquatic locomotion. *Nature Physics*, 10(10):758–761, 2014.

[21] M. Gazzola, M. Argentina, and L. Mahadevan. Gait and speed selection in slender inertial swimmers. *Proceedings of the National Academy of SciencesU.S.A.*, 112(13):3874–3879, 2015.

[22] S. Heathcote and I. Gursul. Flexible flapping airfoil propulsion at low reynolds numbers. *AIAA Journal*, 45(5):1066–1079, 2007.

[23] S. Heathcote, D. Martin, and I. Gursul. Flexible flapping airfoil propulsion at zero freestream velocity. *AIAA Journal*, 42(11):2196–2204, 2004.

[24] S. Heathcote, Z. Wang, and I. Gursul. Effect of spanwise flexibility on flapping wing propulsion. *Journal of Fluids and Structures*, 24(2):183–199, 2008.

[25] H. Hu, A. Gopa Kumar, G. Abate, and R. Albertani. An experimental study of flexible membrane wings in flapping flight. In *47th AIAA aerospace sciences meeting including the new horizons forum and aerospace exposition*, page 876, 2009.

[26] B. Hughey. Volumetric fluid flow measurement procedure, March 2017.

[27] P. Ifju, D. Jenkins, S. Ettinger, Y. Lian, W. Shyy, and M. Waszak. Flexible-wing-based micro air vehicles. In *40th AIAA Aerospace Sciences Meeting & Exhibit*, page 705, 2002.

[28] S.R. Jongerius and D. Lentink. Structural analysis of a dragonfly wing. *Experimental Mechanics*, 50(9):1323–1334, 2010.

[29] C-K Kang, H. Aono, C.E.S. Cesnik, and W. Shyy. Effects of flexibility on the aerodynamic performance of flapping wings. *Journal of Fluid Mechanics*, 689:32–74, 2011.

[30] E. Kausel and J.M. Roesset. Advanced structural dynamics. *Lecture Notes, Massachusetts Institute of Technology*, 2001.

[31] M. Keennon, K. Klingebiel, and H. Won. Development of the nano hummingbird: A tailless flapping wing micro air vehicle. In *50th AIAA Aerospace Sciences Meeting including the New Horizons Forum and Aerospace Exposition*, page 588, 2012.

[32] D. Kodali, C-K. Kang, and H. Aono. Analytical aerodynamic model of spanwise flexible flapping wings in forward flight. In *55th AIAA Aerospace Sciences Meeting*, page 0331, 2017.

[33] R.Y. Krashanitsa, D. Silin, S.V. Shkarayev, and G. Abate. Flight dynamics of a flapping-wing air vehicle. *International Journal of Micro Air Vehicles*, 1(1):35–49, 2009.

[34] G.V. Lauder and E.G. Drucker. Morphology and experimental hydrodynamics of fish fin control surfaces. *IEEE Journal of Oceanic Engineering*, 29(3):556–571, 2004.

[35] E. Lauga and T.R. Powers. The hydrodynamics of swimming microorganisms. *Report on Progress in Physics*, 72(9):096601, 2009.

[36] D. Lentink, S.R. Jongerius, and N.L. Bradshaw. The scalable design of flapping micro-air vehicles inspired by insect flight. In *Flying insects and robots*, pages 185–205. Springer, 2009.

[37] K.M. Liew, L.X. Peng, and S. Kitipornchai. Buckling analysis of corrugated plates using a mesh-free galerkin method based on the first-order shear deformation theory. *Computational Mechanics*, 38(1):61–75, 2006.

[38] Javier Llerandi. Casa de Diego, Madrid, Spain, Private communication, 2015.

[39] K.Y. Ma, P. Chirarattananon, S.B. Fuller, and R.J. Wood. Controlled flight of a biologically inspired, insect-scale robot. *Science*, 340(6132):603–607, 2013.

[40] J.H. Marden. Maximum lift production during takeoff in flying animals. *Journal of Experimental Biology*, 130(1):235–258, 1987.

[41] Holly Maxson. Design and construction of a support for a folding fan. 1986.

[42] S. Michelin and S.G.L. Smith. Resonance and propulsion performance of a heaving flexible wing. *Physics of Fluids*, 21(7):071902, 2009.

[43] S. Michelin, S.G.L. Smith, and B.J. Glover. Vortex shedding model of a flapping flag. *Journal of Fluid Mechanics*, 617:1–10, 2008.

[44] A.M. Mountcastle and S.A. Combes. Wing flexibility enhances load-lifting capacity in bumblebees. In *Proceedings of the Royal Society B*, volume 280, page 20130531. The Royal Society, 2013.

[45] A.M. Mountcastle and T.L. Daniel. Aerodynamic and functional consequences of wing compliance. *Experimental Fluids*, 46(5):873–882, 2009.

[46] D. Mueller, H.A. Bruck, and S.K. Gupta. Measurement of thrust and lift forces associated with drag of compliant flapping wing for micro air vehicles using a new test stand design. *Experimental Mechanics*, 50(6):725–735, 2010.

[47] DJS Newman and RJ Wootton. An approach to the mechanics of pleating in dragonfly wings. *Journal of Experimental Biology*, 125(1):361–372, 1986.

[48] A. Norman, S. Guest, and K. Seffen. Novel multistable corrugated structures. In *48th AIAA/ASME/ASCE/AHS/ASC Structures, Structural Dynamics, and Materials Conference*, page 2228, 2007.

[49] F. Paraz, L. Schouveiler, and C. Eloy. Thrust generation by a heaving flexible foil: Resonance, nonlinearities, and optimality. *Physics of Fluids*, 28(1):011903, 2016.

[50] P. Prempraneerach, F.S. Hover, and M.S. Triantafyllou. The effect of chordwise flexibility on the thrust and efficiency of a flapping foil. *Proceedings Unmanned, Untethered Submersible Technology*, 2003.

[51] G. Qian. *Chinese Fans: Artistry and Aesthetics*, volume 2. Long River Press, 2004.

[52] D.B. Quinn, G.V. Lauder, and A.J. Smits. Scaling the propulsive performance of heaving flexible panels. *Journal of Fluid Mechanics*, 738:250–267, 2014.

[53] S. Ramananarivo, R. Godoy-Diana, and B. Thiria. Rather than resonance, flapping wing flyers may play on aerodynamics to improve performance. *Proceedings of the National Academy of SciencesU.S.A.*, 108(15):5964–5969, 2011.

[54] G.W. Rhead. *History of the Fan.* Lippincott, Philadelphia, Pennsylvania, 1910.

[55] R.J. Ross et al. *Wood handbook: wood as an engineering material.* 2010.

[56] Sanjay P Sane. The aerodynamics of insect flight. *Journal of Experimental Biology*, 206(23):4191–4208, 2003.

[57] T. Schnipper, A. Andersen, and T. Bohr. Vortex wakes of a flapping foil. *Journal of Fluid Mechanics*, 633:411–423, 2009.

[58] T. Schnipper, L. Tophøj, A. Andersen, and T. Bohr. Japanese fan flow. *Physics of Fluids*, 22(9):091102, 2010.

[59] E. Seydel. The critical shear load of rectangular plates. 1933.

[60] M.J. Shelley and J. Zhang. Flapping and bending bodies interacting with fluid flows. *Annual Review of Fluid Mechanics*, 43:449–465, 2011.

[61] W. Shyy, H. Aono, S. K. Chimakurthi, P. Trizila, C-K Kang, C.E.S. Cesnik, and H. Liu. Recent progress in flapping wing aerodynamics and aeroelasticity. *Progress in Aerospace Sciences*, 46(7):284–327, 2010.

[62] O. Sigmund and K. Maute. Topology optimization approaches. *Structural and Multidisciplinary Optimization*, 48(6):1031–1055, 2013.

[63] G.K. Taylor, R.L. Nudds, and A.L.R. Thomas. Flying and swimming animals cruise at a strouhal number tuned for high power efficiency. *Nature*, 425(6959):707–711, 2003.

[64] H. Tennekes. *The simple science of flight: from insects to jumbo jets.* MIT press, 2009.

[65] B. Thiria and R. Godoy-Diana. How wing compliance drives the efficiency of self-propelled flapping flyers. *Physical Review E*, 82(1):015303, 2010.

[66] S. Timoshenko and S. Woinowsky-Krieger. *Theory of plates and shells.* 1959.

[67] G.S. Triantafyllou, M.S. Triantafyllou, and M.A. Grosenbaugh. Optimal thrust development in oscillating foils with application to fish propulsion. *Journal of Fluid and Structure*, 7(2):205–224, 1993.

[68] M.S. Triantafyllou, G.S. Triantafyllou, and D.K.P. Yue. Hydrodynamics of fish-like swimming. *Annual Review of Fluid Mechanics*, 32(1):33–53, 2000.

[69] Hugues Vandeparre, Miguel Piñeirua, Fabian Brau, Benoit Roman, José Bico, Cyprien Gay, Wenzhong Bao, Chun Ning Lau, Pedro M Reis, and Pascal Damman. Wrinkling hierarchy in constrained thin sheets from suspended graphene to curtains. *Physical Review Letters*, 106(22):224301, 2011.

[70] E. Ventsel. *Thin Plates and Shells: Theory, Analysis and Applications.* Marcel Dekker, Inc, University Park, Pennsylvania, 2001.

[71] Z.J. Wang. Dissecting insect flight. *Annual Review of Fluid Mechanics*, 37:183–210, 2005.

[72] Z.J. Wang, J.M. Birch, and M.H. Dickinson. Unsteady forces and flows in low reynolds number hovering flight: two-dimensional computations vs robotic wing experiments. *Journal of Experimental Biology*, 207(3):449–460, 2004.

[73] C.H.K. Williamson and R. Govardhan. Vortex-induced vibrations. *Annual Review of Fluid Mechanics*, 36:413–455, 2004.

[74] R.J. Wood. The first takeoff of a biologically inspired at-scale robotic insect. *IEEE transactions on robotics*, 24(2):341–347, 2008.

[75] Z. Ye. Enhance variational asymptotic method for unit cell homogenization (vamuch) for real engineering structures and materials. 2013.

[76] J. Zhang, N-S. Liu, and X-Y. Lu. Locomotion of a passively flapping flat plate. *Journal of Fluid Mechanics*, 659:43–68, 2010.